PHOTONIC CRYSTAL BASED SENSING USING BAND EDGE MODULATION

by

ATİLLA ÖZGÜR ÇAKMAK

Submitted to the Graduate School of Engineering and Natural Sciences
in partial fulfillment of
the requirements for the degree of
Master of Science

SABANCI UNIVERSITY
Spring 2005

PHOTONIC CRYSTAL BASED SENSING
USING BAND EDGE MODULATION

APPROVED BY:

Associate Prof. Dr. MERİÇ ÖZCAN **…….**
(Thesis Supervisor)

Assistant Prof. Dr. CEM ÖZTÜRK **…….**

Assistant Prof. Dr. İBRAHİM TEKİN **……..**

DATE OF APPROVAL: **.....……**

ABSTRACT

A photonic crystal (PC) based structure is proposed for sensing exceptionally small refractive index changes of a background medium. In a typical PC, we show that the band edges and the defect band(s) (if present) are very sensitive to the dielectric contrast. Hence, a propagating electromagnetic wave at a particular frequency gains significant phase shift due to the index changes. When the phase shift is measured interferometrically, it is possible to infer refractive index changes as small as ten to the power minus eleven per lattice distance.

We have concentrated on the band edge shifts of the two lowest bands of a square lattice of dielectric rods. Calculations reveal that a design of hundred times hundred rods could be utilized to sense an index modulation of ten to the power minus thirteen per square root Hertz with a modulation bandwidth of one Hertz, which is ten to the power five times better than the resolution of waveguide based sensors. Defect modes in PCs are even better candidates for sensing applications. A further resolution enhancement on the order of ten could be achieved.

We have performed proof of principle experiments in the microwave regime with a PC made of seven times seven alumina rods placed in a gas chamber, whose inner pressure is adjusted with a nitrogen tank. Obtaining the index modulations by changing the inner pressure, we witnessed that the experimental results are in very good agreement with the theory at the band edges.

ÖZET

Biz, bu proje ile tipik bir fotonik kristal yapısının frekans bandı ve eğer var ise kusur bant veya bantlarının küçük kırılganlık endeksi değişimlerine dahi çok hassas olduklarını gösteriyoruz. Bu amaç ile kurulacak bir yapının çok ufak mertebelerdeki kırılganlık endekslerinin değişimlerini ölçmekte kullanılabileceğini idda etmekteyiz. Öyle ki, fotonik kristal içerisinde seyahat etmekte olan bir elektromanyetik dalganın bu değişimlerden ötürü ciddi bir faz kaymasına uğrayacanı ve bu faz kaymasının girişimlendirme yolu ile ölçülmesi ile kafes başına on üzeri eksi onbir kadar küçük değişiklikleri fark edebileceğimizi savunuyoruz.

Projemiz boyunca asıl olarak kare kafesli, yalıtkan çubuklardan oluşan bir örgünün en alt iki frekans bandını inceledik. Hesaplarımız gösteriyor ki, yüze yüzlük bir kristal yapısı ile kırılma endeks frekansı bir Hertz ile değişen bir yapıda on üzeri eksi on üç bölü karekök Hertz lik bir hasasiyeti tutturmamız mümkün. Bu sonuçlarımız bile en iyi dalga kılavuzlarıyla yapılan tasarımlardan on üzeri beş kat daha üstün bir performans göstermekte. Dahası, kusur bantlarının bu hasasiyeti en az on kat olmak üzere daha da arttırdığını rapor ediyoruz.

Bu iddalarımızı kanıtlamak üzere yediye yedilik alumina çubuklar ile gerçekleştirdiğimiz fotonik kristal yapılarını mikro dalga rejiminde denedik. Optik kristalin de içine yerleştirilmiş olduğu gaz haznesinin basıncı bir nitrojen tüpü yardımı ile sabitlendi. Nitrojenin basıncı ile oynayarak istediğimiz kırılım endeks değişimlerini yarattık ve deneylere bu koşullarda devam ettik. En son olarak ise, deney sonuçları ile teorik hesaplara dayalı beklentilerimizin harkulade uyum içerisinde olduklarını gözlemledik.

To All Humanity

ACKNOWLEDGEMENTS

I would like to express my sincere thanks to my thesis supervisor, Dr. Meriç ÖZCAN for his accompany, patience and his help.

I would also like to thank Dr. Cem ÖZTÜRK and Dr. İbrahim TEKİN, as my thesis jury members, for their valuable feedbacks about my thesis.

My special thanks to our Microelectronics group, who has always let me feel as a part of the family. I am indebted to Ahmet Akın Ünal and Özgür Taşdizen for their friendly support whenever I needed, to Can Sümer for being my biggest MATLAB rival, and for his limitless oppositions, to Sinan Yalçın for surviving in Adana and sharing his countless adventures, to Mehmet Güney for setting up the exemplary graduate student figure in Sabanci University, to Bülent Köroğlu for his invaluable helps in our projects, to Ercihan İncetürkmen for his kindness and motivations, but most of all to my loving parents and to my concerned aunts, whom have shaped my future since my childhood.

TABLE OF CONTENTS

LIST OF FIGURES

LIST OF TABLES

CHAPTER 1

INTRODUCTION

1. 1 Motivation

Advances in the industry come along with the demand to engineer sensitive devices that could distinguish even the tiniest changes. Several sensor topologies have been developed and employed for specific cases. Sensor design has become an established separate branch in science, combining distinct parts from material, mechanical, biological, electrical and optical engineering.

Optical sensing mechanisms have recently attracted much attention due to their higher sensitivity and resolution. The principle of sensing procedures has been governed by the refractive index variations. In that account, numerous ways for optical detection have been proposed. Fiber optic sensors present low loss figures and immunity to surrounding electromagnetic fields unlike the commercially used transmission lines. Change in the optical properties of the fiber induces either phase or amplitude shifts (or both) on the traveling optical field which triggers the sensing mechanisms. Fibers can be coated with special, chemically sensitive layers to further increase the resolution [1-4]. Waveguide based sensors are also widely used in sensing applications. Optical couplers, resonators have been utilized for the best

performance. Shifts in optical free spectrum and coupling wavelengths have been correlated with refractive index changes. High resolution constants on the order of 10^{-5} have been obtained with such waveguide based configurations [5,6]. Yet, surface plasmon resonance is another method. By exciting the free charges at the metal dielectric interface, a field whose optical characteristics are dependent on the refractive index profile of the sample deposited over the metal, can be created. Thus, this dependency has been exploited to improve the sensing characteristics [7,8].

Nevertheless, as an alternative approach, Photonic Crystals have only been studied extensively since the beginning of 90s, after the first proposals of Yablonovitch [9] concerning the control of the electromagnetic wave propagations via periodic arrangements. The field is widely open to new ideas. Therefore, breakthrough innovations might be feasible with intelligent predictions. The high sensitivity of Photonic Crystal band edges and defect bands bears an appealing picture for sensor investigations. As a result, the possibility of sensing very small refractive index changes with Photonic Crystals has been our top priority and our possible contributions to the field have always been the ultimate motivation.

In recent years, Photonic Crystals have attracted considerable attention in sensor applications as well. There are chemical detectors and bio sensors reported in the literature based on Photonic Crystal configurations which work on the principle of measuring the changes in the dielectric contrast [10-12]. In such sensors, index modulation is detected by sensing the shift of the emission wavelength of Photonic Crystal lasers [13]. In our work here, we propose a method for the detection of a very small refractive index change by measuring the phase shift of a propagating electromagnetic wave. As we explain later, band diagrams are a strong function of the dielectric contrast and a slight change induces a large phase shift on the propagating wave. Dispersion relation of a Photonic Crystal is crucially significant in determining the stop bands, and it has been shown that non-linear optical properties of the Photonic Crystals can be employed to modify the band formations to be utilized for optical switching [14,15]. Here, we present that the deviations in the dielectric constants of the Photonic Crystal do also alter the band diagrams of the structure in a similar fashion. The sensitivity of the sensor can be understood in terms of the

dynamically revised dispersion relations and thereby the phase shifts of the traveling electromagnetic wave specifically at the band edges. In the following parts we are going to show that our method can reach down to refractive index sensitivities of $10^{-13}/\sqrt{Hz}$.

The scalability of Maxwell's equations helps us to examine the electromagnetic waves in a broader spectrum. The modes in the Photonic Crystal can be solved independent of the lattice constants. Then many of the essential experiments could be carried out at longer wavelengths. It has been proven that Photonic Crystal based beam splitters, channel drop filters function at microwave regimes without the loss of generality [16,17]. Regarding to this fact, we have realized our experimental set-up in the microwave regime. Our Photonic Crystal based sensor operates in the GHz frequencies and requires the construction of a square lattice crystal having a certain dielectric contrast with respect to the background index. Two antennas and an interferometer configuration are needed to analyze the scattered propagation of the electromagnetic waves. The modeling and the design of the sensor together with the experimental setup are investigated in the latter sections.

1.2 Photonic Crystal Literature Survey

Photonic Crystals (PCs) are periodic structures, which modify the dispersion relations of the electromagnetic (EM) fields. In analogy to that of electrons in a crystal, EM waves are prohibited from propagating in certain directions. For a particular frequency range, an EM wave can not be coupled into the PC and forbidden bands are formed. Many other interesting phenomena have also been suggested and observed. PCs yield lower radiation losses, and enables higher control of the light that makes them favorable in the field of integrated optics [18-21]. The transmission of light can be based on photonic band gap (PBG) effect rather than total internal reflection. Hence, absolute confinement of light at desired points can be achieved. This is the main reason of remarkable reduced cladding losses in optical fibers with PBG guidance. Intentionally created defects in the periodicity of the PCs have been designed as cavities for the enhancement of the radiation. Such defects perturb the

ideal photonic band gaps of the crystals, and can cause relatively sharp defect bands to enter into the gaps [22]. These types of cavities resemble their counterparts in optical literature and could be modified to create laser cavities with high quality factors [23]. Defects have also been demonstrated as promising candidates for tunable filters [24].

Novel ideas have been proposed to adjust the Photonic Crystals for optical communication systems. Stopping and coherently storing of light methodologies have been originated from the application of coupling mode theory in between the closely separated Photonic Crystal cavities [25]. Yet, a similar design has been shown to perform a complete time-reversal operation on any electromagnetic pulse [26].

Applications directly for microwave regimes have also been offered. Resonant cavity enhanced detectors and resonant antenna configurations with very high directivity have been embedded into Photonic Crystals [27,28]. PCs have been employed as antenna substrates to increase the power ratio of the radiated power into air to the substrate [29].

1.3 Organization of the Thesis

The thesis is going to proceed with a discussion of theories in Photonic Crystals, in chapter 2 where different kinds of PCs are going to be examined. Chapter 3 will be devoted to the computational methodologies of Photonic Crystals. Chapter 4 is going to be dedicated to the proposed design methodologies of Photonic Crystal sensors as well as the adaptation methods of Photonic Crystals for sensor applications. Experimental results will be presented in chapter 5 and finally conclusion and future work are going to be listed under chapter 6.

CHAPTER 2

THEORY OF PHOTONIC CRYSTALS

All successful accomplishments in science rely on concrete, consistent, flawless, applicable and presentable theoretical backgrounds. Math is a tool to describe and to simulate every problem in nature. Breakthrough innovations are governed by intelligent predictions based on theoretical calculations. Science is an accumulation of knowledge about the secrets of the working mechanisms of nature. A researcher should not be satisfied with any knowledge lacking logical and mathematical support. Otherwise paradoxes and misunderstanding are impossible to overcome. In parallel to that conjecture, this chapter aims to deal with both fundamental and advanced theoretical analysis of the Photonic Crystals. These analyses constitute the heart of the thesis and they are going to help justify the design strategies together with the overall approaching style towards Photonic Crystals. Introducing the fundamentals of Photonic Crystals has been the main objective.

2.1 Wave Equations and Eigenvalue Problem

As mentioned in the first chapter, finding a clever way of controlling the propagation of the electromagnetic waves has always been a priority. Photonic

Crystals have just been proposed and used for this specific purpose. Since we are going to be mainly concentrated on the interaction of the electromagnetic fields with the rigid structures like Photonic Crystals in this chapter, Maxwell's equations are the first and by far the most significant elements of our theory. It is possible to derive all the proceeding formulas, theories with these equations. The components of an electromagnetic wave (EM wave), which are the electric and magnetic fields, traveling through a media free of charges and currents had been proven to show the following relationships by Maxwell [30].

$$\begin{aligned}
&\vec{B}(r,t) = \mu_0 \mu(r) \vec{H}(r,t), \\
&\vec{D}(r,t) = \varepsilon_0 \varepsilon(r) \vec{E}(r,t), \\
&\vec{\nabla}.\vec{D}(r,t) = 0, \\
&\vec{\nabla}.\vec{B}(r,t) = 0, \\
&\vec{\nabla} \times \vec{E}(r,t) = -\frac{\partial}{\partial t} \vec{B}(r,t), \\
&\vec{\nabla} \times \vec{H}(r,t) = \frac{\partial}{\partial t} \vec{D}(r,t).
\end{aligned} \tag{2.1}$$

The standard notations for the electric field (E), the magnetic field (H), the electric displacement (D), and the magnetic induction (B) are used in these equations. Recalling the particular identity from Vector Arithmetic,

$$\vec{\nabla} \times \vec{\nabla} \times (\vec{A}) = \vec{\nabla}(\vec{\nabla}.\vec{A}) - \vec{\nabla}^2 \vec{A} \tag{2.2}$$

and adapting it for Maxwell's equations, the general, commonly cited wave notations can be reached for bulk materials where $\nabla.\varepsilon(r) = 0$ and $\mu(r) \approx 1$ everywhere.

$$\begin{aligned}
\vec{\nabla}^2 \vec{E} &= \mu_0 \varepsilon_0 \varepsilon \frac{\partial^2}{\partial t^2} \vec{E} \\
\vec{\nabla}^2 \vec{H} &= \mu_0 \varepsilon_0 \varepsilon \frac{\partial^2}{\partial t^2} \vec{H}
\end{aligned} \tag{2.3}$$

It is apparent that solutions to such second order differential equations will be in the form of $E = E_{amp} \exp(i(\vec{k}.\vec{r} - wt))$, $H = H_{amp} \exp(i(\vec{k}.\vec{r} - wt))$ where wave vector and frequency are designated with k and w respectively. Although bulk example may present an intuitive, rough idea, it can not be our primary interest since it does not offer any means to manipulate the fields. The waves will diffract with certain amplitudes and form an oscillatory pattern. However, the control of the propagating wave via transforming the power confinement as a function of the position vector requires the addition of several other layers with different dielectric constants. Then wave equations will turn out to be,

$$\begin{aligned} \frac{1}{\varepsilon(r)}\vec{\nabla}\times\{\vec{\nabla}\times\vec{E}(r,t)\} &= (\frac{w}{c})^2\vec{E}(r,t) \\ \vec{\nabla}\times\frac{1}{\varepsilon(r)}\{\vec{\nabla}\times\vec{H}(r,t)\} &= (\frac{w}{c})^2\vec{H}(r,t) \end{aligned} \tag{2.4}$$

Note that the material dispersion relation of $\varepsilon(r, w)$ is ignored and will be disregarded as long as a specific, rather narrow frequency spectrum is of our concern. Furthermore, harmonic waves similar to the solutions of EM waves in the bulk matter are sought. Speed of light is denoted as c, which is identical to $(1 / (\mu_0\varepsilon_0))^{1/2}$.

Eq. 2.4 is attributed as the *master equation* among the Photonic Crystal researchers. Although it does not seem to imply anything new from engineer's perspective, examination of the familiarities with the Schrödinger's energy eigenvalue theorem in quantum mechanics opens new standpoints. An object with a mass would obey the Schrödinger equation and its energy could be computed accordingly. A small comparison reveals the analogy in between.

	Quantum Theory	Electromagnetic Theory
Fields	$\psi(r,t) = \psi(r)\exp(iwt)$	$H(r,t) = H(r)\exp(iwt)$
Eigenvalue problem	$H\psi = E\psi$	$\zeta_H H = (w/c)^2 H$
Operators	$H = -\hbar^2\nabla^2/(2m) + V(r)$	$\zeta_H = \vec{\nabla}\times(1/\varepsilon(r))\vec{\nabla}\times$

Table 2.1 Analogy between Quantum Theory and Electromagnetic Theory

The Hamiltonian of the quantum theory (H) determines the eigenenergies (E) for an object whereas operator ζ_H clarifies the eigenfrequencies for the EM wave. Treating the electromagnetic wave equation in eq. 2.4 as an eigenvalue problem has been the driving point in Photonic Crystals literature. The eigenfields with separate eigenfrequencies span the field vector space. The eigenfields become orthogonal to each other and we may encounter degenerate fields. The operator ζ_H can be shown to be Hermitian. The consequences of regarding the electromagnetic wave problem as an eigenvalue question can be summarized in the subsequent section.

Orthogonal Fields	$\zeta_H H_1 = (\frac{w_1}{c})^2,\ \zeta_H H_2 = (\frac{w_2}{c})^2$ then if $w_1 \neq w_2$, $< H_1 \mid H_2 >= 0$
Hermitian Operator ζ_H	$< H_1 \mid \zeta_H H_2 >= \int dr H_1^* \frac{1}{\varepsilon(r)} \nabla \times \nabla \times H_2 = \int dr (\nabla \times \frac{1}{\varepsilon(r)} \nabla \times H_1)^* H_2$ $< H_1 \mid \zeta_H H_2 >=< \zeta_H H_1 \mid H_2 >$

Table 2.2 Implications of Linear Algebra over Electromagnetic Theory

2.2 Scaling Properties of the Maxwell Equations

Provided that we stay in the macroscopic region, there is no fundamental length scale for the solutions of the Maxwell's equations. Researchers have exploited this feature of the electromagnetic theory to carry out similar experiments in a broad frequency spectrum. A rough discussion has already been done in the first chapter but, mathematically when we scale our master equations by a factor of *s* we get,

$$
\begin{aligned}
& r' = sr, \vec{\nabla}' = \vec{\nabla} / s \\
& \frac{1}{\varepsilon(r)} \vec{\nabla} \times \{\vec{\nabla} \times \vec{E}(r,t)\} = (\frac{w}{c})^2 \vec{E}(r,t) \\
& \frac{1}{\varepsilon(r'/s)} s\vec{\nabla}' \times \{s\vec{\nabla}' \times \vec{E}(r'/s,t)\} = (\frac{w}{c})^2 \vec{E}(r'/s,t) \\
& \frac{1}{\varepsilon'(r')} \vec{\nabla}' \times \{\vec{\nabla}' \times \vec{E}'(r',t)\} = (\frac{w}{cs})^2 \vec{E}'(r',t)
\end{aligned}
\qquad (2.5)
$$

The solution of the problem at one length scale determines the solutions at all other length scales. This simple fact is of considerable practical importance. Since micro fabrication of complex micron-scale photonic crystals can be difficult, models can easily be tested in the microwave regime.

2.3 Time Reversibility

Time reversibility of the optical modes in the photonic crystals can be explained with the symmetrical manipulation of the supporting wave vectors. The complex conjugate of the master equation must also yield real eigenvalues, then we obtain

$$(\zeta_E E)^* = \zeta_E E^* = ((\frac{w(k)}{c})^2 E)^* = (\frac{w(-k)}{c})^2 E^* \tag{2.6}$$

It follows that the complex conjugate of the electrical mode produces same eigenfrequency. It sets the dependence of the eigenfrequencies on the wave vectors as $w(k) = w(-k)$. It can also be interpreted as the time reversibility of the electromagnetic waves given that we are working with the harmonic modes.

2.4 Symmetric Dielectric Media

Photonic Crystals are intelligently engineered structures composed of periodic unit cells. Yet, before going into the further details of the wave propagation and mode analysis in Photonic Crystals, an outline of these symmetric arrangements could be helpful. This section of the thesis will deal with the most frequently practiced periodic arrays in the world. We have also used similar configurations through out our designs.

Alternating dielectrics give the periodic appearance to the Photonic Crystals. Solid States is the best known theory for the appreciation of the physics behind these formations. The translational symmetries can be repeated over different dimensions. For a one dimensional case, that we can also call as Bragg gratings, may only have

one discrete translation operator. The dielectric configuration which is given in Fig. 2.1 can be qualified to obey the one dimensional characteristics.

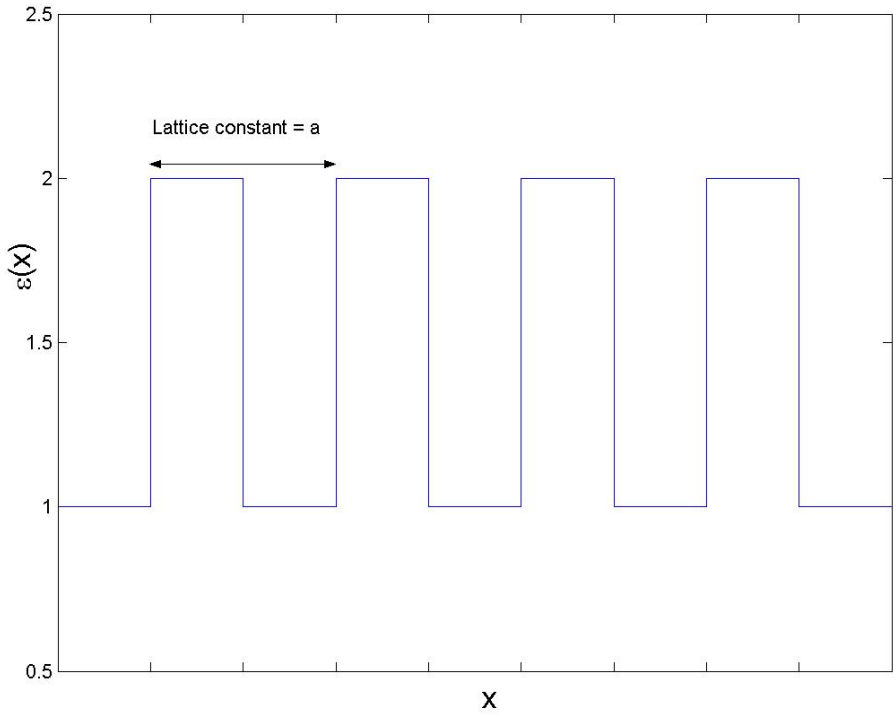

Fig. 2.1 Bragg Gratings (One Dimensional Symmetry)

Fig. 2.1 illustrates the scenario where ε_1=1 and ε_2=2 are the alternating dielectric medias. The simplest pattern that can recreate the crystal structure by repeating itself is called the unit cell and its length is abbreviated with the lattice constant, *a*. Then the dielectric function varies with x accordingly

$$\varepsilon(x) = \varepsilon(x + a) \tag{2.7}$$

If the pattern is extended into infinity then, it is trivial to assume that the electromagnetic fields will be in the form of

$$\begin{aligned} &E(\vec{x}, \vec{y}, \vec{z}, \vec{G}) \propto \exp(i(\vec{k}_{\vec{\rho}}.\vec{\rho}))\exp(i(\vec{k}_x + \vec{G}).\vec{x}) \\ &\vec{\rho} = \vec{y} + \vec{z} \end{aligned} \tag{2.8}$$

Here G is the reciprocal lattice vector and maintains the equality such that

$$\begin{aligned} &\exp(iG.x) = \exp(iG.(x+a)) \\ &\exp(iG.a) = 1 \\ &G.a = 2\pi n \end{aligned} \tag{2.9}$$

where n is an integer. The reciprocal lattice vector for Bragg gratings becomes $\vec{G} = \frac{2\pi}{a} n\vec{x}$.

The duplication of the unit cells may also continue in the second dimension whilst keeping the dielectric media homogenous in the third dimension. The square lattice and the triangular arrays are the generally studied models. Fig. 2.2 portrays a square lattice of rods on the x-y plane.

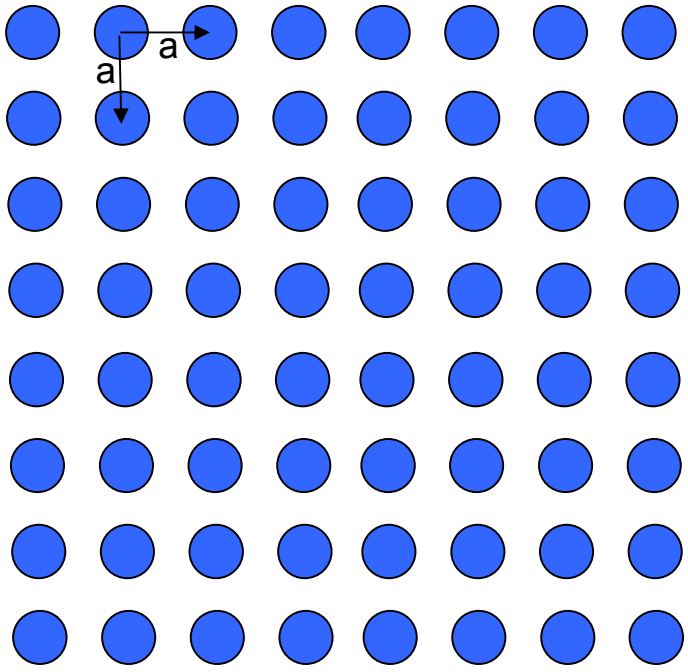

Fig. 2.2 Square Lattice of Rods

Any point on the plane can be expressed in terms of the x and y polar coordinates. However, we might not need to take care of all the points on the plane since the overall structure is a mere replication of the unit cell. If a particular k is

closer to a neighboring lattice point, you can always reach it by staying close to the original lattice vector and then translating by the G that reaches from one lattice point to the other as in eq. 2.8. The situation is depicted in Fig. 2.3.

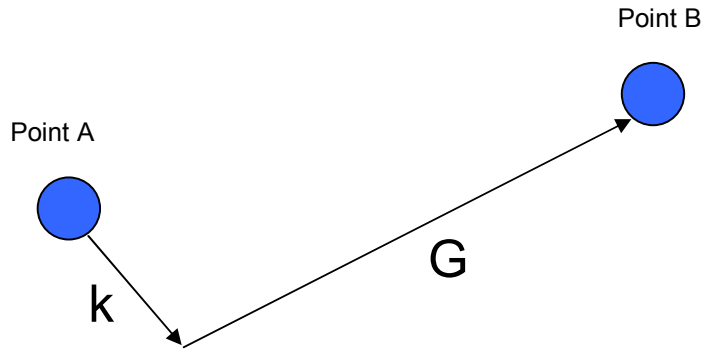

Fig. 2.3 Characterization of the First Brillouin Zone

Nevertheless we can specify the precise location of point B in wave vector space in terms of point A, thanks to the periodicity. Any electromagnetic field at point B will be just a reflection of the mode at point A. We need not take point B and all likes into consideration. An easy method of constructing a group of points that span the lattice space has to be presented. The technique of finding the Brillouin zone of the square lattice, whose points can not be written as a linear combination of others and reciprocal lattice vector is exhibited step by step in Fig. 2.4.

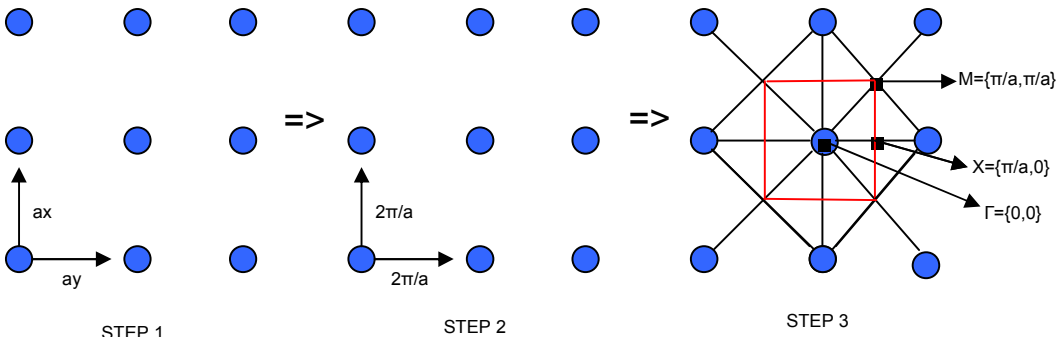

Fig. 2.4 Step by step construction of the First Brillouin Zone. Step1: Square Lattice array. Step 2: Reciprocal vector space for the Square Lattice array. Step 3: Midpoints of the intersecting lines give us a square boundary of the Brillouin zone.

It is uncovered that the first Brillouin Zone of the square rods is again a square with corners denoted with M. Point M is invariant under the translational operators C_{4v} [31]. Some of the C_{4v} group symmetry operators are

$$\begin{aligned}
&(x,y)\xrightarrow{E}(x,y)\\
&(x,y)\xrightarrow{\sigma_x}(-x,y)\\
&(x,y)\xrightarrow{\sigma_y}(x,-y)\\
&(x,y)\xrightarrow{\sigma_d}(y,x)\\
&(x,y)\xrightarrow{\sigma'_d}(-y,-x)
\end{aligned} \tag{2.10}$$

The points M, X and Γ have practical importance, because they found the Irreproducible Brillouin Zone. In any further calculations, it is going to be sufficient to only bear with them as the representatives of the overall lattice.

Likewise, similar treatments can be applied for the triangular lattice structures [32]. Triangular lattice has been demonstrated in Fig. 2.5. The general solutions for any reciprocal lattice vectors have been outlined as a set of equations for convenience in eq. 2.11 [33].

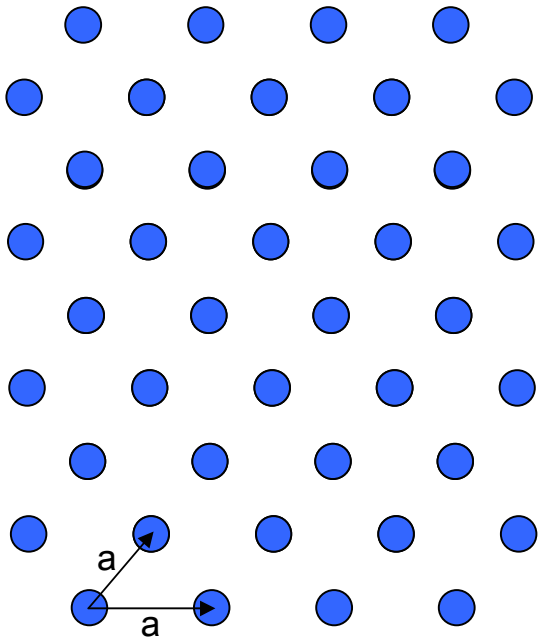

Fig. 2.5 Triangular Lattice of Rods

$$
\begin{aligned}
&\vec{R} = \vec{a}_{1x} + \vec{a}_{2y} + \vec{a}_{3y} \\
&\vec{G} = n_1\vec{x} + n_2\vec{y} + n_3\vec{z} \\
&\vec{G}.\vec{R} = 2\pi N \\
&n_1 = 2\pi \frac{\vec{a}_2 \times \vec{a}_3}{\vec{a}_1.\vec{a}_2 \times \vec{a}_3} \\
&n_2 = 2\pi \frac{\vec{a}_3 \times \vec{a}_1}{\vec{a}_1.\vec{a}_2 \times \vec{a}_3} \\
&n_3 = 2\pi \frac{\vec{a}_1 \times \vec{a}_2}{\vec{a}_1.\vec{a}_2 \times \vec{a}_3}
\end{aligned}
\tag{2.11}
$$

The translational symmetries oblige ζ_E, $(1/\varepsilon(r))\vec{\nabla}\times\vec{\nabla}$ to commute with all translation operators of the dielectric system. With this knowledge, we can identify the modes of ζ_E as simultaneous eigenfunctions of both translation operators. This argument is an entailment of quantum mechanics and has exceptional consequences that might be valuable in solving the Photonic Crystal bands. An ordinary translation operator, T_R, may translate a wave function by adding a certain phase to it.

$$
T_R\Psi = T_R \exp(ik.r) = \exp(ik.d).\exp(ik.r) = \exp(ik(r+d)) \tag{2.12}
$$

Symmetric dielectrics simplify many computationally hard problems. The biggest advantage of working with infinitesimally long periodic patterns is that they make the mathematical series expansions possible. All dielectric systems either periodic in one, two or three dimensions can be written as the Fourier expansion.

$$
\begin{aligned}
&\frac{1}{\varepsilon(r)} = \sum_G \varepsilon(G)\exp(iG.r) \\
&\varepsilon(G) = \frac{1}{V}\sum_V \frac{1}{\varepsilon(r)}\exp(-iG.r)
\end{aligned}
\tag{2.13}
$$

where V represents the volume of the unit cell. For example, the expansions of the dielectrics in Fig. 2.1 and 2.2 can be computed in a standard computer numerically. The expansions have been shown in Fig. 2.6 and 2.7 respectively.

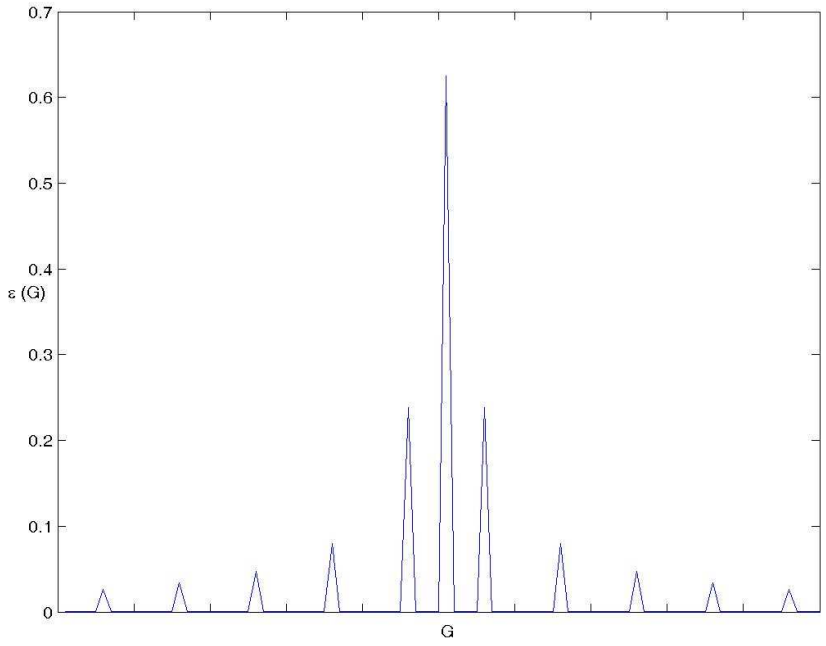

Fig. 2.6 Expansion coefficients of one dimensional structure (Fig. 2.1)

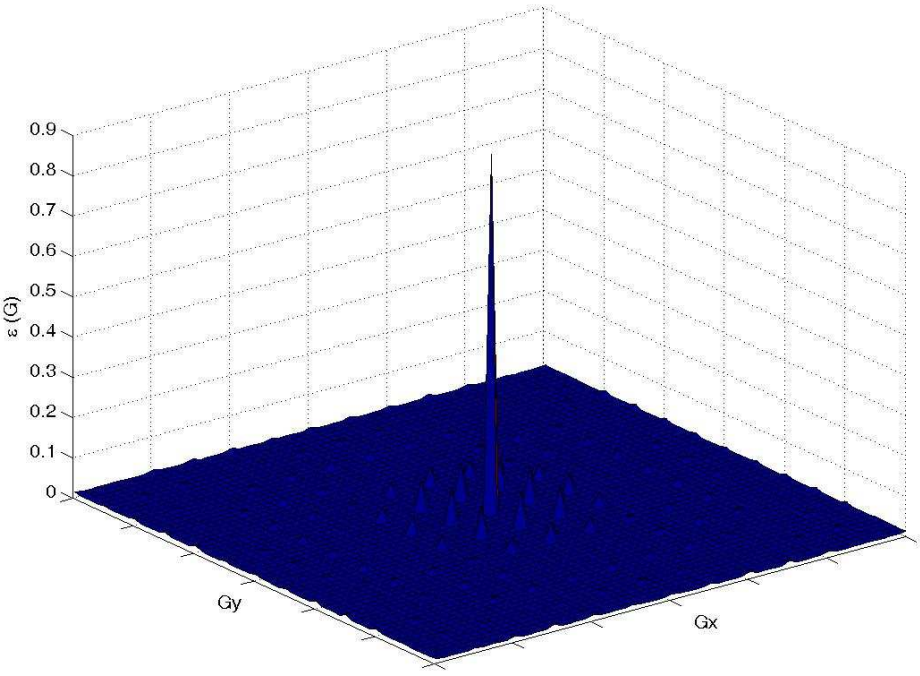

Fig. 2.7 Expansion coefficients of two dimensional structure (Fig. 2.2)

The DC components of the expansions outweigh the other harmonics as expected. After a tolerance value, the following harmonics' contributions become weaker. Since we are working with finite numerical elements in our hands, DFFT (Discrete Fast Fourier Transform) should be calculated up to a comparatively large number to sustain better approximations.

The last periodic formation that is of interest for us will be three dimensional lattices. Some very interesting and spectacular configurations have already been proposed by Photonic Crystal research groups. Thus, the most straight forward arrangement has been face centered cubic lattice (fcc).

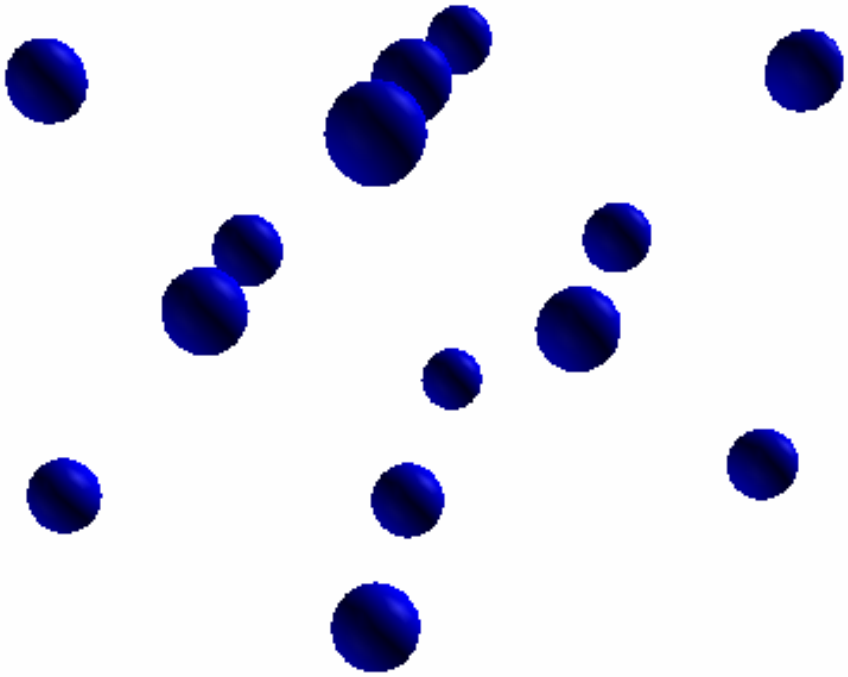

Fig. 2.8 FCC lattice

Three dimensional periodic structures can be theoretically analyzed, but the fabrication of a full 3D Photonic Crystal could be extremely difficult. Face centered cubic lattice structure is one the recurrently used configurations in solid state theory, but as we will discuss in further details, people tend to invent new devices in Photonic

Crystal literature that will somehow behave like a three dimensional periodic structure.

2.5 Symmetric Surprises, Theory of Photonic Crystals

This portion of the thesis will be devoted to the theory of the Photonic Band Gap materials. Beginning with the one dimensional case, all possible conventional configurations will be studied. The core of the theory has been developed since 90s. Several theories have been recently improved and the ultimate goal of the thesis has been to cover many of the new prospects of the field during the thesis preparation. In view of the fact that there is still no perfectly settled and accepted method for Photonic Band calculations, a considerable amount of ideas have been inspired by contemporary papers. Distinct computation routines have been adapted, but they will not be discussed in details in this subsection, but rather will be examined in the next chapter.

2.5.1 One Dimensional Photonic Crystals

One dimensional Photonic Crystals are excellent candidates to start learning the band formations and propagating mode analysis. They are relatively easier. An arrangement similar to Fig. 2.1 is used. As it will be done for others, first band diagrams will be analyzed. Later on localization at the defect sites and supported modes will be studied and finally off-axis propagation together with surface states will be investigated.

2.5.1.1 The Origin of the Bands

It has already been described in the first chapter that in analogy with electrons in semiconductors, bands appear for photons or in general for electromagnetic waves in photonic band materials. The dispersion relation exposes that some states with certain frequencies are not allowed to propagate in the photonic crystal regardless of

the wave vector, k. A resonant cavity, carved out of a photonic crystal, would have perfectly reflecting walls for frequencies in the gap. In the bulk material, using eq. 2.3 we see that frequency, w can be related to the wave vector, k .The dispersion relationship has been plotted in Fig. 2.9

$$w(k) = \frac{ck}{\sqrt{\varepsilon}} \tag{2.14}$$

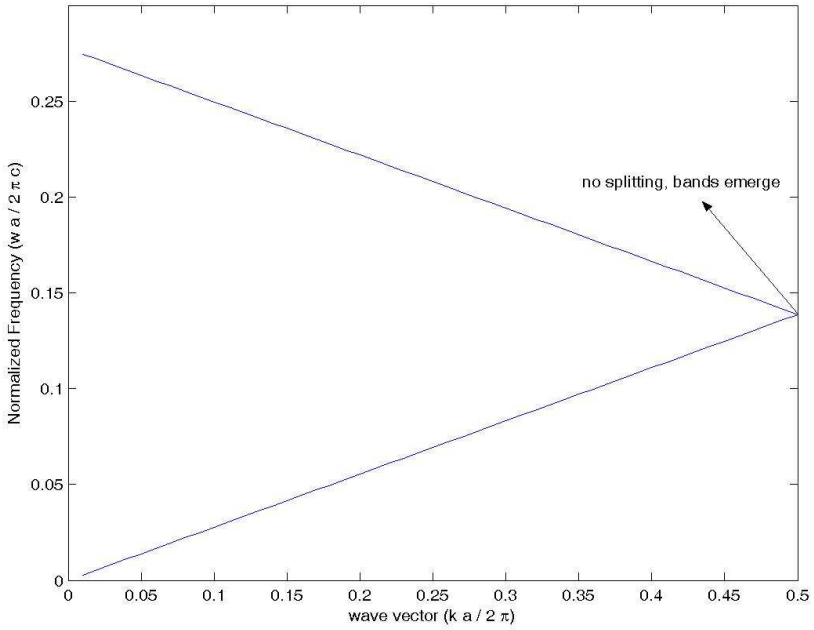

Fig. 2.9 First Two Bands for bulk material with $\varepsilon = 13$. The point k = 0, point k = 0 is omitted (computational difficulties).

On the other hand, when alternating multilayer dielectrics are studied, like in the case of Fig. 2.1, the electromagnetic wave propagating will be perturbed. There will be infinite amount of reflections at the boundaries and a gap will appear. Interesting enough, the structure will resemble an N slabs waveguide, where N goes to infinity if we extend the periodicity in one dimension. Then, we could explain the propagation of the electromagnetic waves in one dimensional Photonic Crystals in a similar fashion to the treatment of N slab waveguides in integrated optics.

2.5.1.1.1 Scattering through N Slabs

If we combine the theory of Quantum Tunneling [34] with Integrated Optics [35], and exploiting eq. 2.12, the dispersion relations can be fully understood. Visualizing the propagation of the wave in Fig. 2.10, the boundary conditions can be satisfied.

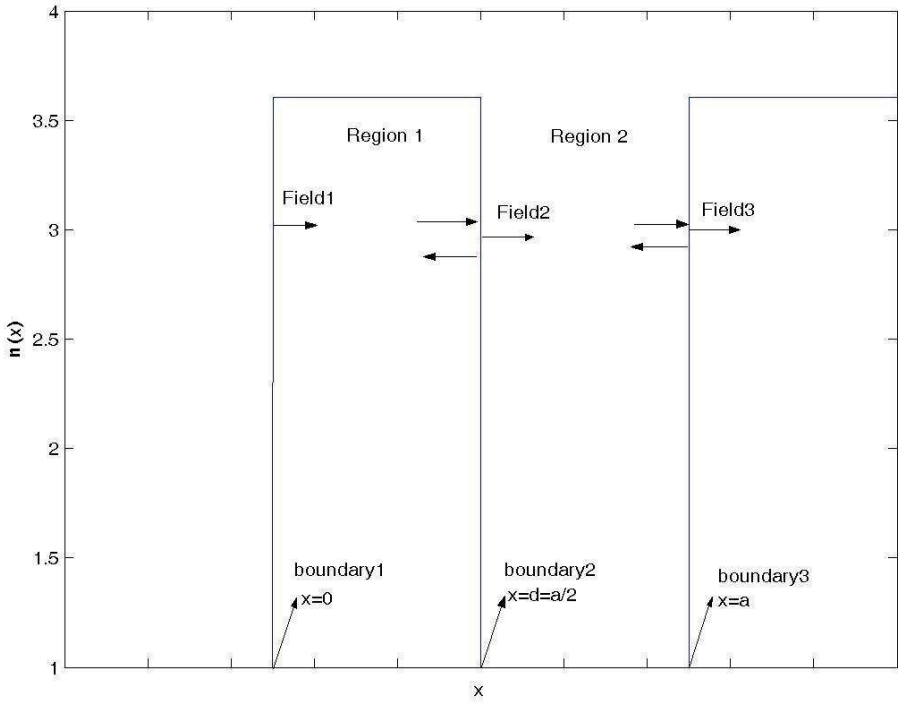

Fig. 2.10 Field Propagation in a 1-D (One dimensional) periodic structure, $\varepsilon_1 = 10, \varepsilon_2 = 1.$

As long as the pattern extends into infinity, the modes will be oscillatory in both high and low dielectric regions, unlike the case with finite number of N slabs in Integrated Optics. For the one dimensional case, eq. 2.4 can be interpreted in the proceeding form. Note that we will be working with TE modes, which also indicates that electric fields will play the major role, due to a random preference,. The duality in one dimensional Photonic Crystals compels the eigenstates to be degenerate. TM modes would support the same eigenfrequencies as TE modes.

$$\frac{c^2}{\varepsilon(x)}\frac{\partial^2 E_y(x,z,t)}{\partial x^2}=\frac{\partial^2 E_y(x,z,t)}{\partial t^2}$$

$$E_{1y}(x,z,t)=\left[Ae^{ik_1x}+Be^{-ik_1x}\right]e^{-iwt+ik_zz}\ldots region1$$

$$H_{1x}(x,z,t)=\frac{1}{iw\mu_0}\frac{\partial E_{1y}}{\partial z}$$

$$H_{1z}(x,z,t)=\frac{-1}{iw\mu_0}\frac{\partial E_{1y}}{\partial x} \qquad (2.15)$$

$$E_{2y}(x,z,t)=\left[Ce^{ik_2x}+De^{-ik_2x}\right]e^{-iwt+ik_zz}\ldots region2$$

$$H_{2x}(x,z,t)=\frac{1}{iw\mu_0}\frac{\partial E_{2y}}{\partial z}$$

$$H_{2z}(x,z,t)=\frac{-1}{iw\mu_0}\frac{\partial E_{2y}}{\partial x}$$

The boundary conditions at x = d = a/2 restricts the tangential components of the E and H fields to be continuous. But eq. 2.12 says that translational symmetry operators do not violate the commutation. Then we have another set of equations at x = a. The propagating wave's frequency component can be evaluated in terms of wave vector in separate regions. We can define a formula that manages the dispersion relations with different dielectric constants.

$$E_{1y}(x=0,z,t)=E_{2y}(x=a,z,t)e^{-ika}$$

$$k_1=\frac{w}{c}\sqrt{\varepsilon_1},k_2=\frac{w}{c}\sqrt{\varepsilon_2}$$

$$\begin{bmatrix}1 & 1 & -e^{ia(k_2-k)} & -e^{-ia(k_2+k)}\\ k_1 & -k_1 & -k_2e^{ia(k_2-k)} & k_2e^{-ia(k_2+k)}\\ e^{ik_1d} & e^{-ik_1d} & -e^{ik_2d} & -e^{-ik_2d}\\ k_1e^{ik_1d} & -k_1e^{-ik_1d} & -k_2e^{ik_2d} & k_2e^{-ik_2d}\end{bmatrix}\begin{bmatrix}A\\B\\C\\D\end{bmatrix}=\begin{bmatrix}0\\0\\0\\0\end{bmatrix}\Rightarrow M\begin{bmatrix}A\\B\\C\\D\end{bmatrix}=\begin{bmatrix}0\\0\\0\\0\end{bmatrix} \qquad (2.16)$$

$$\det(M)=0\Rightarrow\cos(k_1d)\cos(k_2(a-d))-\frac{{k_1}^2+{k_2}^2}{2k_1k_2}\sin(k_1d)\sin(k_2(a-d))=\cos(ka)$$

Now, we have every tool to compute the band structures. Consistently calculating the band structure for $\varepsilon_1=10,\varepsilon_2=1$ and d = a/2, we witness the birth of a frequency gap as in Fig. 2.11.

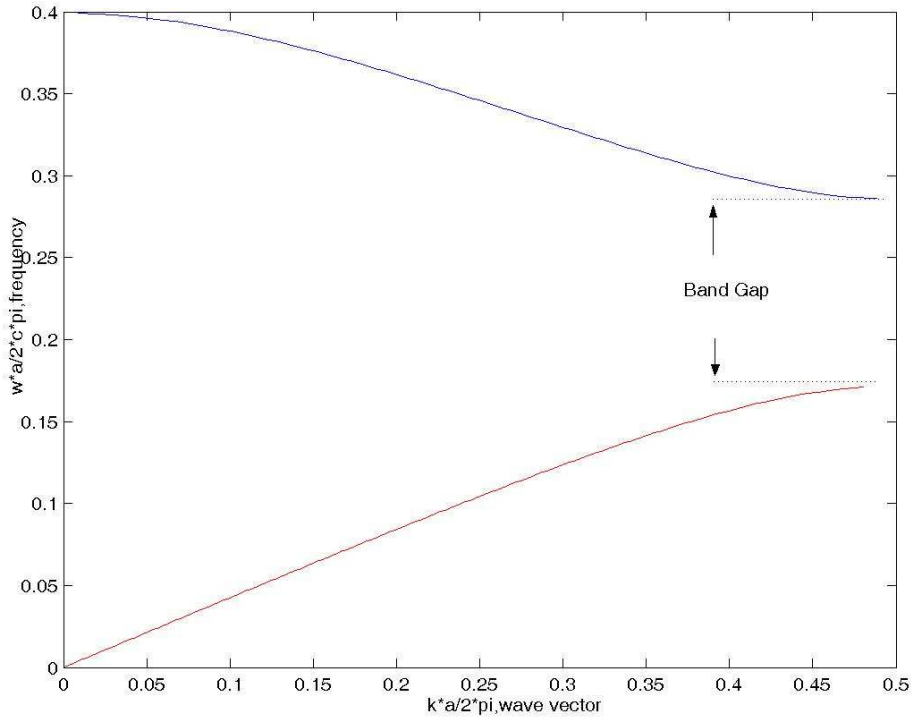

Fig. 2.11 Formation of the Band Gap Note that the band calculation does not converge at the band edges, k=0.5 has been omitted (computational difficulties).

It strikes our attention that the slope of the bands at the edges reaches almost zero. It means that an electromagnetic wave traveling with critical frequencies at the band edges will be stopped propagating at the x-direction (for our case), but still be diffracting at the other dimensions where no scattering has occurred. It should also be noted that the frequencies and wave vectors have been normalized, to make them independent of the lattice constant. Furthermore, only the bands in the Irreducible Brillouin Zone have been calculated.

2.5.1.1.2 Plane Wave expansion method

Plane wave expansion method is a frequently employed approach. It has been widely accepted. A lot of papers have been published discussing and weighing the advantages and the drawbacks of this technique since 90s. Plane wave expansion

method (PWEM) is adjustable for two and three dimensions as well. Now, a brief general formalism will be laid out at first and they will be specialized for the one dimensional case later on.

In the most universal situation, the PWEM relies on the expansion of the electromagnetic fields in a similar fashion to the dielectric tensors in eq. 2.13 because of the symmetry. Then mixing the Bloch's theory with the electromagnetism, the fields will look like

$$\begin{aligned} &\frac{1}{\varepsilon(r+R)} = \frac{1}{\varepsilon(r)} = \sum_G \kappa(G)\exp(iG.r) \\ &E_k(r,t) = u_k(r)e^{ik.r-iwt} = \sum_G E_k(G)\exp(i(k+G).r - iwt) \\ &H_k(r,t) = u_k(r)e^{ik.r-iwt} = \sum_G H_k(G)\exp(i(k+G).r - iwt) \end{aligned} \tag{2.17}$$

Combining the expansion coefficients for dielectric media and inserting into the *master equation* of eq. 2.4

$$\begin{aligned} &-\sum_{G'} \kappa_{(G-G')}(k+G')\times\{(k+G')\times E_{k,G'}\} = (\frac{w}{c})^2 E_{k,G} \\ &-\sum_{G'} \kappa_{(G-G')}(k+G)\times\{(k+G')\times H_{k,G'}\} = (\frac{w}{c})^2 H_{k,G} \end{aligned} \tag{2.18}$$

Each eigenfield is expressed in terms of the series expansion of the other contributors. Then, the coupled matrix is constructed. Eq. 2.18 is an ordinary eigenvalue equation and a regular computer can be programmed to numerically solve the matrix formulas. Computation methodologies and convergence problems of this technique belong to another chapter.

Even though the equations illustrate the spherical wave expansions to prevent the loss of generality, plane waves have been utilized in computations, which possess the property of eq. 2.19. The phase fronts of such fields are constant and form a plane at a specific point.

$$\vec{E}(r,t) = \vec{E}_0 \exp(i\vec{k}.\vec{r})$$
$$\vec{k}.\vec{E}_0 = 0 \tag{2.19}$$

Modifications for the one dimensional structure are needed. Eq. 2.17 and 2.18 can be transformed into the following statements, and when Maxwell's equations have been altered for one dimensional problem, band gaps occur for the exactly same configuration whose dispersion relations are demonstrated in Fig. 2.11.

$$\frac{1}{\varepsilon(x)} = \sum_{m=-\infty}^{\infty} \kappa_m \exp(i\frac{2\pi m}{a}x)$$
$$E_k(x,t) = u_k(x)e^{ik.x-iwt} = \sum_{m=-\infty}^{\infty} E_m \exp(i(k+\frac{2\pi m}{a})x - iwt)$$
$$H_k(x,t) = u_k(x)e^{ik.r-iwt} = \sum_{m=-\infty}^{\infty} H_m \exp(i(k+\frac{2\pi m}{a})x - iwt) \tag{2.20}$$
$$-\sum_{m'=-\infty}^{\infty} E_{m'}(k+\frac{2\pi m'}{a})^2 \kappa_{(m-m')} = (\frac{w}{c})^2 E_m$$
$$-\sum_{m'=-\infty}^{\infty} H_{m'}(k+\frac{2\pi m}{a})(k+\frac{2\pi m'}{a})\kappa_{(m-m')} = (\frac{w}{c})^2 H_m$$

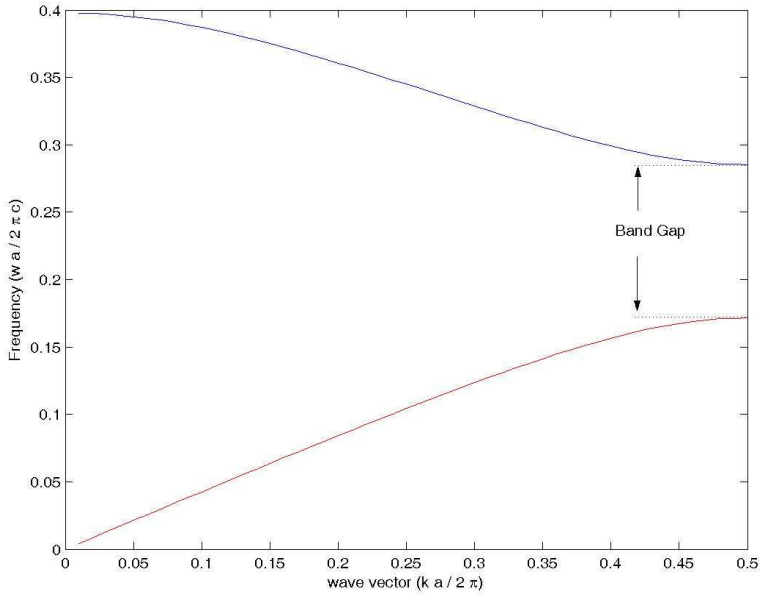

Fig. 2.12 PWEM version of the dispersion graph in Fig. 2.11

Comparison of the two graphs states the fact that for the one dimensional case, PWEM can be successfully performed. There is still a tiny amount of error involved in the expansion method, since we are limited with finite quantities of harmonics, rather than the ideal model in eq. 20. For infinitesimally long periodic structures we could predict that scattering method would yield the exact results whereas in PWEM our results would be limited by the number of plane waves taken into consideration.

2.5.1.2 Localization at the Defect Site and Field Profiles

Cavities with high quality factors can be engineered and tuned easily with Photonic Crystals. This neat feature signifies their practical importance. A defect is any kind of perturbation in the symmetric crystal. A breakdown in the pattern can be utilized to localize the fields that used to be in the band gap. Their presence would actually be prohibited in a perfect crystal, but defects lift up these bands into the forbidden region. Moreover these modes would not be supported by the Photonic Crystal itself, so they will have nowhere to escape other than being confined at the defect site. Defect modes are bound to die in the crystalline structure and they are also referred as evanescent fields in the Photonic Crystal. This incident bears strong resemblance to the quantum-mechanical problem of a particle in a box. Even in a one dimensional array, it is possible to have very sharp, high quality and low bandwidth cavity configurations. Density of states of the photonic crystal has been clearly disturbed by the existence of the defect. Fig. 2.13 demonstrates the phenomena for a periodic arrangement similar to the one in Fig. 2.10. The defect is produced by removing one of the gratings with dielectric constant of10. The edges of the lower and upper bands do not change (check from Fig. 2.11 or 2.12), the only major modification is the insertion of the defect band into the photonic band gap.

The removed grating confines the electric fields at the defect site. In Fig. 2.14 the electric field variation versus dielectric constant is plotted. A quick calculation displays that %46 of the overall power of the field has been confined at the defect site. The displacement fields with defects are also computed in the same manner. For our case N slab scattering method has been employed.

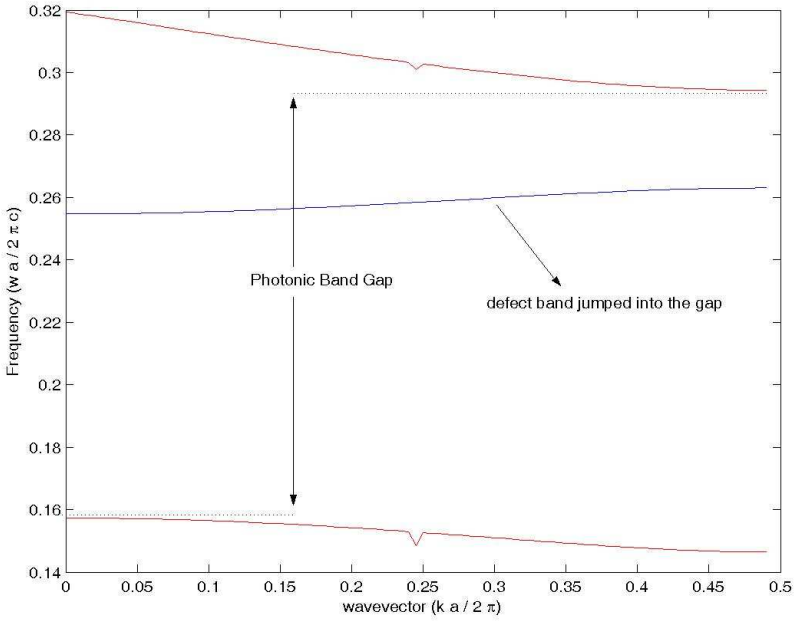

Fig. 2.13 Defect Band in the Photonic Band Gap. Note that discontinuous points at the lower and upper bands are computational errors. The defect band is calculated with the N slab scattering method.

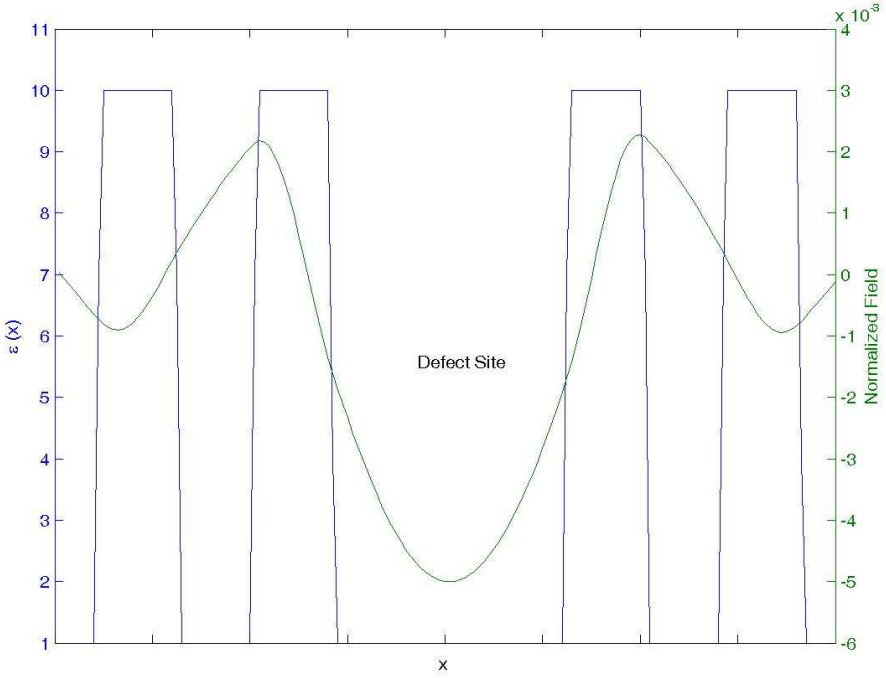

Fig. 2.14 Field Localization at the Defect Site.

2.5.1.3 Off-Axis Propagation and Surface States

So far we have considered the modes propagating perpendicular to the gratings. This is not always the case, for a multilayer film, because the off-axis direction contains no periodic dielectric regions to coherently scatter the light, the bands will not split up to open a gap. The bands will occur only if the propagation wave vector and the $\vec{\nabla}(\varepsilon(r))$ dielectric function vectors coincide in the same direction. This generalization applies for the two dimensional Photonic Crystals as well. Three dimensional Photonic Crystals have complete periodic patterns in all directions, so electromagnetic wave can be coupled inside from every track and the traveling waves may open forbidden regions without any complications.

Furthermore, the majority of our discussion has concerned the interior of photonic crystals of infinite extent. But real crystals are necessarily bounded. At the boundary surface of the crystal structure, extended or decaying fields can be observed. Any defect at the air boundary can localize fields in between Photonic Crystals and background air region. They may behave like surface plasmon-polaritons in metallic surfaces. They are very sensitive to the termination of the structure [36].

These features might obscure the analysis of the Photonic Crystals. Ignoring these effects, we will be sticking to the essential assumption of infinite crystals while conveying the design methodologies. The difficulties of projecting these assumptions into the real life experiments will be described in another chapter. It would not be beneficial to totally ignore these influences mainly coming from the finite dimensions of the periodic arrangements, but a clever way to reduce their nonlinear contributions has to be sought.

2.5.2 Two Dimensional Photonic Crystals

After having examined the interesting properties of one-dimensional photonic crystals, the thesis will continue to investigate situations where the crystal is periodic in two dimensions and homogenous in the third. Initially, the gap formation

mechanisms will be discussed in order to progress with the defect studies. The mode profiles will be considered and the section will be concluded by briefly referring to the out of plane propagation and surface states again.

Two dimensional structures are of great significance for the thesis preparation. Many of the design criteria have been based on the solid theoretical analysis of the two dimensional Photonic Crystals.

2.5.2.1 Gaps in two dimensions

It is not hard to predict that gaps will also appear in two dimensional structures, like their counterparts in the one dimension. Two dimensional structures enable us to confine the electromagnetic wave in a plane. Therefore, polarized plane waves will be the major actors of the contemplation. First of all, prudently the polarization vectors inside the crystals must be clarified. There is a small difference in Photonic Crystal literature in terms of defining the TE and TM polarizations in comparison with the other photonic contexts [35]. TE and TM polarizations are defined in the following manner.

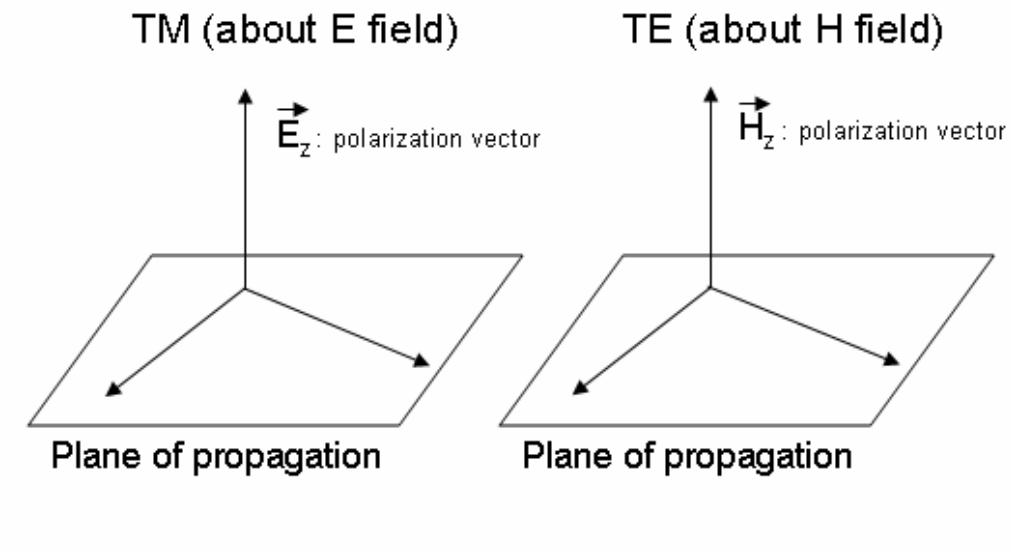

Fig. 2.15 Polarization definitions

Then the fields will be staying totally in the plane of periodicity and scattering from crystals will be the source of forbidden gaps. Our fields could be summarized as

$$\begin{aligned}\vec{E}(x,y,t) &= \vec{E}_z \exp(i(\vec{k}_x.\vec{x} + \vec{k}_y.\vec{y}))\exp(-iwt)\ldots TM \\ \vec{H}(x,y,t) &= \vec{H}_z \exp(i(\vec{k}_x.\vec{x} + \vec{k}_y.\vec{y}))\exp(-iwt)\ldots TE\end{aligned} \tag{2.21}$$

Crystalline structures similar to Fig. 2.2 and 2.5 will be taken into account. Uniquely, we can now distinguish the propagation of the distinct polarized electromagnetic waves in different media. Without going any further, an adjustment to the generalized plane wave expansion method given in eq. 2.17 and 2.18 has to be done to be able to solve band diagrams in two dimensions. Then polarization dependency on the band splitting can be scrutinized.

2.5.2.1.1 Plane Wave Expansion for 2-D structures

If we take the square lattice as an example, then points Γ, X and M (Fig. 2.4) will become the corners of the Irreducible Brillouin zone. And the reciprocal lattice vector is simply

$$G = \frac{2\pi x}{a} n_1 + \frac{2\pi y}{a} n_2 \tag{2.22}$$

where n_1 and n_2 are any integers. Our *master equation* in eq. 2.4 is going to look like

$$\begin{aligned}\zeta_E E_z(x,y) &= -\frac{1}{\varepsilon(x,y)}\{\frac{\partial^2}{\partial x^2} + \frac{\partial^2}{\partial y^2}\}E_z(x,y) = (\frac{w}{c})^2 E_z(x,y) \\ \zeta_H H_z(x,y) &= -\{\frac{\partial}{\partial x}\frac{1}{\varepsilon(x,y)}\frac{\partial}{\partial x} + \frac{\partial}{\partial y}\frac{1}{\varepsilon(x,y)}\frac{\partial}{\partial y}\}H_z(x,y) = (\frac{w}{c})^2 H_z(x,y)\end{aligned} \tag{2.23}$$

Symmetry expansion rules still apply for the fields and dielectric tensors,

$$E_{k,z}(x,y,t) = \sum_{n_2=-\infty}^{\infty}\sum_{n_1=\infty}^{\infty} A_{n1,n2}\exp(i((k_x+\frac{2\pi}{a}n_1)x+(k_y+\frac{2\pi}{a}n_2)y)-iwt)$$
$$H_{k,z}(x,y,t) = \sum_{n_2=-\infty}^{\infty}\sum_{n_1=\infty}^{\infty} B_{n1,n2}\exp(i((k_x+\frac{2\pi}{a}n_1)x+(k_y+\frac{2\pi}{a}n_2)y)-iwt) \quad (2.24)$$

Reminding that these formulas are only valid for the in-plane propagation where k_z=0. Then the two dimensional matrix can be constructed upon calculating the each harmonic contributor of the eigenvalue equation,

$$\sum_{n'_2=-\infty}^{\infty}\sum_{n'_1=-\infty}^{\infty} A_{n1,n2}((k_x+\frac{2\pi}{a}n'_1)^2+(k_y+\frac{2\pi}{a}n'_2)^2))\kappa_{(n_1-n'_1),(n_2-n'_2)} = (\frac{w}{c})^2 A_{n1,n2}$$
$$\sum_{n'_2=-\infty}^{\infty}\sum_{n'_1=-\infty}^{\infty} B_{n1,n2}((k_x+\frac{2\pi}{a}n'_1).(k_x+\frac{2\pi}{a}n_1)+(k_y+\frac{2\pi}{a}n'_2).(k_y+\frac{2\pi}{a}n_2)))\kappa_{(n_1-n'_1),(n_2-n'_2)} \quad (2.25)$$
$$= (\frac{w}{c})^2 B_{n1,n2}$$

Then band formations can be calculated with this technique as shown in Fig. 2.16.

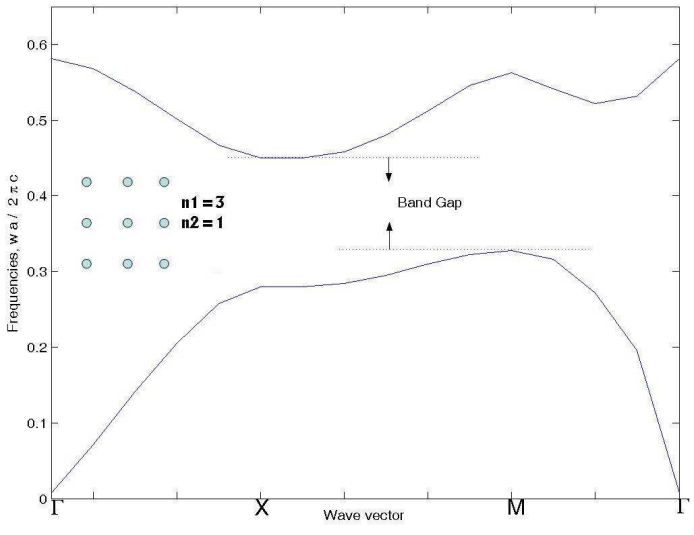

Fig. 2.16 Band Diagram in Two Dimensions

2.5.2.1.2 Variation Principle (MIT's method)

Plane wave expansion method has widely been accepted and used in Photonic Crystals literature [37-42]. Yet, people might have different perspectives and methodologies. The Photonic Crystal research group at Massachusetts Institute of Technology (MIT) has developed their Photonic Crystal solver software [43]. This software computes the eigenfrequencies based on plane wave expansion method, but rather than carrying out the calculations with an iterative eigensolver, it makes use of the variation principle from perturbation theory of quantum mechanics. Variation method can be reviewed in a couple of words. An intuitive way to find the normalized frequency can be

$$w_n = \frac{< H \mid \zeta_H \mid H >}{< H \mid H >} \tag{2.26}$$

From this standpoint, when we add δH to our current state, w_n should not change, if we are at a saddle point. Moreover, w_n is going to be the lowest possible frequency value for the ground state.

If we write a state H from the beginning as a linear combination of suitable basis, and calculate the eigenfrequency, then it should satisfy $\partial w_n / \partial H = 0$. Hence, as soon as the ground state is estimated, then simultaneous orthogonal eigenvalues that span the field space are directly the eigenfields due to the Hermitian ζ_H operator.

$$\begin{aligned}
&H^k{}_w(r) = \sum_{G\lambda} h_{G\lambda}\vec{e}_\lambda \exp(i(k+G)r) \\
&\sum_{(G\lambda)'}\left[(k+G)\times\vec{e}_\lambda\right]\left[(k+G')\times\vec{e}_{\lambda'}\right]\varepsilon^{-1}(G,G')h_{(G\lambda)'} = (\frac{w}{c})^2 h_{(G\lambda)} \\
&w_{\text{var}} = \frac{\sum_{(G\lambda)'}\sum_{(G\lambda)} h_{G\lambda}{}^*\left[(k+G)\times\vec{e}_\lambda\right]\left[(k+G')\times\vec{e}_{\lambda'}\right]\varepsilon^{-1}(G,G')h_{(G\lambda)'}}{\sum_{G\lambda} h_{G\lambda}{}^* h_{(G\lambda)'}} \\
&w_{\text{var}} = \frac{< H^k{}_w \mid \zeta_H \mid H^k{}_w >}{< H^k{}_w \mid H^k{}_w >}
\end{aligned} \tag{2.27}$$

After having expanded the field vectors and attaining the eigenvalue equation, variation method is exercised [32]. The computations reveal a similar band diagram that has already been portrayed in Fig. 2.16.

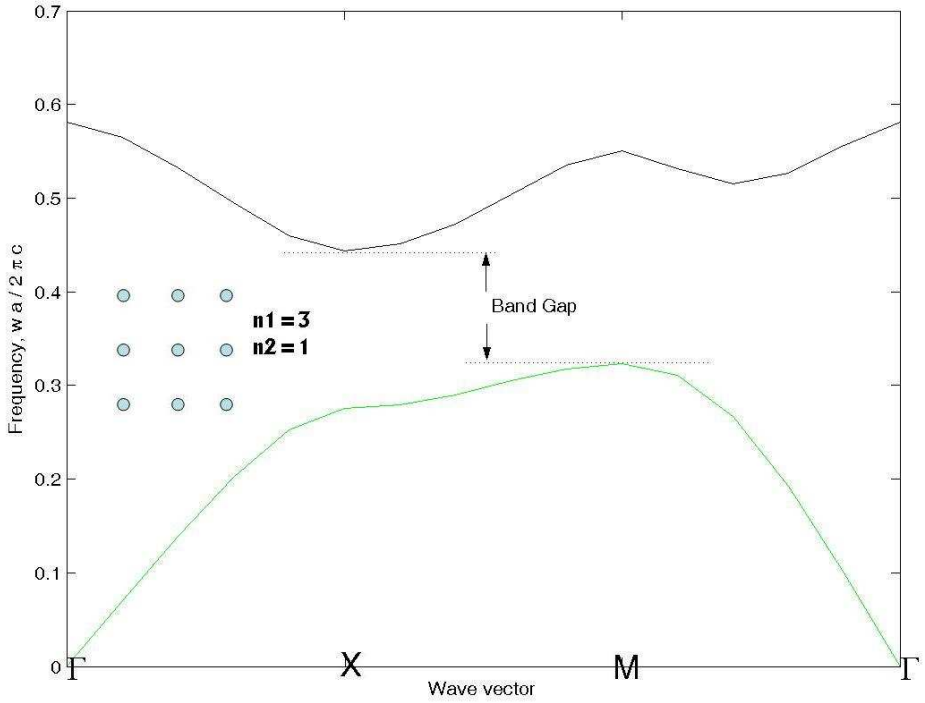

Fig. 2.17 Two Dimensional Band Diagram from variation method [44]

2.5.2.1.3 Polarization Dependency

The shape of the band diagrams are strongly related with the periodic configuration of our crystal. As we have seen, a square lattice of dielectric rods would behave as a photonic band gap material when TM polarized electromagnetic wave is coupled into them. Therefore, we have to search for the eigenvalues coming from the expansion of the electric fields instead of magnetic fields. However, if we still desired to view the band structures for TE polarizations, we would get a continuum of frequencies as dictated in Fig. 2.18. Yet, for another periodic configuration, such as for a square lattice of veins, TM polarizations would not split a gap whereas TE would. Shortly, it can be generalized that TM band gaps are favored in a lattice of

isolated high dielectric regions, and TE band gaps are favored in a connected lattice. Research groups have also proposed arrangements where both of the polarizations would yield a gap for propagating electromagnetic fields [32].

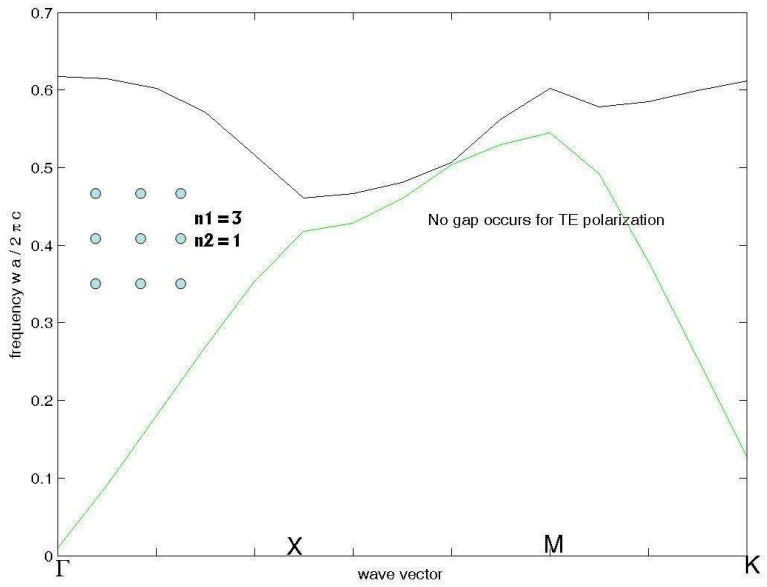

Fig. 2.18 Bands for TE polarization. Note that K is point {0.1, 0.1} in irreducible zone

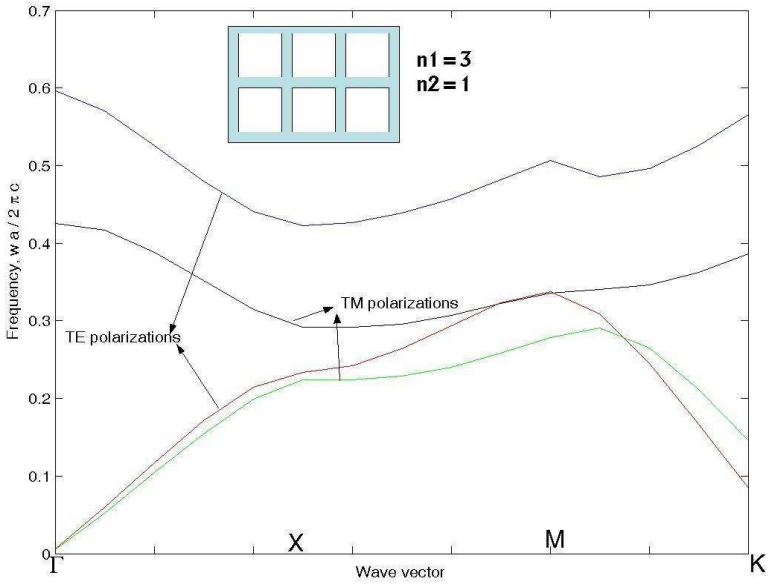

Fig. 2.19 Polarization dependence of Band Gap formation

2.5.2.2 Modes in 2-D crystals

Mode solutions are essentially important in two dimensional crystals for the examination of the defect modes and their decay rates. Therefore, the proceeding sections are meant for the theoretical calculation of the modes in finite crystals. The modes for distinct two dimensional periodic arrangements are going to be laid down and discussed.

2.5.2.2.1 Field Equations

Photonic Crystals can be thought as an intermediate media with certain transmission and reflection coefficients. Then, analogous to the plane wave expansion method, fields can be expanded in different regions [12].

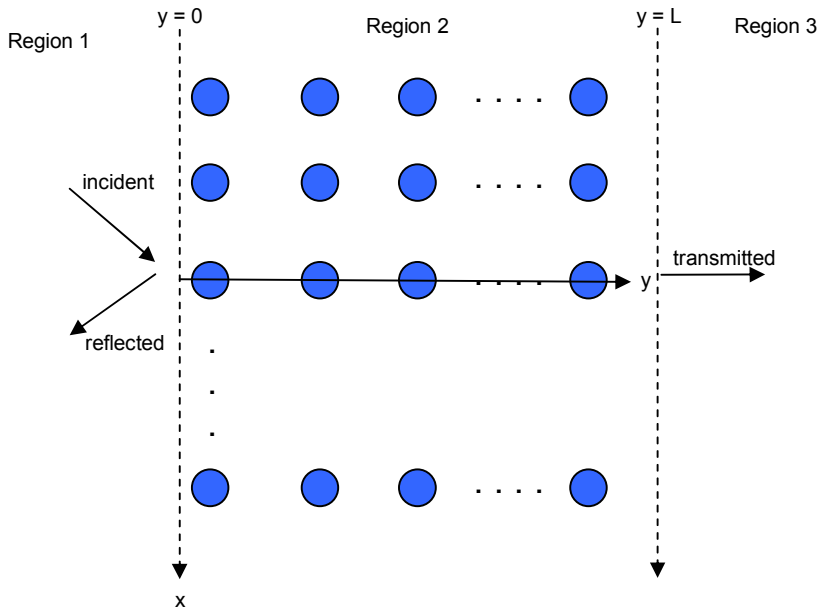

Fig. 2.19 Fields in 2-D crystal

$$E_{1,z}(x,y) = E_0 \exp(ik_i.r_{//}) + \sum_{n=-\infty}^{\infty} R_n \exp(ik_r.r_{//})$$
$$E_{3,z}(x,y) = \sum_{n=-\infty}^{\infty} T_n \exp(ik_t.(r_{//} - L)) \quad (2.28)$$

where E_0, R, T are amplitudes of the electric field of the incident wave, the reflected Bragg waves, and the transmitted Bragg waves respectively. If we define a function as

$$\begin{aligned} f(x,y) &= \frac{1}{L}\sum_{n=-\infty}^{\infty}\{yT_n + (L-y)(\delta_{n0}E_0 + R_n)\}\exp(ik_x x) \\ f(x,0) &= E_{1,z}(x,0) \\ f(x,L) &= E_{3,z}(x,L) \end{aligned} \tag{2.29}$$

such a definition could ease our job by

$$\begin{aligned} &\Psi(x,y) = E_{2,z}(x,y) - f(x,y) \\ &\zeta_E\psi(x,y) - (\frac{w}{c})^2\psi(x,y) = \zeta_E E_{2,z}(x,y) - (\frac{w}{c})^2 E_{2,z}(x,y) - \zeta_E f(x,y) + (\frac{w}{c})^2 f(x,y) \\ &\psi(x,0) = \psi(x,L) = 0 \end{aligned} \tag{2.30}$$

A function sustaining these boundary conditions could be in the form of

$$\begin{aligned} \psi(x,y) &= \sum_{n=-\infty}^{\infty}\sum_{m=1}^{\infty} A_{nm}\exp(ik_x x)\sin(\frac{m\pi}{L})y \\ \frac{1}{\varepsilon(x,y)} &= \sum_{n=-\infty}^{\infty}\sum_{m=1}^{\infty}\kappa_{nm}\exp(i(G_n x + \frac{\pi m}{L}y)) \end{aligned} \tag{2.31}$$

Then writing down the boundary continuity equations of the tangential electromagnetic fields we have 3 sets of equations to extract our coefficients, A_{nm}, R and T.

$$\begin{aligned} &(\frac{w}{c})^2 A_{nm} + \sum_{n'=-\infty}^{\infty}\sum_{m=1}^{\infty}\{(k_x{}^{n'})^2 + (\frac{m'\pi}{L})^2\}\times\{\kappa_{n-n',m+m'} - \kappa_{n-n',m-m'}\}A_{n'm'} \\ &= \frac{-2w^2}{\pi c^2}\frac{(-1)^{m-1}T_n + R_n + \delta_{n0}E_0}{m} \\ &+ \frac{2}{\pi}\sum_{n'=-\infty}^{\infty}(k_x{}^{n'})^2\sum_{m'=1}^{\infty}(-\kappa_{n-n',m+m'} + \kappa_{n-n',m-m'})\times\frac{(-1)^{m'-1}T_{n'} + R_{n'} + \delta_{n'0}E_0}{m'} \end{aligned} \tag{2.32}$$

$$\pi\sum_{m=1}^{\infty} mA_{nm} = (iLk_{r,y} + 1)R_n - T_n + \delta_{n0}E_0(iLk_{1,y} + 1)$$
$$\pi\sum_{m=1}^{\infty} m(-1)^m A_{nm} = R_n + (iLk_{t,y} - 1)T_n + \delta_{n0}E_0 \quad (2.33)$$

In the actual numerical calculation we restrict the number of terms that appear in the Fourier expansions as it has been done for the photonic band calculations. The values, A_{nm} are the same coefficients used in PWEM for the electric field ($A_{n1,n2}$ as given in eq. 2.24). Once the band calculations are successfully realized, eq. 2.32 and 2.33 can easily be solved to find the reflection and transmission coefficients as well as to plot the mode profiles. In the following part we will be studying mode profiles that have been plotted using Ref. 44. The MATLAB realization has been left as a future work.

2.5.2.2.2 Modes

Sufficient amount of factors give away such field diagrams shown in Fig. 2.20.

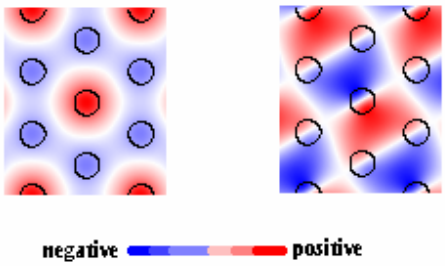

Fig. 2.20 Electrical Fields in lowest bands of Square Lattice rods at point K, {-1/3,1/3} for TM polarization [44]

The origin of the bands can be explained just by examining the modes. The lowest mode is concentrated within the dielectric rods to minimize its frequency. The next bands, in order to be orthogonal, are forced to have a node within the rods, imposing a larger eigenfrequency, hence cost a gap. A triangular lattice structure has been examined and the index contrast has been taken to be 3, considering the background as a reference point. As already discussed a TM polarized

electromagnetic wave would split up band gaps for this configuration. Then we could define a parameter called filling factor, which is

$$f = \frac{\int_{V=highindex} E^*(r).D(r)d^3r}{\int_{V=all} E^*(r).D(r)d^3r} \tag{2.34}$$

The filling factor for TM polarizations is 0.9235 and 0.6449 for consecutive bands. Filling factor is an indicator of the band gap width as well. The filling factors for different polarizations are shown in Table 2.3.

	TM	TE
Band1	0.9235	0.0235
Band2	0.6449	0.3769

Table 2.3 Filling ratios for different polarizations

2.5.2.3 Defects in 2-D crystals

Planar localization of the light can be achieved by defects in two dimensional crystals. Defects can be employed to build many analogous components that are already available in integrated optics literature. Starting from the simplest case of cavity modes, many possible devices that can be constructed with defects are going to be clarified.

2.5.2.3.1 Tunable Cavities

Tunable cavities are the one of the most significant part of the thesis. The working principles of the proposed sensor configurations have been relied on the tunability of the cavity modes. As mentioned in the last section, we can universally say that a defect in the crystal pushes states into the forbidden gap. That phenomenon exactly works in two dimensions as well. When a rod is removed out of the square lattice of alumina rods ($n_{alumina}$=3.13), then the band structures will look like

Fig. 2.21. The modes will be almost fully localized around the defect site. Fig. 2.22 shows the localized mode and %58 percent of the power will be residing within one lattice site when computed. The field amplitudes are arbitrarily normalized in respect to the incident wave. It is apparent that the mode will not be supported by the crystals and is bound to decrease exponentially whilst leaving the defect site. The defect band is sharp with respect to the continuous bands.

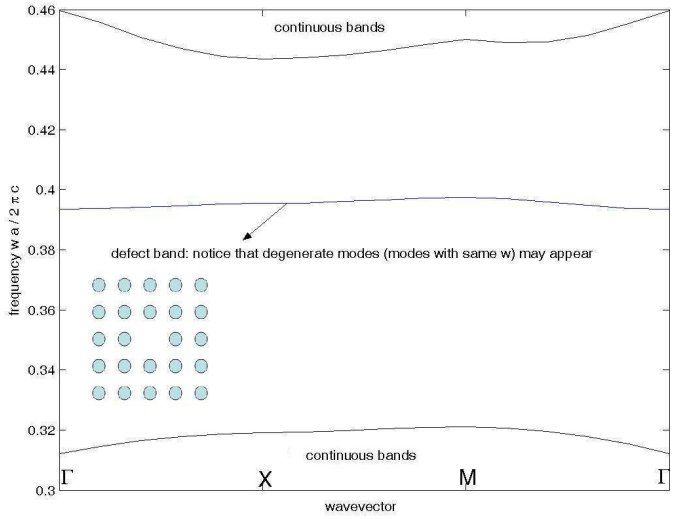

Fig. 2.21 Defect Band in Square Lattice. Compare with Fig. 2.16 and note that band edges have not moved

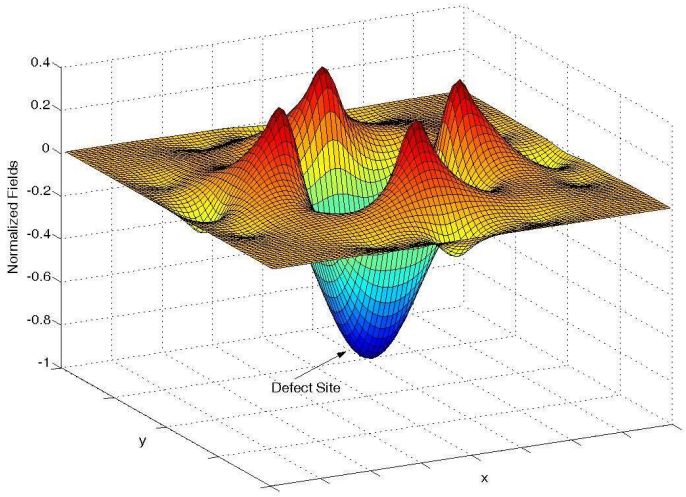

Fig. 2.22 Localization of the modes at the defect site [44]

The most important feature of the photonic cavities is that the designated defect frequency can easily be tuned in terms of both geometric and material dependent parameters at the defect site. For the same lattice configuration, Fig. 2.23 and 2.24 illustrate the tunability range of the Photonic Crystal using a single defect site.

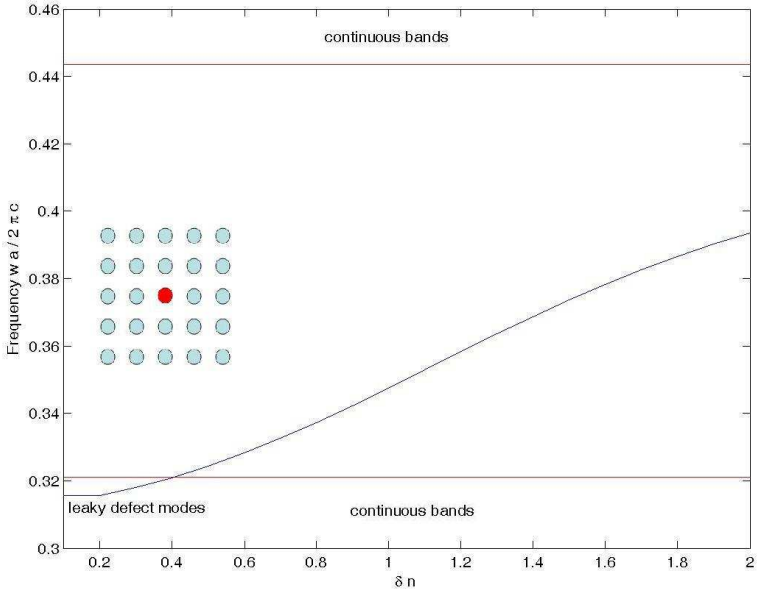

Fig. 2.23 Defect Tuning by index modulation. $n_{rods} = 3$, $r_{rods} = 0.2a$

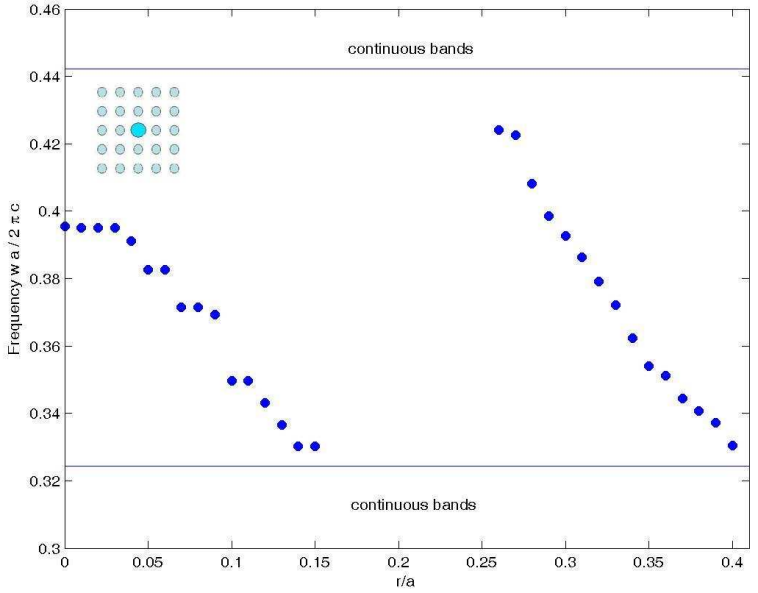

Fig. 2.24 Defect Tuning by size modulation. $n_{rods} = 3$, $r_{rods} = 0.2a$

We have selected the micro cavity structures for our sensor designs for their large range of tunability and sensitivity. The response of the cavities with respect to the either size or index modulation almost outputs a linear behavior. Sometimes they are also referred as linear defects. The modulation takes a band out of the continuous bands and places it inside the band gap. However as it can be depicted from the figures above that the modulation may not be sufficient to lift up the band into the forbidden region or it might directly be responsible for the defect band to reenter the continuous region. Such modes can still be called defect modes, but they will not be perfectly confined at the defect site. Surrounding Photonic Crystal medium will not act like a totally localizing mirror and modes will be leaking into the lattice structure.

These have been the fundamental characteristics of defects. Many interesting devices can be manufactured onwards.

2.5.2.3.2 Want to play LEGO?

Several contemporarily available devices in the photonics market can be built by Photonic Crystals. Here is an outline of the famous ones.

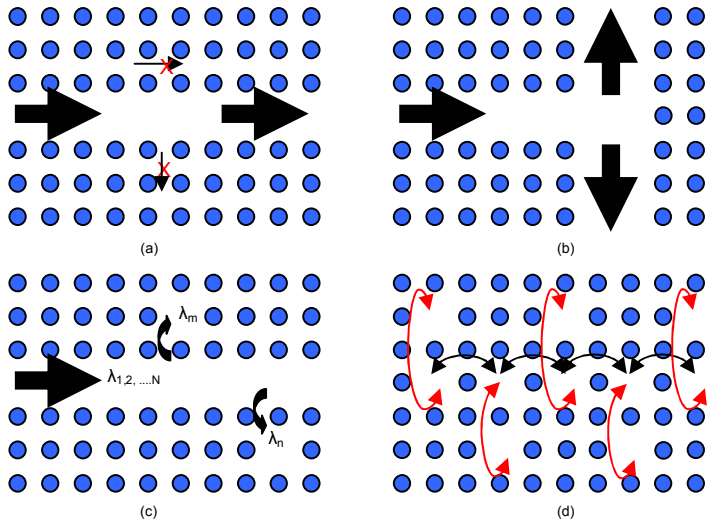

Fig. 2.25 Build anything you want (a) waveguide (b) beam-splitter (c) band drop-filter (d) coupled resonator optical waveguide (CROW)

Alternating defects on a line form waveguides as it can be seen in Fig. 2.25(a). Then, several waveguide based devices in Integrated Optics are feasible. Single mode waveguides, very similar to their counterparts in Integrated Optics have already been fabricated. Yet, their working mechanism does not depend on the total internal reflection. The line defect in Photonic Crystal waveguides support a range of distinct defect bands which are not allowed to propagate in the crystal. Losses due to the absorption in the cladding layers are minimized. Typically, only material dispersion relations become important for the waveguide. This brings simplicity to the calculations by reducing the non-linear effects. Since we can control and guide the electromagnetic waves in the waveguide by simple geometrical modifications, radiation losses are tremendously decreased. Localized wave will not be able to escape outside in the form of radiation.

Beam splitters or in other words, power dividers are feasible to create as well. The amount of power splitting ratio can be controlled with additional defects. Mechanically controllable switch designs can be proposed [45].

Band dropping can be managed by simple tuned cavities that are in the vicinity of the waveguide. Cavities filter out wavelengths out of the waveguide. As we have witnessed, selectivity of the cavities are reliable to distinguish in between relatively close frequencies. These magnetic waves either can be trapped in high quality cavities or can be further guided into other waveguides [46-48].

Cavities that are near enough to each other can form waveguides. The wave coupling from one cavity to another permits the electromagnetic wave to hop from one defect site to the following defect site. The working mechanism is governed by simply coupled-mode theory. In Fig. 2.25 (d), if we call the horizontal cavities as a_n and vertical ones as b_n, then we can crudely write the following (ignoring the losses), where w_A, w_B are cavity tuned resonance frequencies and α and β are the coupling

$$\begin{aligned} \frac{da_n}{dt} &= iw_A a_n + i\alpha(a_{n-1} + a_{n+1}) + i\beta b_n \\ \frac{db_n}{dt} &= iw_B b_n + i\beta a_n \end{aligned} \tag{2.35}$$

coefficients in between *a* type cavities and *b* cavities. Then it can be proved by ignoring the contributions of the *b* type cavities that the frequency band of the waveguide formed by the alternating *a* type cavities can be represented by

$$w_{A,k} = w_A + 2\alpha\cos(kl) \tag{2.36}$$

In terms of the waveguide's frequency band, the system's overall eigenfrequency can be calculated. Photonic Crystal contains two distinct eigenfrequencies.

$$w_{\pm}(k) = \frac{1}{2}\left\{w_{A,k} + w_B \pm \sqrt{w_{A,k} - w_B + 4\beta^2}\right\} \tag{2.37}$$

It turns out that rather than solving the complicated expansion coefficients for the two dimensional structures we can express the *w-k* band diagrams as a function of the properties of the smaller sub blocks, in our case the micro cavities of *a* and *b* type have been enough, together with their respective coupling coefficient.

Exciting unique experiments can be carried out when we modulate the micro cavities. Some research groups have recently been working on intriguing ideas like stopping and storing of light coherently. The main concept is based on the evolution of the group velocity of the electromagnetic wave ($dw_{\pm}(k)/dk$) whilst the microwave index modulation takes place [46].

Limitless number of designs and applications are viable with the introduction of defects into the crystal structure. All we need is a two dimensional array and an intelligent suggestion.

2.5.2.4 Surface Waves and Out-of Plane Propagation

So far we have again considered polarized electromagnetic waves propagating on a plane orthogonal to the polarization vector, in infinitely extended crystals. However, we live in a three dimensional world and our structures must be compatible to finite terminated crystals. In real life, aside from theoretical calculations, surface

localized planar modes might appear at the termination positions of the crystal. Analogous to the case in one dimension, a defect mode can be created that is imprisoned at the surface. Modes that decay in both crystal and in air can be analyzed for different application fields.

As stated before, the homogenous media will not be able to scatter the waves to form band gaps. Hence three dimensional crystals are vital for the examination of the randomly polarized waves. Plane waves have been specifically chosen to investigate in two dimensional crystals, but then we can not generalize our solutions for other instances. This might be disturbing, and has been a motivation to search for ways to deal with the third dimension.

We have tried to summarize almost all the theoretical aspects of two dimensional crystals. In the proceeding parts, methods of controlling the propagation of electromagnetic waves in all possible dimensions will be discussed.

2.5.3 Road to Three Dimensional Crystals, Photonic Crystal Slabs

Three dimensional crystals are useful, but difficult to manufacture. Even though nothing can replace them totally, people have looked for other ways to overcome the problem of confining the waves in the third dimension. No clarification seems to bring full band gaps. Therefore, a trade-off decision has to be taken. The necessity of full band gaps has also been discussed. It has been elucidated that full gaps are not a great restriction to build new optical devices. Nevertheless, the structures must be designed with precautions. The coupled waves are no longer going to be classified as TE or TM modes, and there will be no way of traditionally defining the band gaps in Photonic Crystal slab structures.

Research group at MIT has been one of the first teams to carefully study the Photonic Crystals Slabs and this subsection has been a quick summary of the theoretical backgrounds of the working mechanisms of Photonic Crystal Slabs. There have been recently quite a lot of methods to model them [49-52]. These modeling techniques will be briefly delivered and interpreted.

2.5.3.1 What happens in the third dimension?

We have already seen the band diagrams in two dimensional case when $k_z = 0$. This has been sustained by taking the material to be homogenous in the third dimension. Plane waves were enough to explain the band diagrams. In spite of that, with the addition of k_z value, we will be destroying the full band gaps that we had obtained in two dimensions.

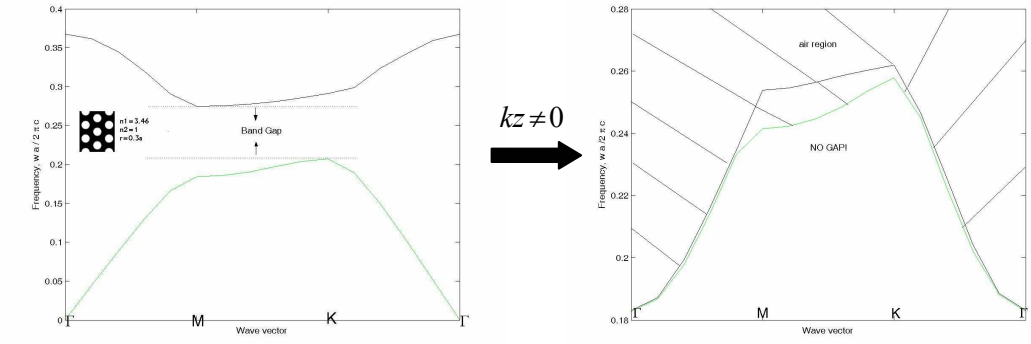

Fig. 2.26 Projection onto the third dimension [44]

However, it must be reminded that these bands are the full projection of the bands onto the third dimension. That involves a slight modification of the plane wave expansion formulas. The existence of the band gap disappears and band extends into air region where bands are continuous.

Before the treatment of the Photonic Crystal Slab, the radiation eigenmodes in uniform dielectric slabs have to be examined. For a slab structure shown in Fig. 2.27, when we examine the TE modes, we can write the following equations.

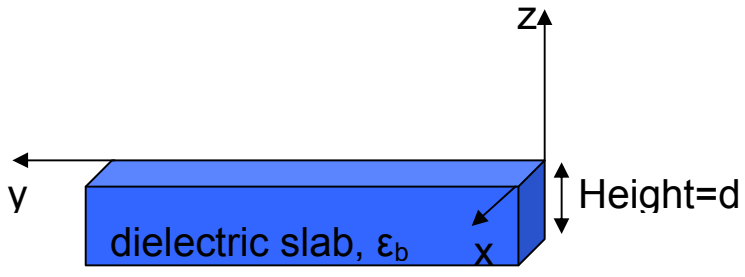

Fig. 2.27 Photonic Crystal Slab

$$E_1 = \begin{pmatrix} 0 \\ E_{1y} \\ 0 \end{pmatrix} \exp(i(k_{//}x - wt))\cos(k_z z) \ldots -d/2 < z < d/2$$

$$H_1 = \frac{E_{1y}}{iw\mu_0} \begin{pmatrix} k_z \sin(k_z z) \\ 0 \\ ik_{//} \cos(k_z z) \end{pmatrix} \exp(i(k_{//}x - wt))$$

$$w^2 = \frac{c^2}{\varepsilon_b}({k_{//}}^2 + {k_z}^2) \tag{2.38}$$

$$E_2 = \begin{pmatrix} 0 \\ E_{2y} \\ 0 \end{pmatrix} \exp(ik_{//}x - \kappa z - iwt) \ldots z > d/2$$

$$H_2 = \frac{E_{2y}}{iw\mu_0} \begin{pmatrix} \kappa \\ 0 \\ ik_{//} \end{pmatrix} \exp(ik_{//}x - \kappa z - iwt)$$

$$w^2 = c^2({k_{//}}^2 - \kappa^2), \kappa > 0$$

Of course, these equations are only valid for even modes, which are symmetric with respect to z axis. Then the continuity of the tangential components reveals an equation where the determinant of the coefficients vanishes and we have a non-trivial solution.

$$\kappa \cos(\frac{k_z d}{2}) - k_z \sin(\frac{k_z d}{2}) = 0 \tag{2.39}$$

Then κ is the attenuation constant for guided modes in the slab. If we solve the even modes of TE polarizations we encounter such a dispersion relation as demonstrated in Fig. 2.28.

By intuition we can understand that some of the modes will be guided inside the slab. These guided modes will not be coupled into the air regions and there will be some sort of a band gap for them. Likewise the unguided modes will not be coupled into the slab itself. There will be a clear cut distinction in between these two kinds of propagating modes. While the modes are traveling in the x-y plane, the guided modes

will be confined in the third dimension due to the total internal reflection. Another thing to notice would be that higher order wave vectors are strongly guided in the slab.

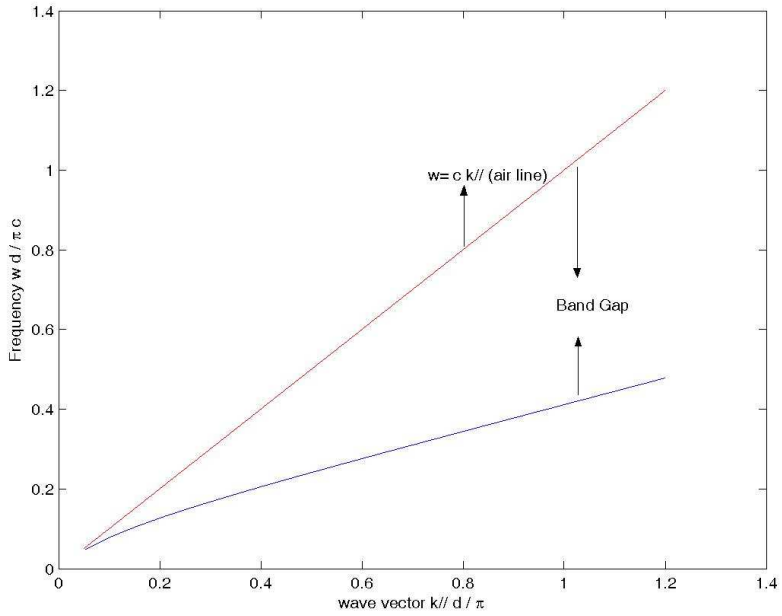

Fig. 2.28 Dispersion relations for the slab, $\varepsilon_b = 2.89$. Notice that Frequency values have not been calculated around $k_{//} = 0$ because of computational difficulties

When our two dimensional Photonic Crystal structure is carved into (or out of) the slab, Photonic Crystal Slab with a finite thickness is created. The band diagrams can be solved by applying the degenerate time independent perturbation theory of quantum mechanics [51]. Briefly, along the z direction ε of the slab is assumed to perturb the states.

$$\frac{1}{\varepsilon_r(z)} = \frac{1}{\varepsilon_{un}(z)} + \frac{1}{\varepsilon_{pe}(z)}$$

$$\nabla \times \frac{1}{\varepsilon_{un}(z)} \nabla \times h_0(z) = (\frac{w}{c})^2 h_{0n}(z), H_0(z) = \sum_{m=1}^{n} a_\alpha{}^{(0)} h_{0m} \ldots ZerothOrder \qquad (2.40)$$

$$M_{i,j} = \int d^3 z h_i^*(z).\nabla \times (\frac{1}{\varepsilon_{pe}(z)} \nabla \times h_j(z), \sum_{\beta=1}^{n} a_\beta{}^{(0)} M_{0\alpha,0\beta} = (\frac{w^{(1)}}{c})^2 a_\alpha{}^{(0)} \ldots FirstOrder$$

$$-\sum_{i,\alpha,\beta} \frac{(a_\alpha{}^{(0)})^* M_{(0\alpha)i} M_{i(0\beta)} a_\beta{}^{(0)}}{w_i{}^2/c^2 - w_0{}^2/c^2} = (\frac{w^{(2)}}{c})^2 \ldots SecondOrder$$

Then the dispersion diagrams will look like Fig. 2.29.

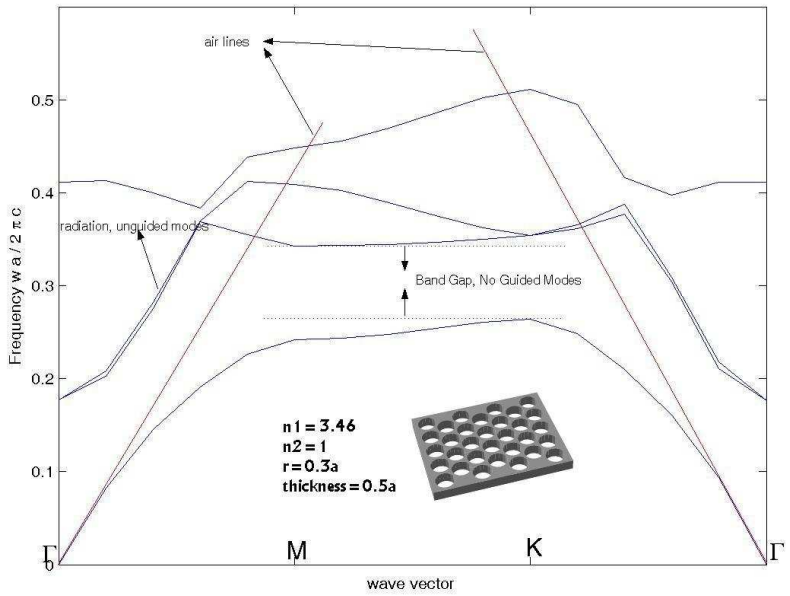

Fig. 2.29 Band Formations for the Photonic Crystal Slab [44]. Even polarization.

We have been dependent on MIT's software that can simulate the projected band diagrams of the first Brillouin Zone. MIT's software computes eigenstates of the slab using preconditioned conjugate-gradient minimization of the Rayleigh quotient in a plane-wave basis [52].

2.5.3.2 Do we really need a complete band gap?

The band diagrams show that we can still talk about a legitimate band gap formation. However, a band gap in this case is a range of frequencies in which no guided modes exist. It is not a true band gap because there are radiation modes at those frequencies. The lines that separate the band diagrams are called air lines. The modes below the air cone are guided bands in the slab. The traditional complete band gaps are not possible in the third dimension. Hence our states are classified according to their symmetry along the z axis. The TE polarizations resemble the even modes whereas odd polarizations can be considered to be similar to TM polarization states.

The slab thickness plays an important role in determining whether the photonic crystal slab has a band gap in its guided modes. Fig. 2.30 shows the variation of the gap size as a function of slab thickness for the very same slab topology whose band diagrams are drawn in Fig. 2.29.

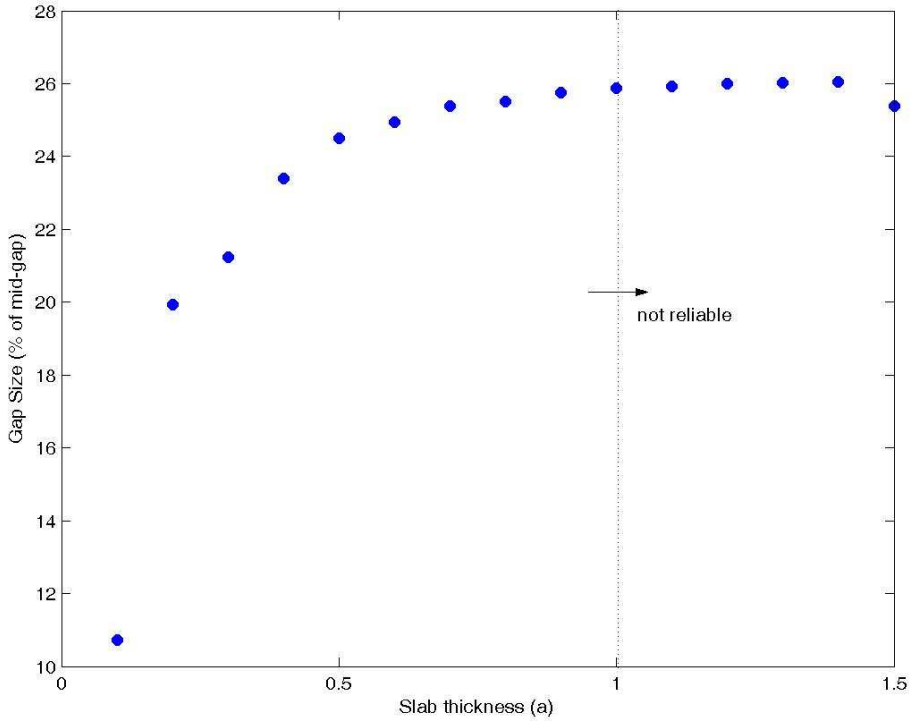

Fig. 2.30 Slab Thickness vs Gap Size [44]

When the slab is too thin, it will bring a very weak perturbation to the environment, such that no guided modes will appear. On the other hand, if the slab is too thick, then higher order modes will be created easily. The slab will behave as if it is a bulk material, destroying all the gaps.

Notice that computations after a certain thickness may not be reliable totally due to computational assumptions that will be described in the next chapters. The gap size seems to be almost constant after d = 0.5a. Then, it would be proper to choose that value rather than seeking for a larger gap size with a larger thickness. Another significant thing is that gaps close to the air lines are roughly in resonance with the

unguided bands. The most appropriate way would be to design our devices close to M and K where modes are strongly guided.

Although it will not be proven here, the first band of the Photonic Crystal Slab is an extension of the solutions in the two dimensional case. They constitute the ground states for the electromagnetic waves and are assured to lie under the air cone. The air lines are also defined to be tangential to the first band. The first band decides the width of the air cone and is strategically important.

2.5.3.3 Defects in Photonic Crystal Slabs

In spite of everything, defect structures based on the shrinking of rods or faults in crystal slabs are feasible, yet they are not so easy. Radiation losses are inevitable. The guided defect modes will be coupled to the air cone.

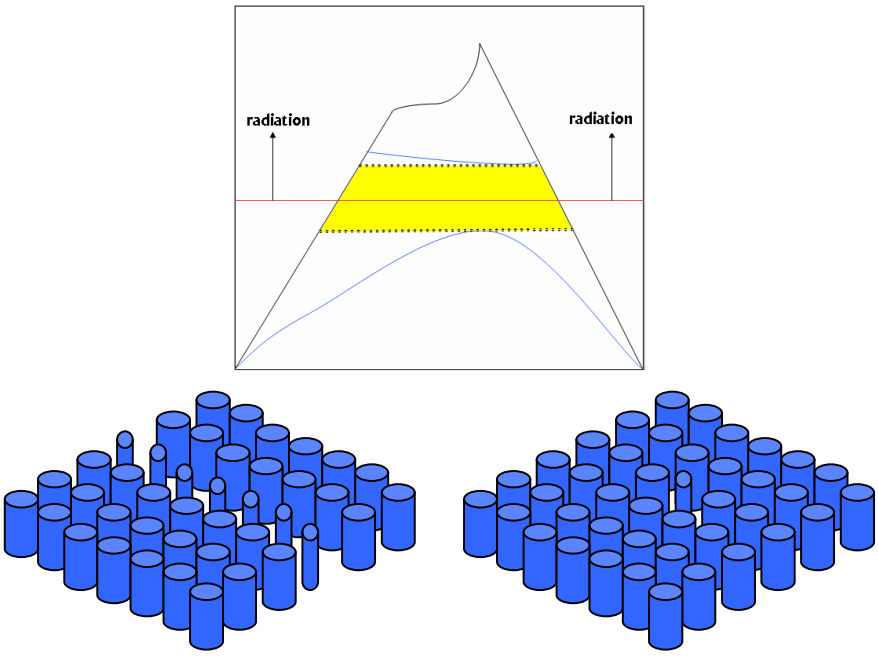

Fig. 2.31 Photonic Crystal Defects

Since the index guiding can not be sacrificed in the third dimension, the rods can not be totally removed. The situation is similar for the etched PCs. Light is contained inside the slab by two different mechanisms, total internal reflection (TIR) in the third

dimension and Bragg scattering on the planar surface of the periodic structure. Consequently, people can not avoid losses, so cavities with very high quality factors are favored in the literature [53,54].

Quality factor of a defect is the measurement of the energy possessing character of the configuration. It can be calculated with methods like Finite Difference Time Domain Method (FFTD) which is explained in details in Ref. 31. We did not have a computational tool to measure the time evolution of the electromagnetic fields in photonic crystals, and comparisons in between different results have not been performed. However it should be mentioned that FFTD yields better convergence in comparison to field expansion methods, and it has been widely accepted among the Photonic Crystal research groups all over the world.

2.5.4 Three Dimensional Photonic Crystals

Finally, the last type of crystals that will be of our concern will be three dimensional Photonic Crystals. The remaining part of our section will be devoted to their examination. This thesis is not directly related with their design topologies and defect formations, so just the references will be given for any further inspection. This does not mean that localization of defect modes or confined surface states are not reported. Three dimensional structures may be the heart of all applications in the near future, but they are just out of this thesis's scope for the current being.

2.5.4.1 Distinct, Manufactured Three Dimensional Crystals

The first kind that was predicted to show complete three dimensional band gap was a diamond lattice of spheres (Fig. 2.8). As long as the sphere radius is chosen correctly, band gaps would exist. Another proposal suggests that the dielectric rods form a complete gap when they are designed to be connected to each other [55]. Fig. 2.32 illustrates configurations.

2.5.4.2 Band Gaps

Generally speaking, band gaps tend to appear in structures with a high dielectric contrast. The more light is scattered, the more likely a gap will open up. Yet any geometry does not cause band splitting, which would be the case in two dimensional structures. Complete photonic band gaps are rarer for three dimensional arrangements. Drilling the correct dimensions or designing the accurate sizes of spheres is crucial. Fig. 2.33 shows a complete band gap in three dimensions for a face centered cubic lattice with a dielectric constant of 11.56. The radius of the spheres is adjusted to be 0.25a, one quarter of the lattice constant.

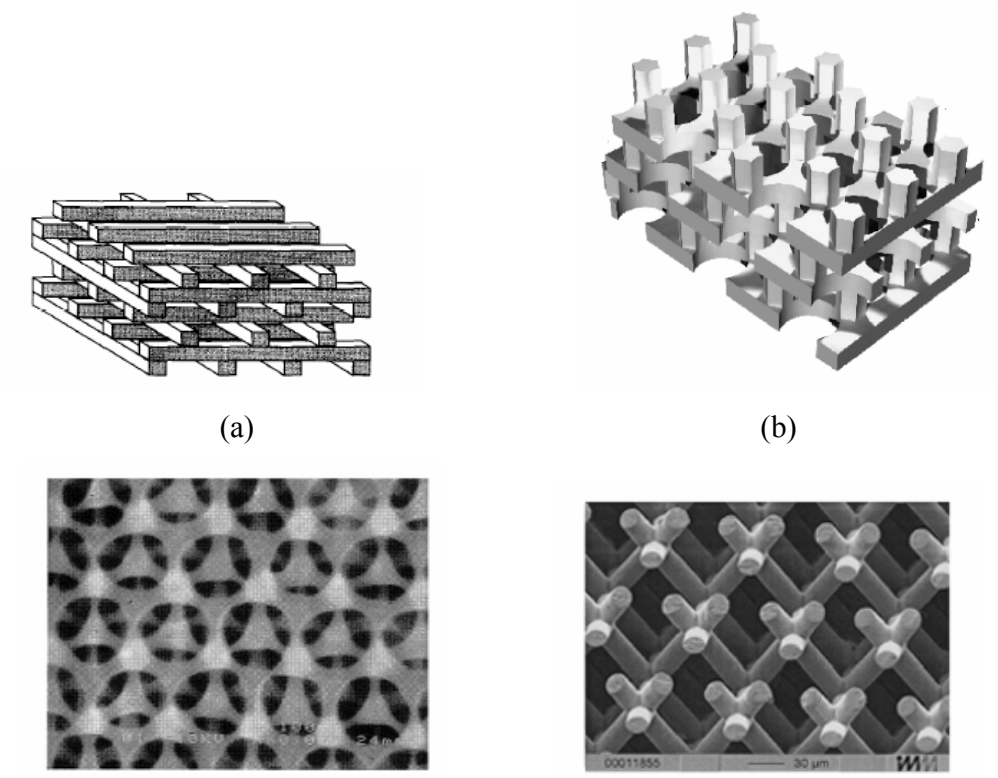

(a) (b)

(c) (d)

Fig. 2.32 Different Three Dimensional Configurations. (a) Rods connected to each other (b) Rods and Holes of 2-D are mixed together (MIT group) (c) Yablonovite, the first device to demonstrate full band gap, named after Yablonovitch (d) Cylinder Structure

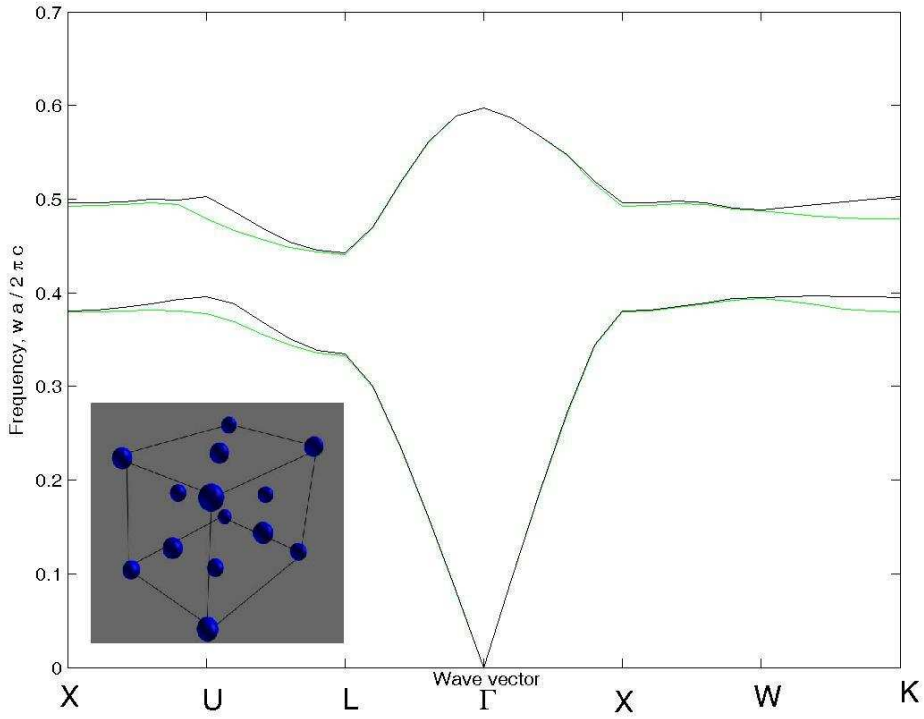

Fig. 2.33 Complete Band Gap in Three Dimensions

2.6 Final Words

Essential theoretical background about especially the two dimensional structures has been lied down. From here, we will be moving and directly focusing on the design strategies that have been applied in the thesis. We will be again referring to many points from this chapter to clarify any problems on theoretical grounds and it is our hope that it will be the verification of why this chapter was claimed to be the heart of the thesis.

CHAPTER 3

COMPUTATION METHODOLOGIES

Even though we had not honestly planned to do a very detailed examination of the conventional computational techniques in Photonic Crystal literature at the beginning, development of new software tools to compute the band diagrams in one and two dimensional problems can be thought as a major outcome of the project. The expensive Photonic Band solvers have been a motivation for this purpose. I have been encouraged to digest every theoretical step and new information by my supervisor. The more I had been attached to the theoretical side, the more I understood the limitations of MIT's Band Package which has been the only Photonic Crystal analyzer software in our hands. MIT's software is relatively easy and user friendly, however it occurred to us that we would only be controlling our designs behind software which puts inaccessible boundaries between the user and the physics of the Photonic Crystals. We do not think that it should be satisfactory for any graduate student in Sabanci University. Furthermore, Photonic Band calculations are widely open to assumptions and crude estimations which may cause intolerable errors.

We led this project from that perspective and attempted to write our codes in order to realize the simulations by using other means of computational tools. MATLAB has been a great candidate to fulfill our intentions with fast matrix manipulation instruments.

In this chapter, we will be discussing both MIT's software and in some ways compare the advantages and the shortcomings of our simulation programs. The chapter is going to start with the introduction of the Band Package program and then proceed with the applications for different configurations in separate topologies. It is apparent that we will have to refer back to chapter 2 at any points involving theoretical equations.

3.1 Introduction to MIT Band Package

MIT's software depends on the plane wave expansion and variation methods that we have already described. It can output spatial distribution of both eigenfields and eigenfrequencies in the form of band diagrams. The mode profiles in the previous chapter had been calculated by this method.

There are many significant parameters in the plane wave expansion. However, the only parameter that can be directly controlled from the script prompt is the lattice resolution constant. We will talk about other factors as we move on, but for now let us concentrate on the lattice resolution variable.

MIT's Photonic Band calculator (MPB) is programmed by Steven G. Johnson and has been an open source that can be downloaded in related pages. MPB is simply coded with C language and is suitable for UNIX operating system. The figure below exhibits the shift in *w*-*k* diagrams due to resolution errors.

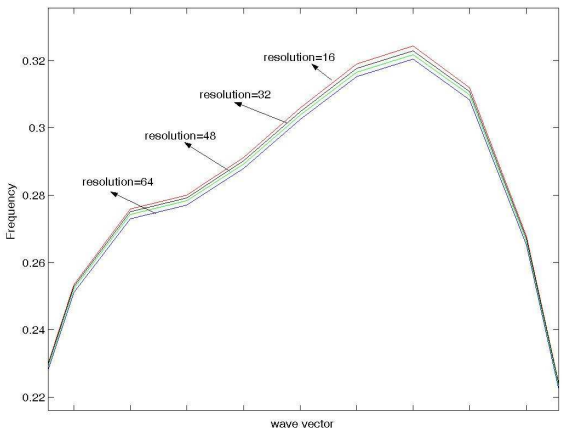

Fig. 3.1 Errors due to lattice resolution

The error percentage between the outputs when resolution is set to 16 and 48 turns out to be around %1.7 at most. This is a tolerable error percentage, but the designer should expand the coefficients within the same resolution constant to expect consistent results for very sensitive devices. The resolution constant is directly responsible for expressing the dielectric function in the unit cell. It meshes the lattice with respect to the assigned resolution constant and computes the $1/\varepsilon(r)$ matrix accordingly. This might bring severe problems as we are going to see in more details.

3.2 One Dimensional Problem

The one dimensional Photonic Crystals have been simulated using two different algorithms. The first methodology has been pointed out in the second chapter and is based on the boundary calculations inside the infinitesimal crystal. This topology will be called as the exact solution because of certain reasons. This method had been submitted in the name of scattering through N-slabs before.

When the lengthy wave expansions and exact solution topologies are concerned, they share the assumption that the dielectric function is alternating infinitely in one dimension. However plane wave expansion (PWE) leads even to more assumptions and thereby errors. For a sufficiently long crystal, exact solutions will definitely be more accurate as long as it does not involve any other suppositions. On the other hand PWE includes other propositions;

a) The dielectric function has to be expanded over a satisfactory amount of harmonics. This means that the unit lattice has to be meshed into adequate number of discrete elements so that the Fast Fourier Transform (FFT) of the lattice is performed with enough contributors. Whatever we do, we would still need infinite number of frequency components to express square waves, so specific amount of error is inevitable.
b) The number of eigenvalues is limited. While writing the electric fields in the Bloch form, we needed to express the fields as an infinitely extended number of expansions. Hence in the computational world we are bounded with finite numbers. This would bring an additional error that is unavoidable as well.

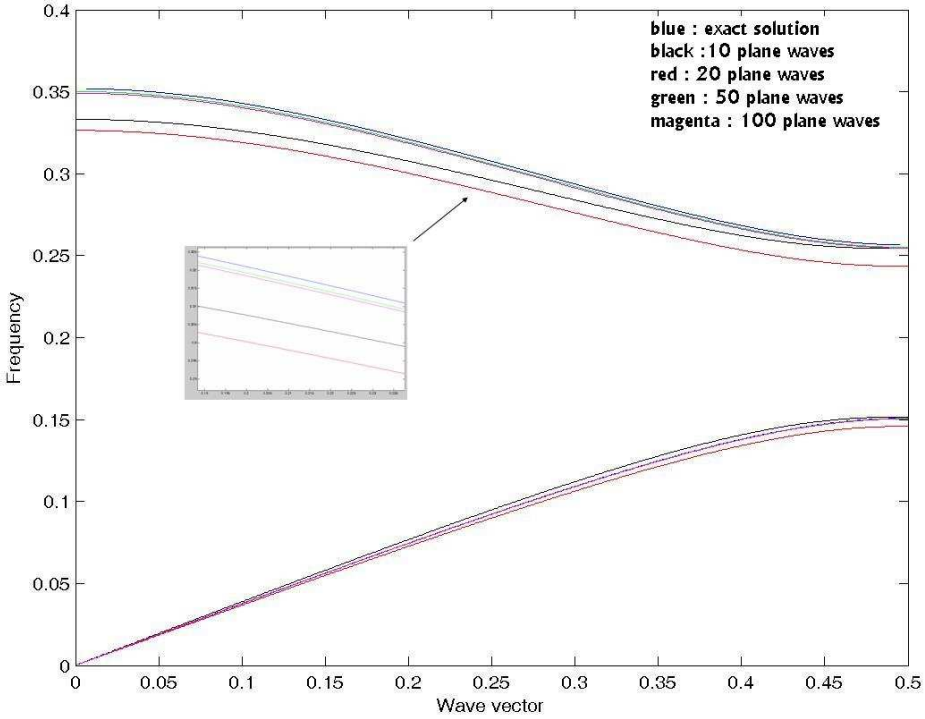

Fig. 3.2 PWE vs Exact Solution for 1-D crystal of $\varepsilon_1 = 13, \varepsilon_2 = 1$

It figures out that rather than the Fourier expansion of the dielectric function, the number of the eigenvalues to be inserted into our equations becomes the bottleneck. As it can be depicted from Fig. 3.2, 50 plane waves are only enough to accommodate for our error percentage in PWE method in comparison with the N-slabs scattering theory. The evaluation done above has been carried out in between two algorithms that have been adapted for the one dimensional problem. If we were to judge among our PWE method and MPB's PWE method, then we can crudely extract a rough idea of how many plane waves they might have used. The situation is portrayed in Fig. 3.3.

Considering the picture below, we can reach several deductions. The most significant one would be that MPB can not converge for better results with limited resolution. Actually it is the outermost line considering the upper band. Besides, solutions approach a saturation point for more than 50 plane waves. The convergence error of 100 and 400 plane waves seems to be on the same scale.

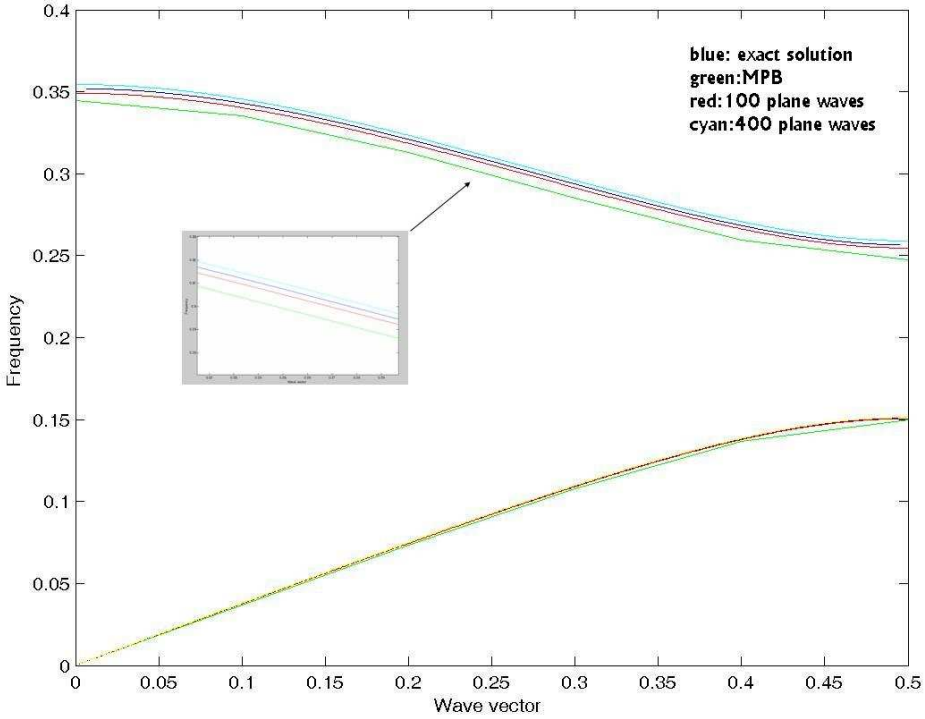

Fig. 3.3 Convergence Problem of MPB

It can be claimed that the number of plane waves in PWE calculations would be much more crucial than the meshing resolution of the dielectric function, unlike Ref. 56. Theoretically, at the limits the meshing resolution of the lattice constant determines the number of plane waves that we can insert into our PWE calculations due to the duality of the Fourier expansion. Eq. 20 is converted into the following finite forms for computational purposes.

$$\begin{aligned} &\frac{1}{\varepsilon(x)} = \sum_{m=1}^{M} \kappa_m \exp(i\frac{2\pi m}{a}x) \\ &-\sum_{m'=1}^{M'} E_{m'}(k+\frac{2\pi m'}{a})^2 \kappa_{(m-m')} = (\frac{w}{c})^2 E_m \end{aligned} \tag{3.1}$$

Here, the number M will be the limiting factor if it is comparable to M'. For very low resolution constants, the band edge of the upper band will become seriously disoriented. But as long as we take M to be a relatively big number, it will not happen

to be the bottleneck. It should be noted that lattice resolution was set to be around 1000 while calculating the examples in Fig. 3.3.

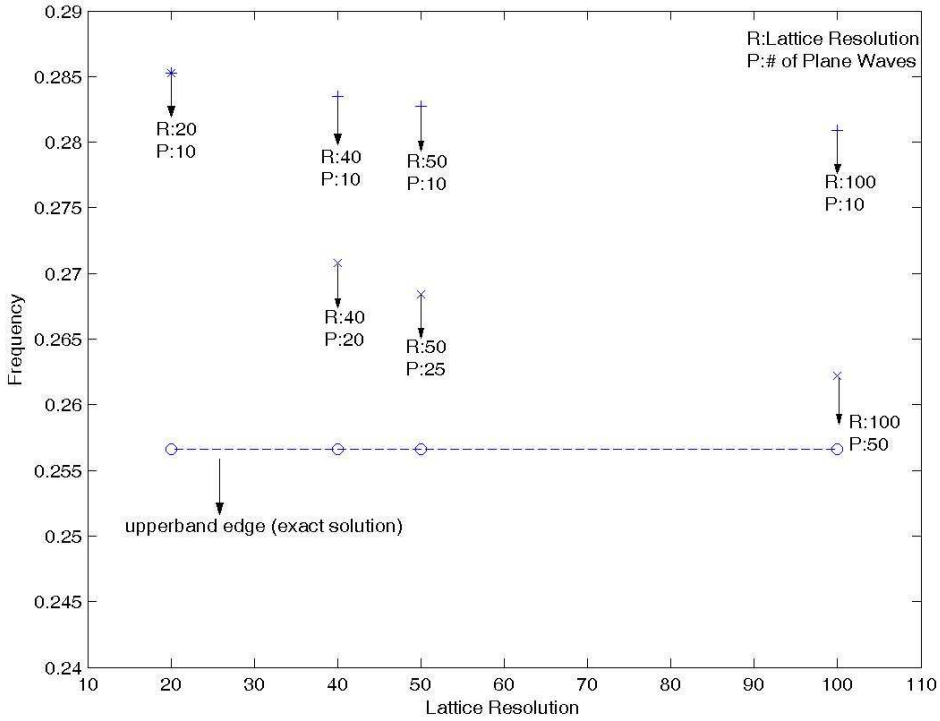

Fig. 3.4 Lattice Resolution vs Plane Wave Number

Such lattice resolution constants are comparatively small to be used in actual calculation. Hence, the influence of the meshing resolution of the lattice (denoted as lattice resolution) is strikingly smaller than the number of plane waves to be computed.

Slow convergence is a big issue that PWE methods suffer from. In Ref. 57 a survey has been accomplished to estimate the error percentage shifts of the upper band as a function of plane wave numbers to be analyzed. The small shift in the figure must be because of the attempts performed in conventionally available PWE methods to treat the dielectric expansion as an independent element. We will be reanalyzing this point, but it must be remarked that people are interpolating even the low resolution lattice representations in order to demolish the direct relationship between the number M and M' in eq. 3.1. This might be a way to avoid the limiting

factor of resolution lattice constant. It also enables us to choose as many plane waves as we desire at low resolutions, nevertheless the improvements coming from larger amounts of plane wave contributions saturate much faster dissimilar to the case in Fig. 3.4.

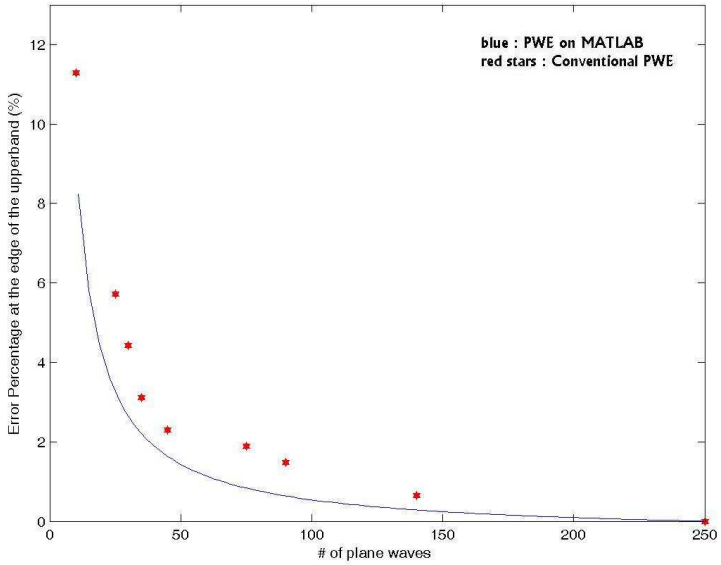

Fig. 3.5 Classical PWE vs PWE on MATLAB for 1D problem

Working at low resolutions might be appealing at first, and it might be attractive as long as the FFT time is reduced considerably. On the contrary, it may cause slow convergence and it should be taken care of. We should note that Fig. 3.5 has been drawn *only* to demonstrate the similarities of error reduction curves between our MATLAB implementation and the classical PWE methods in terms of plane wave numbers. The data about conventional PWE methods has been extracted from Ref. 57, and the slight shift with respect to the MATLAB version should not be necessarily interpreted as a significant superiority of our implementation.

3.3 Two Dimensional Problem

Two dimensional Photonic Crystals have been simulated with both MPB and our PWE methods. Unfortunately, the exact solution's adaptation to the two

dimensional case would be extremely difficult and has not been attempted. Therefore, the main comparisons will be in between these two algorithms.

3.3.1 Computational Differences

It should not be understood that MPB is based on a completely different methodology. PWE is employed to expand the electromagnetic fields, but at the last stage variation method (eq. 2.27) is used to guess the ground state by writing it in terms of the chosen eigenstates. As a result, MPB requires a significant iteration time to converge to a stable saddle point. On the other hand, our software expands the electromagnetic fields (eq. 2.25), the eigenfrequencies are directly found by MATLAB's special eigenfunctions. MATLAB can remarkably handle huge matrices like 961x961 very easily with the help of its internal diagonalization functions. Huge Matrices with dimensions exceeding 1000x1000 is usually the case to minimize the error contributions.

If we were to examine the band diagrams very precisely, then they would look like the following figure.

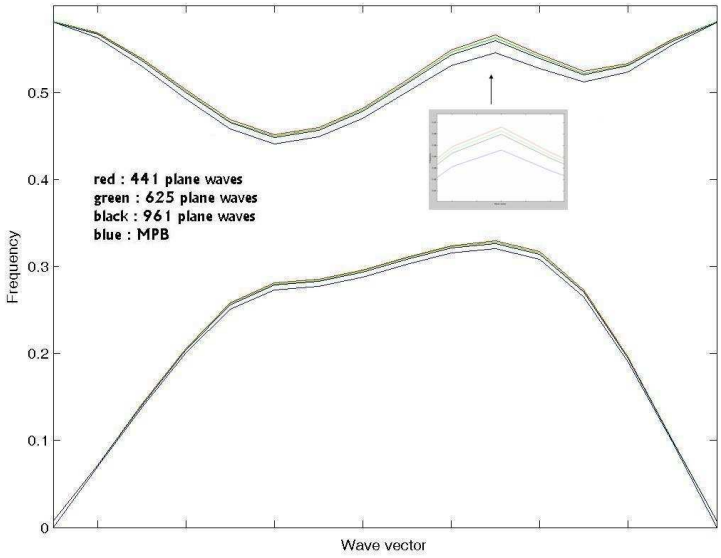

Fig. 3.6 Comparison of MPB with our PWE method in 2-D for $\varepsilon_1 = 9, \varepsilon_2 = 1$

SQ lattice of rods, r = 0.2a

For two dimensional problems, results have been compared for various numbers of plane waves. Since we do not have the absolute control over the parameter, it might be only a speculation for now, but MPB seems to utilize even more than 1000 plane waves. Our results tend to come closer to MPBs' as the number of plane waves is increased.

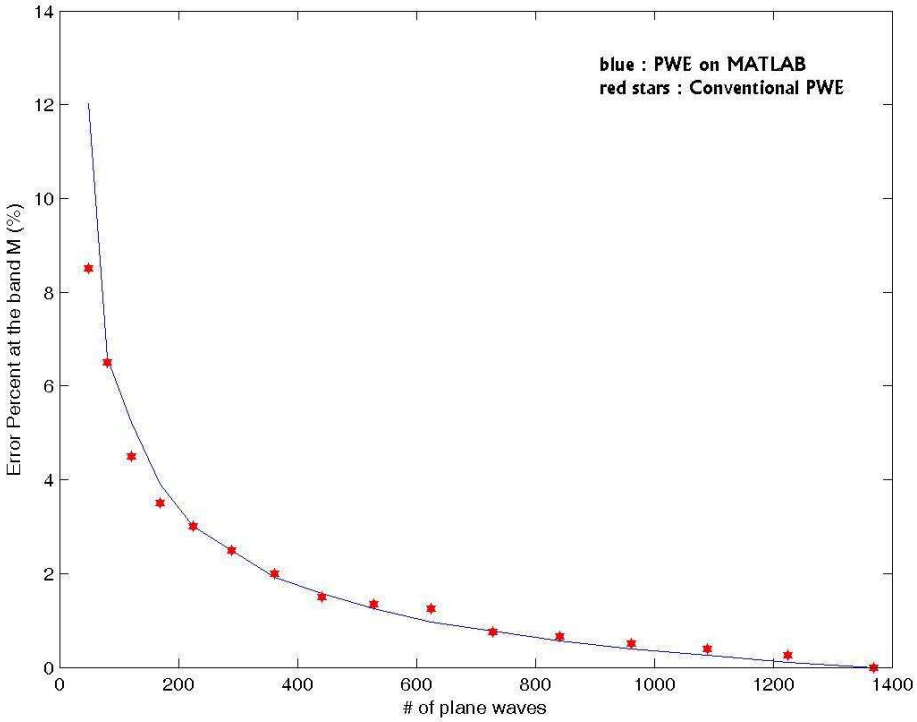

Fig. 3.7 Conventional PWE vs PWE on MATLAB for 2D problem

Again when we compare the conventional applications with our software [57], it can be seen that our algorithm roughly coincides with the band solver solutions available in the market. Researchers are discussing and proposing even faster convergences by applying small but useful adjustments to the master eigenvalue equation of 2.4. In most of the cases, a trade of has to be managed in between the time consuming FFT of the lattice structure and the appropriate formulation of the eigenvalue equation. In spite of that, these studies are more related with mathematics and they are out of scope for just now. We are going to be contented with just mentioning these examinations.

3.3.2 Defect Calculations

Defect calculations are very critical for the thesis. In plane wave analysis a method called supercell expansion is frequently used. In this method, the structure shown in Fig. 3.8 is regarded as the unit cell, which is in fact a supercell, and the band calculation by the plane-wave expansion is performed for this unit cell structure. Then defect modes with a very small bandwidth appear in the band gaps.

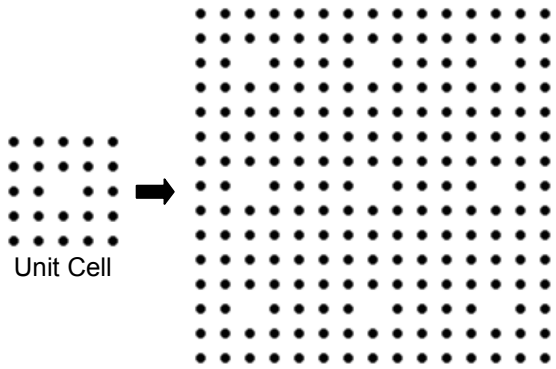

Fig. 3.8 Unit Cells in Defects [44]

The figure above is a typical dielectric output function of MPB. Replicating the supercell by defining a new unit cell might be a neat idea. However it goes along with serious drawbacks. Firstly, we are going to need plenty of new plane waves to reconstruct our computational matrix. This is because, when we extract our unit lattice to create a defect site, we are also recharacterizing the Brillouin Zone by stretching out the irreducible zone's volume N^2, which is 25 for Fig. 3.8. Then the new unit cell's N^2-1 will correspond to the first band edge of the old primitive unit lattice. This means that the band gap will now be starting to appear above the $(N^2-1)^{th}$ band of the new structure. Specifically for the configuration in Fig. 3.8, the defect band will reside at the 25^{th} band. Calculating accurately the bands starting by N^2, require a huge matrix consisting of a lot of plane wave contributions. The nice convergence that we have found in Fig. 3.7 can not be applied anymore. The total computation may entail hours and even days! Fig. 3.9 shows the error ratios and the demanded CPU time to carry out the calculations.

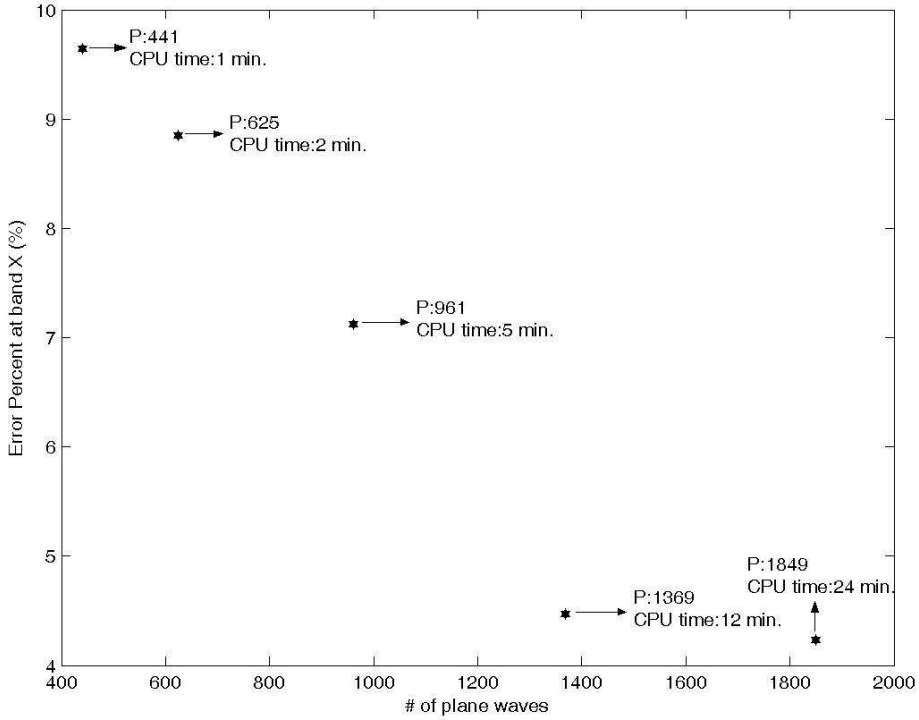

Fig. 3.9 Defect Calculations Errors with respect to No Defect Calculations

Another drawback of superlattice method is the so-called defect to defect modulations. Provided that our defects are separated only by the lattice constant of the superlattices, our results will also include the defect to defect mode coupling factors. In the real world, we would like to have sharp resonances for our cavity designs and defect modulations may not be favored. The defect band should be limited accordingly. Fig. 3.10 is an illustration of the phenomena.

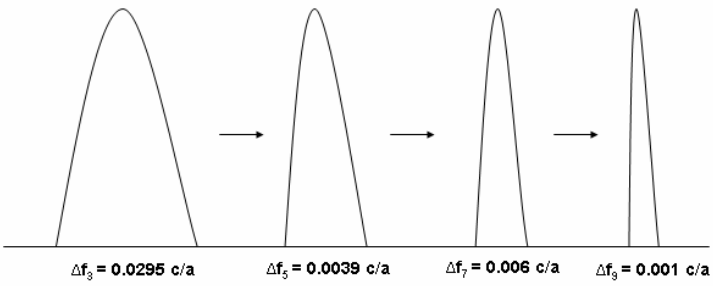

Fig. 3.10 Defect to Defect Modulation

The ideal way to handle the problem is to expand the superlattice indefinitely. Nevertheless, we are bound with the finite memory of the processors. The extension coefficient of the superlattices is inversely proportional to the required CPU time. We would like to avoid the accumulation of thousands of plane waves, if possible. Also, 7x7 superlattices' defect to defect to modulations look to be tolerable.

3.3.3 Further Improvements and Extra Features

PWE method has been modified for MATLAB environment. As it was stated any improvement over the algorithm by readjusting the matrix formulations has not been our essential concern. Yet, could there be any advances from an engineering perspective? The answer to this question has been our driving force.

3.3.3.1 Fast Fourier Transform of the Dielectric Functions

MATLAB can cope with many functions and can produce their n-dimensional Fast Fourier Transforms successfully consuming little CPU time. Regarding that, the respective FFTs' of the one and two dimensional periodic lattices had already been portrayed in Fig. 2.6 and 2.7. If we remind ourselves that $M >> M'$ restriction might be also applied analogously to the one dimensional case in eq. 3.1, then we are free to represent the unit lattices with enormous resolution. Hence, we need not to consider all the expansion coefficients. As a result of the periodicity, the pattern can be recreated from the fundamental and small amounts of harmonics. In Fig. 3.11, high resolution meshed lattices' FFT images were used to maintain the old images. For this specific case, only first 40 harmonics from each side (totally 81 components) have been utilized to convert the lattice dielectric function. Actually Fig. 3.11 also shows why we have to face a lot of trouble with super lattice theory. The single rod could be expressed in terms of dielectric tensors and the single rod image is easily recognizable, whereas the rods with defect structure have not fully gained their shape at the defect site even with 81 components, we are still missing some contributors.

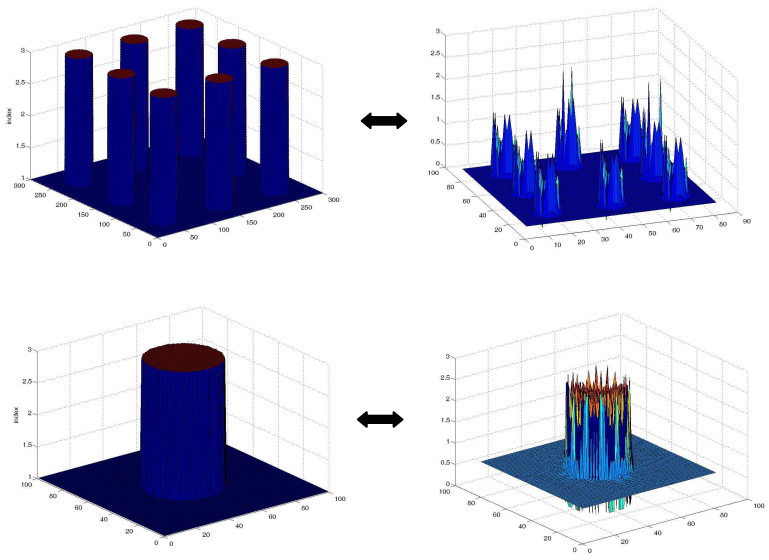

Fig. 3.11 Invertible Images

Based on these ideas, we can ignore the low weighted expansion coefficients to speed up the PWE algorithms. In our software, we omit the coefficients smaller than the adjusted fraction of the DC value. In the eigenvalue problem, this technique decreases the necessary CPU time for evaluations as long as factorization of the matrix gets easier with less elements placed on the matrix.

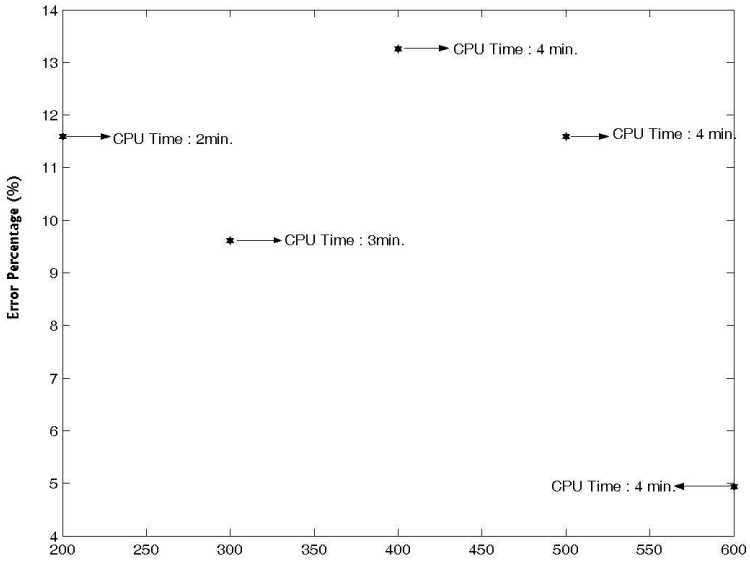

Fig. 3.12 Error vs Tolerance values with respect to No Defect Calculations

A tolerance value has been assigned. This value determines whether a matrix element is going to be inserted into the wave equations or not.

$$\frac{DC}{Tolerance} \leq Harmonic \Rightarrow .inserted \tag{3.2}$$

Then Fig. 3.12 is obtained. For a 3x3 superlattice of square lattice of dielectric rods standing in air, CPU time is decreased from 5 min. to 2 min. as expected. The error values are acquired by comparing the frequency values of the defect bands.

3.3.3.2 Determination of the Phase Shifts

MPB can nicely draw the bands, settling the gaps. The user may interpolate as many wave vector (k) values as she/he desires. However MPB lacks a tool to approximately calculate the phase shifts due to the disturbances in the periodic lattice, which is essentially important for sensor applications in Photonic Crystals.

Any perturbation may alter the band diagrams and an electromagnetic signal propagating through the crystal with a fixed frequency may be compelled to endure certain amounts of phase shifts. The problem contains inverse iterations of band frequencies to estimate the desired k values.

This feature has also been added in our PWE software and is going to be helpful in finding out the sensing capabilities of the Photonic Crystals in the following chapters.

3.4 Photonic Crystal Slabs

Unfortunately, we have been dependent on MPB for the Photonic Crystal Slab solutions. We could briefly mention the drawbacks of Slab solver tool of MPB. The analysis has been clearly done in Ref. 52 that symmetric structures in the third dimension are needed. Any symmetry breakdown along the z axis mixes the odd and even modes, and therefore destroys the band gap for the guided modes. The software

may only accept the following configurations if we had to manufacture the slab structure on a specific substrate. Now, Fig. 3.13 is almost impossible to realize in a micro fabrication facility, still the symmetry in the third dimension is a strict requirement of the software. A secondary substrate has to be added with the same thickness, d. It should be useful to keep these properties in mind during the design and modeling stages.

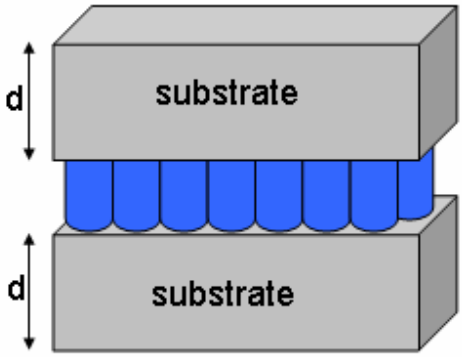

Fig. 3.13 Limitations for MPB's Slab Solver

3.5 Final Words

The implementation of the PWE has especially helped us to understand the electromagnetic field propagation in Photonic Crystals. PWE combines the Bloch vectors of Solid State with Maxwell's equations in electromagnetic theory and still is a powerful tool for the beginners in the field. Band diagrams, mode profiles, defect formations can be explained by this simple theorem which is based on the expansion of the field coefficients in the coordinate space.

In addition to that, our software gives us the opportunity to control other parameters as well. A detailed analysis on the error ranges of PWE, and our awareness of the limitations coming from PWE is going to be our strong points at the design and experiment phase.

CHAPTER 4

DESIGN METHODOLOGY

This chapter will be dedicated to the introduction of the methodology for sensing very small refractive index changes via phase shift of the EM wave as well as the design stages of our proposed devices that we have built utilizing the special features of Photonic Crystals. Two different cavity designs based on two dimensional Photonic Crystals will be presented.

The designs have been both developed specifically for sensing applications. The main idea has been to examine the perturbing effects of the outer disturbances on the Photonic Crystals.

The experiments of the suggested devices and comparisons in between the theoretical expectations and experimental results would be more than convincing. As a result, the design parameters have been chosen in such a way that realization and experimental set-up of the overall structure would not be extremely difficult.

It should also be mentioned that the results have been tried to be optimized in a certain range, but yet even better models with better performance issues could be offered for other particular design criteria (different frequency range, fabrication necessities, with different FDTD tools ...).

Both our PWE tool together with MPB have been employed to generate the theoretical outputs. The output results must always be interpreted considering the

error tolerances of our programs. The fundamental working mechanisms delivered in chapter 2, should be enough to understand the general picture.

In this section, we will start from the selection of the background Photonic Crystal with certain dielectric filling ratio. We will be examining the estimation of the phase shifts of the traveling EM wave due to the band edge modulations. Then we will be proceeding with the design of the point defect site. Coupling the waves into the cavities will be studied and finally the sensing capability of the defect will be examined.

4.1 Background Crystal

The first step in the design should be the determination of the Photonic Crystal topology. There are various choices in two dimensions, like triangular lattice and square lattice configurations of holes or rods as explained in the second chapter. Yet, the topology that we choose here should easily be realizable in our labs. Therefore, we have decided on working with rods rather than any other hole arrangements. This preference is solely based on the fact that it would be easier to construct a perfect crystal with periodically spaced rods, instead of struggling to carve perfect holes into a fairly tall bulk material in the microwave regime. Etched hole configurations would be much more efficient and would yield better results if we had to micro fabricate our designs in optical communication wavelengths.

As for the index contrast, PWE may not converge very well, after $\varepsilon_1 = 10, \varepsilon_2 = 1$. We have tried to work for the case where the results of our PWE and MPB programs agreed the most. Fig. 4.1 shows this phenomenon as the background material, air's index is kept constant, gap size and mid band gap frequencies have been analyzed. We would need a certain amount of gap to let the disturbances swing the defect band freely. The more the index contrast we have the bigger gaps we do maintain. But we can not increase the contrast indefinitely, because PWE methods become liable to errors. Also for the low index contrast case, gap frequencies are really quite high and gap sizes are relatively small to design our cavity structures. Values around 2.7 and 3.2 seem to be suitable for our purpose. Consequently we have chosen our high index

material to have a refractive index value of 3.13 in our cavity designs. Actually this has not been a random choice as well. Alumina rods, which are frequently used in Photonic Crystal literature, have also a refractive index value of 3.13 around 9GHz.

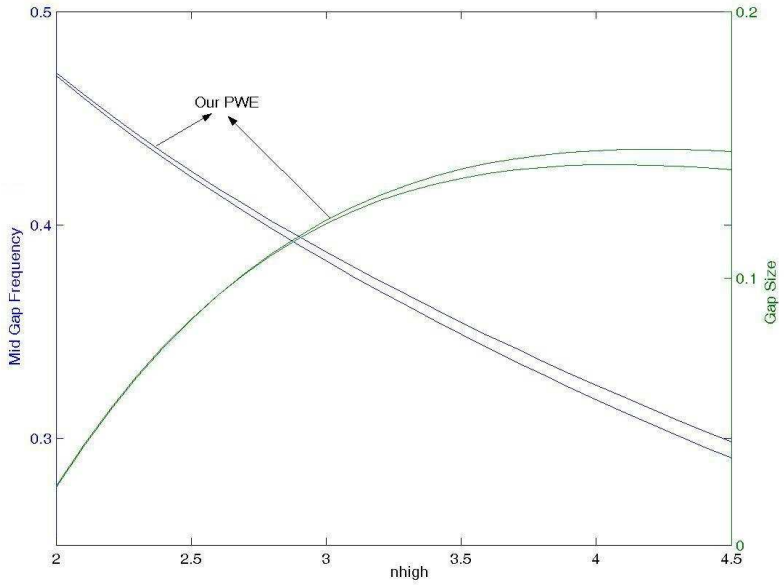

Fig. 4.1 Index Contrast. For SQ rods, r=0.2a, background is air

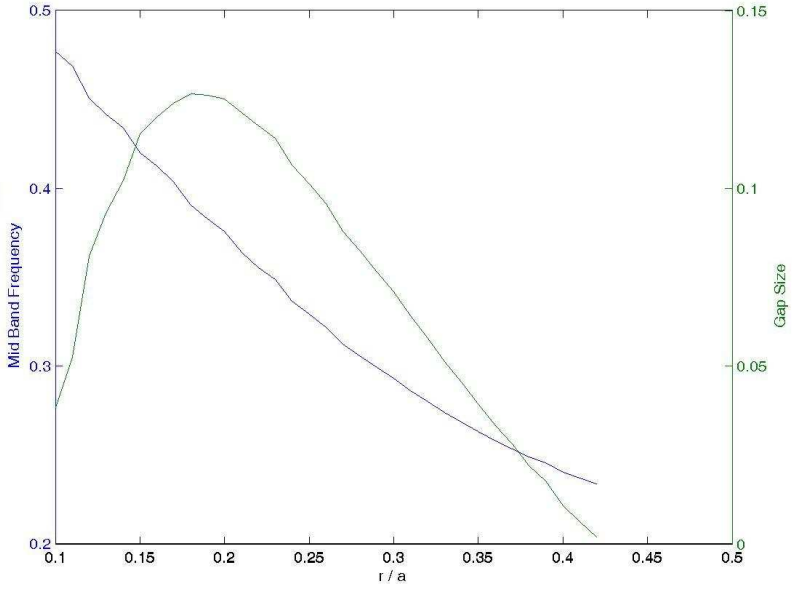

Fig. 4.2 Estimation of the Rod Radius. For SQ rods

The second important parameter that we have to consider now is the volume ratio of the crystals in the unit cell which is another way of saying *r/a*. Fig. 4.2 is plotted to point out the gap size dependency to the rod radius. It is obvious that gap sizes would shrink as we increase *r/a* values after a certain point. The propagating wave would see almost a homogenous block rather than a crystal structure. Too thin crystals would also not be able to scatter the light, so splitting only small gaps. It can be deducted from the figure that *r/a* values in the range of 0.15 to 0.25 might be practical. However frequencies around the value of 0.15 are comparatively large and we may not be able to sweep the whole frequency spectrum in the gap at the experimental stage. In fact, $r = 0.2a$ both addresses lower frequencies and huge band gaps as we desire. This methodology is analogous to the small signal amplifier designs in analog circuits where we begin by searching for a biasing point that produces swings without distortions.

Then two important factors have been settled down. In the continuing parts, our crystals will be alumina rods with a radius of $0.2a$, in terms of the lattice constant.

4.2 Proposed Method for sensing very small refractive index changes

As an example, we calculated the lowest two bands for a square lattice of rods with a lattice constant *a* and a rod diameter of $d = 0.4a$. The dispersion diagram is plotted in Fig. 4.3 where the points Γ, X, M are the traditional representations for the corners of the irreducible Brillouin zone of the square lattice. Each rod stands in air and has a dielectric constant of $\varepsilon_{rods} = 13.39$. The slopes at the three designated band edges are small enough to practically study the phase shifts. When the background dielectric constant, which is air in our case, is perturbed, band diagrams move such that an EM wave traveling with a certain frequency and a wavevector, is going to require a phase shift. If the transmission at that particular frequency is investigated, the amount of phase shift, $\Delta\Phi$ is directly proportional to Δk. The phase shifts at the first band edge can graphically be seen in Fig. 4.4. For the same PC configuration whose band diagram is displayed in Fig. 4.3, Fig. 4.4 illustrates the band modulations at the first edge. The dispersion relations have been solved in the Γ-X direction as the

background index is incremented (dashed line) from its initial value (solid line). At a specific frequency, f_0, the EM wave will have a phase shift that can be defined as, $\Delta\Phi = \Delta k.L$ where L represents the optical path traveled by the EM wave.

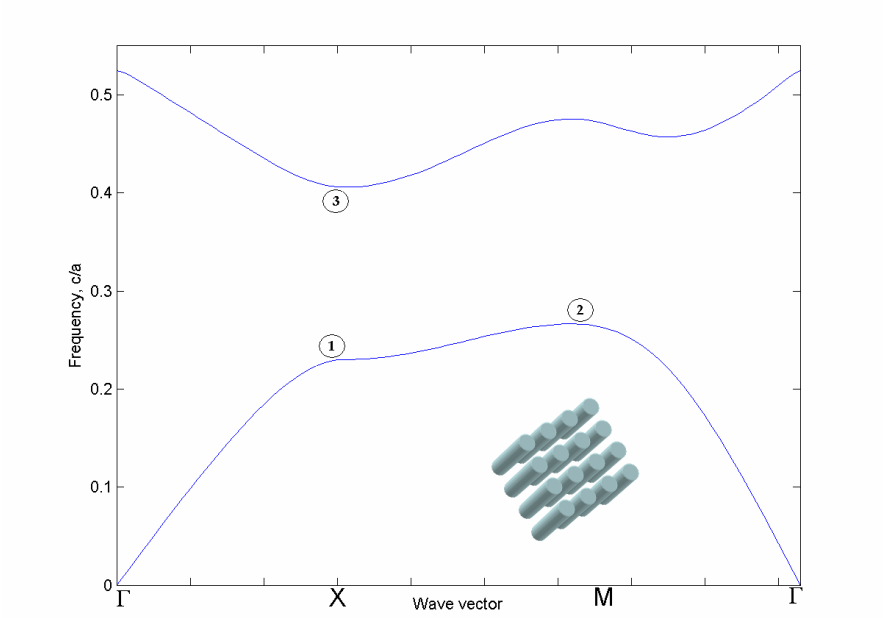

Fig. 4.3 Band edges

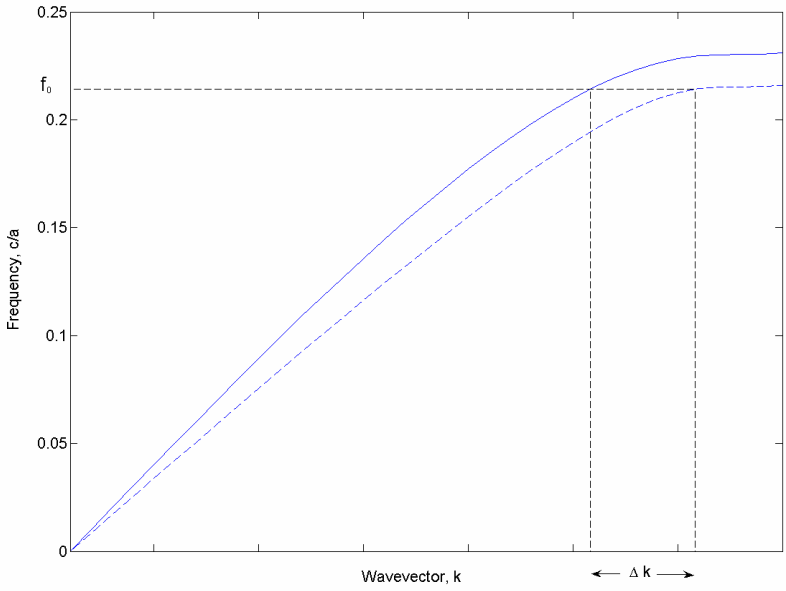

Fig. 4.4 Phase shift estimation from *w-k* graph at band edge 1

Following the same methodology, we have estimated the relevant phase shifts at our three band edges separately. The evaluations have been computed for index modulations starting with 10^{-5} down to 10^{-10}. The graph in Fig. 4.5 reveals that the phase shifts pursue almost a linear response on the logarithmic scale with respect to the index modulations. It should be noticed that the reported phase shift values are given per unit lattices. Consequently, we deduce that we should theoretically detect index variations on the order of $10^{-13}/\sqrt{Hz}$ with a 100x100 PC configuration of square lattice of dielectric rods using a very sensitive interferometer structure [58].

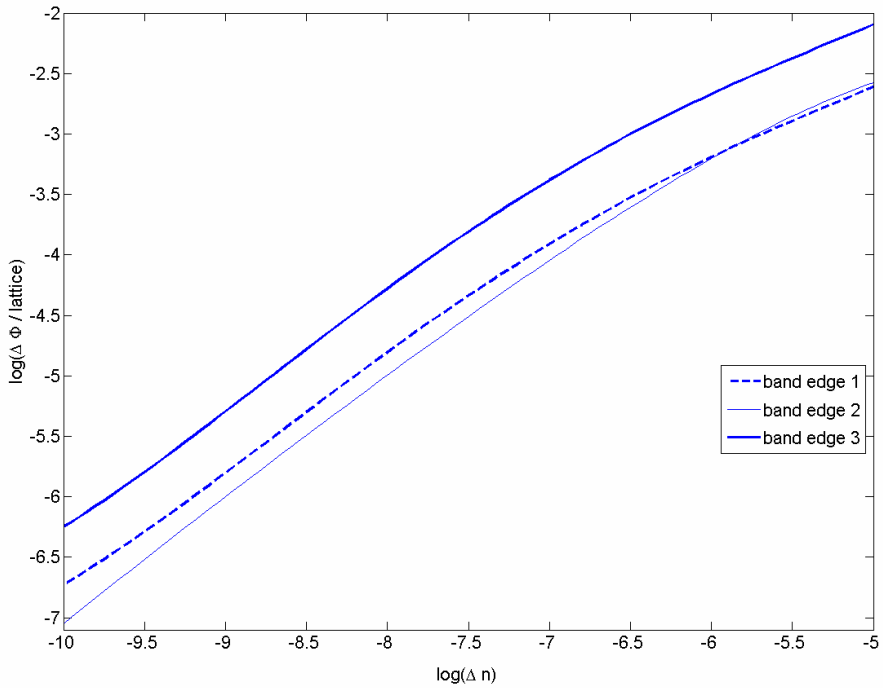

Fig. 4.5 Phase change per lattice for the band edges shown in Fig. 4.3 is plotted as a function of the index change.

Δn	Band Edge 1	Band Edge 2	Band Edge 3
10^{-5}	2.4×10^{-3}	2.7×10^{-3}	8×10^{-3}
10^{-7}	1.2×10^{-4}	9.3×10^{-5}	4.1×10^{-4}
10^{-10}	1.8×10^{-7}	8.8×10^{-8}	5.6×10^{-7}

Table 4.1 Phase change per lattice for the band edges shown in Fig. 4.3 is listed as a function of the index change

Moreover, when we compare the performance characteristics at distinct band edges, it is apparent that better results can be attained by working at edge 3. Upper band is influenced at higher rates from index modulations, which causes larger phase shifts as an output. Likewise, similar arguments can be done for PC with defects. Modest defect bands, created by the removal of one dielectric rod would also produce phase shifts. Actually, we anticipate that defect based PCs are promising candidates for sensor applications. PC defects set up cavities whose bands can easily be modulated by refractive index perturbations. We propose that sensitivities can be further improved down to $10^{-14} / \sqrt{Hz}$ with simple defect formations.

4.3 Cavity based designs

The proposed cavity structure can be further used on for two specific goals. First, it can be operated to sense the material based faults, in other words to sense the refractive index alterations in materials. Secondly it can be utilized to serve as a gas sensor, which can sense the index changes at the background material, which is air in our case.

4.3.1 Sensing Material Faults

The tuning ranges of these types of cavities had been laid down in Fig. 2.23 and 2.24. When Fig. 2.24 is examined carefully, it is apparent that the only useful parts are in between r_{defect}= [0, 0.15a] and r_{defect}= [0.25a, 0.4a]. Modulation effects after r_{defect} = 0.4a has not been drawn, but similar behavior of the defect site continues there as well. Hence, all the states lose their uniqueness once they sweep the band and develop into at least doubly degenerate states. But we would like to work with single mode, non-degenerate elements. The dipole modes contain two states with the same wave vector. This may bring trouble for our measurement techniques. So our range is further narrowed down to r_{defect}= [0, 0.15a].

Our objective in this sensing mechanism is to build a system that can perceive the small refractive index changes of the rod at the defect site. In other words we are

perturbing the confined electric fields. Then we would like our perturbation to be as efficient as possible. Coupled mode theory tells us that it can be maintained by maximizing the overlap integral of the perturbation function with the electric fields.

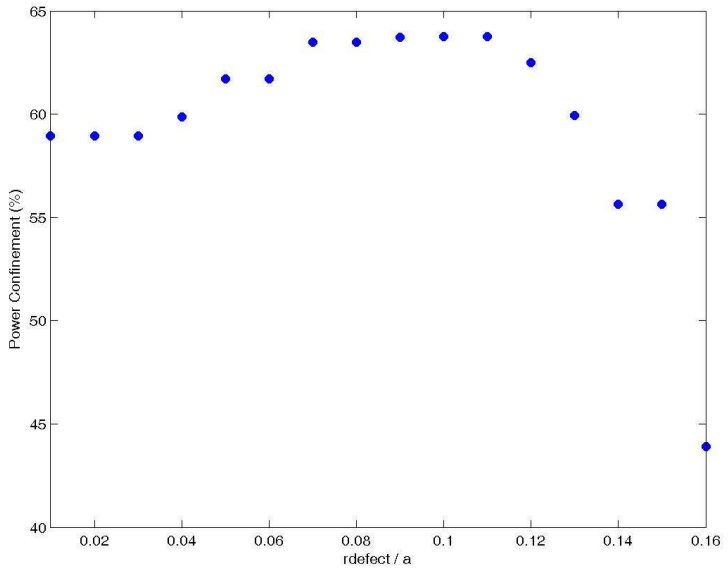

(a)

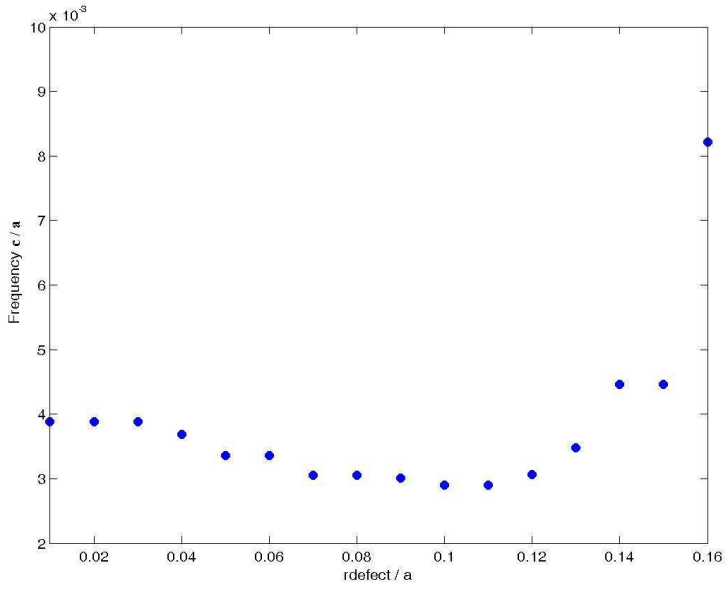

(b)

Fig. 4.6 Estimation of defect size (a) Power Confinement at the defect site (b) Defect band bandwidth. Notice that all frequency values are still normalized.

In the given range, the defect size variations would modify both the power confinement and the bandwidth of the defect band. These are the parameters directly responsible for the quality assessment of the defect site. We would favor power confinement over anything, because our perturbations would be sensed by the system in a more delicate way. A defect radius of $0.1a$ seems to be meeting our expectations. Then our cavity is totally formed.

If the material's refractive index at the defect site is electroptically tuned to imitate the refractive index modulation, then the transmission spectrum of the defect would shift accordingly. In the light of Fig. 4.7, the frequency shifts of the midband frequency of the defect band almost follow a linear path with a finite slope of approximately 0.03.

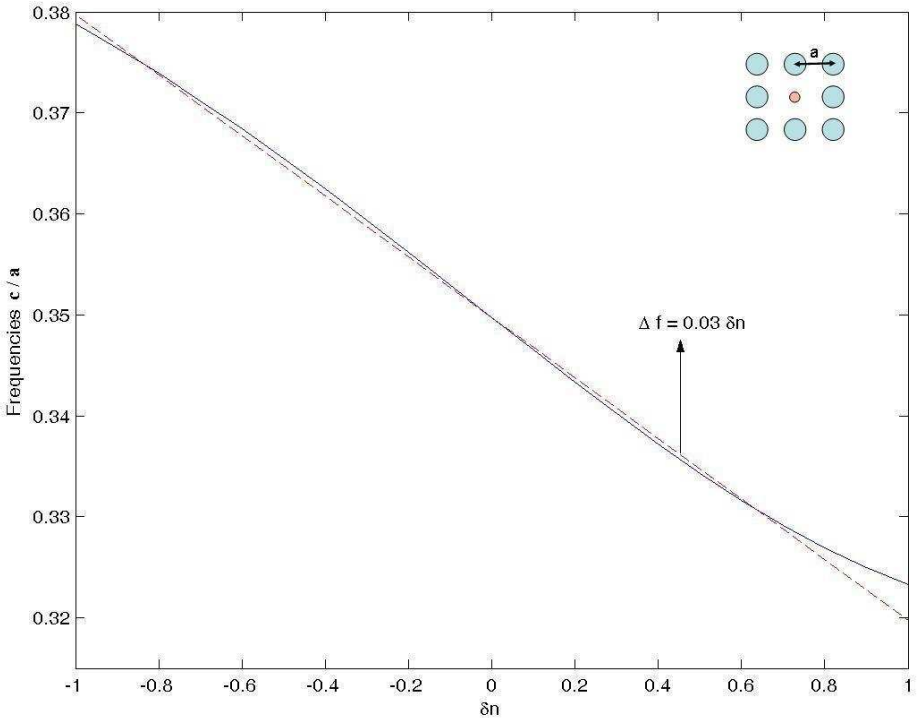

Fig. 4.7 Frequency Shift vs index modulation

Chemical sensing with Photonic Crystal based cavities has attracted considerable attention recently. Loncar et al. [13] had proposed a laser cavity whose spectrum can be shifted by an amount of $\Delta\lambda \approx 266\Delta n$ (as a fitting parameter) for a

Photonic Crystal structure with lattice constant on the order of 400 nm. Then when we reconfigure Fig. 4.7 for wavelength swings, we can obtain Fig. 4.8. For the same lattice constant, this cavity structure yields $\Delta\lambda \approx 115\Delta n$.

Nevertheless, our major concern has never been the long wavelength shifts due to large index modulations. We are rather trying to sense very low index modulations which Loncar et. al. have not particularly studied. For such modulations the plane waves inside the crystal will still be in phase. The phase shift brought by the crystal can be calculated.

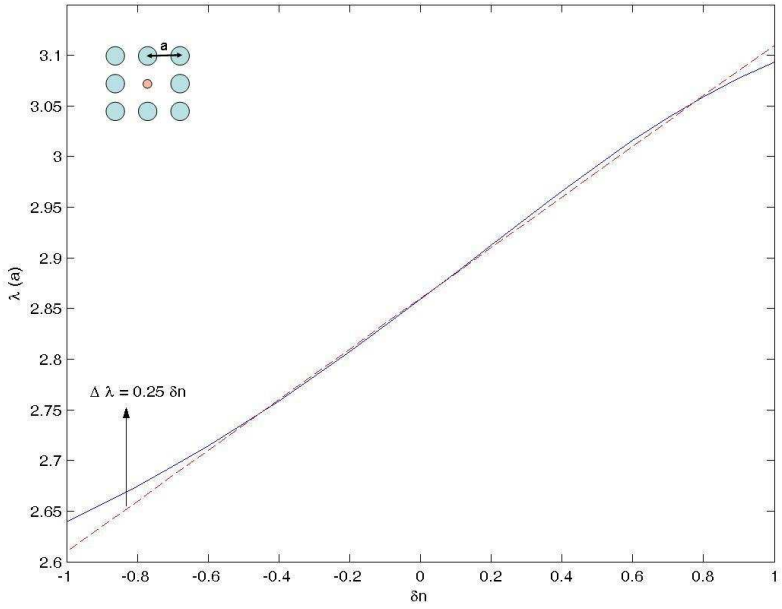

Fig. 4.8 Wavelength Shift vs index modulation

Fitting functions reveal that the linearity of the modulation is preserved even at comparatively low modulations. We suggest that using simple cavity structures like we have already defined, super sensitive refractive index sensing can be feasible. Fig. 4.9 implies that theoretically speaking, 1 GHz frequency shift would be the result of only 10^{-6} in the optical regime. PWE might have convergence problems, but these problems are valid for every single calculation. The error offset is almost constant and our computation tolerance value can be lifted up to $10^{-8}\,c/a$ without any significant problems. Then the swinging *w-k* band diagrams at the resonance frequency could be

drawn. The defect band is modulated by $\Delta n = 10^{-3}, 5\times10^{-4}, 10^{-4}$ respectively in Fig. 4.10. There are two suitable saddle points to study the phase shifts, one at point K and the other at point M. The slopes are too low and makes it practical to study the $\Delta k_{w=const.}$.

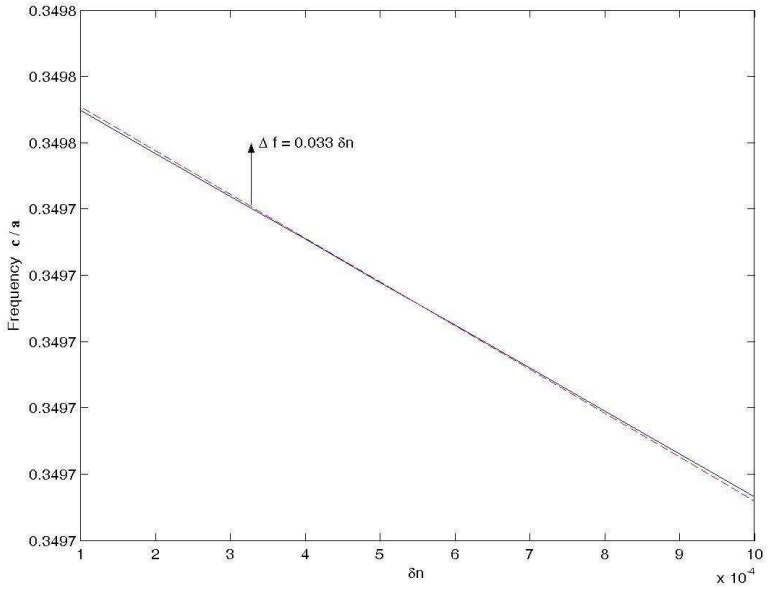

Fig. 4.9 Frequency Shifts at low Index Modulation

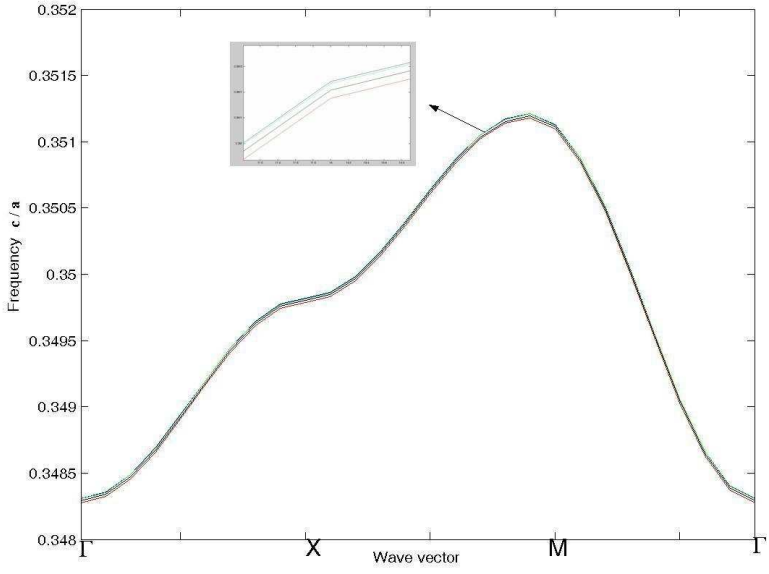

Fig. 4.10 Defect Band Hopping with Index Modulations

The relative phase shifts at band M are listed in Table 4.2.

Phase Shifts (mRad / a)	
$\Delta n = 10^{-4}$	133.5 – 138.7
$\Delta n = 10^{-5}$	31.8 – 51.1

Table 4.2 Phase Shifts vs Index Modulations

When we compare the results listed in Table 4.2 with the phase shift values with bulk PCs without any defect site, there evidently exist an enhancement on the order of 10. Accordingly, if we again assume a linear behavior in the logarithmic scale, similar to the case depicted in Fig. 4.5, we can deduct that it is possible to sense refractive index variations down to 10^{-11} per lattice distance at band edge M. Roughly speaking, the performance characteristics are improved 10 times with the inclusion of a defect site.

The values in Table 4.2 are given inside certain intervals unlike the bulk crystal, because of the difficulties in determining the exact phase shifts with MIT Band package program.

4.3.2 Gas Sensor

A gas sensor could also be realized with a similar configuration. Gas sensor that can sense the perturbations in the environment would be more than functional. In this part, we will examine the performance issues of such a design.

The same cavity design could be applied to this version of the problem. However now, the background index modulation is taking place. Assuming that the index of the air is almost homogenously perturbed in a unit volume, the cavity could be utilized to work in an analogous fashion.

The background index modulations should be a major element in determining the resonance frequency of the defect. Then again the electric fields should be localized where the perturbation takes place. In other words, the defect must be created by totally removing the rod. Next we can start by inspecting the defect

resonance frequency shifts in the same manner like we have just done for our first design. But in this case, the background material is in the gas form, and would only yield perturbations on the order of $10^{-4} - 10^{-5}$ at most. Actually, the index of air that we breathe may fluctuate around those values as a function of harsh pressure and temperature conditions.

It appears that such a design is much more sensitive to index modulations. This is logical under the context that we are modifying the whole crystal structure rather than just being contended with the defect site. Comparing it again, this corresponds to a value of $\Delta\lambda \approx 660\Delta n$ for a lattice constant of 400nm.

Phase Shifts (mRad / a)	
$\Delta n = 10^{-4}$	164.3 – 166.9
$\Delta n = 10^{-5}$	48.5 – 58.1
$\Delta n = 10^{-6}$	9.7 - 34.4

Table 4.3 Phase Shifts vs Index Modulations for the second design

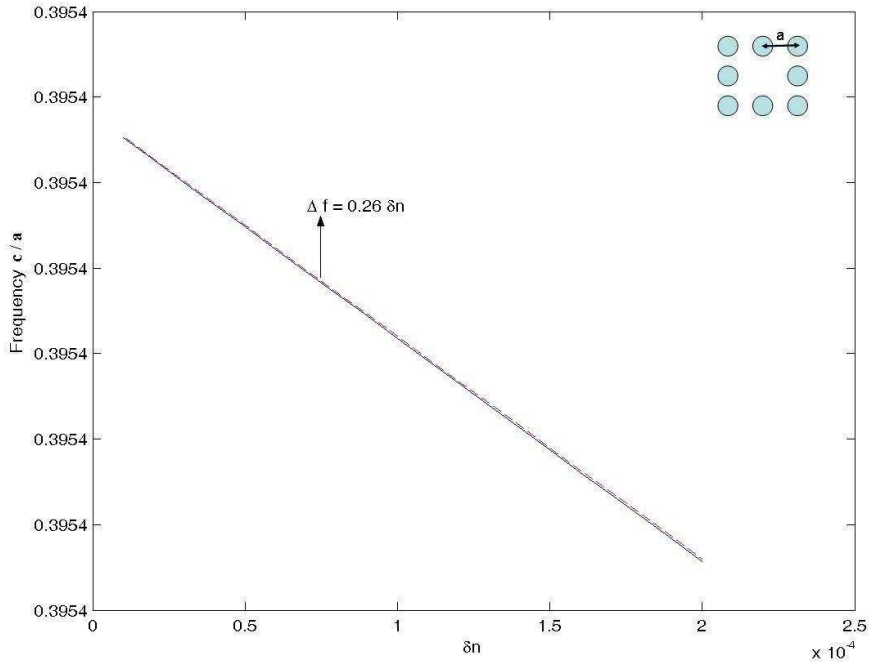

Fig. 4.11 Frequency Shift vs index modulation for the second design

Table 4.3 dictates that sensing 10^{-12} per lattice is feasible with the proposed gas sensor, again by extrapolating the values for smaller changes. MIT is not very helpful for such calculations. The exact results should be obtained directly by other PWE methods. Still an improvement on the order of 100 with respect to the bulk crystals can be attained.

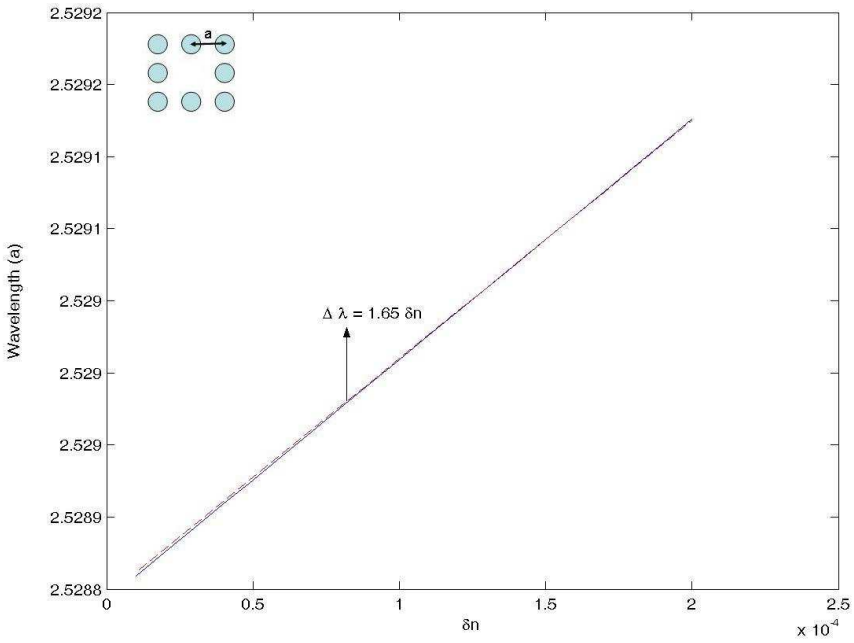

Fig. 4.12 Wavelength Shift vs index modulation for the second design

4.4 Final Words

We have tried to deliver the basic design frame that we have been through. The results show that even with these modest and trivial cavity structures together with the band edge modulation techniques of the bulk crystals, high resolution, and sensitive sensing mechanisms are feasible. People have come up with many other topologies. Most of them require a lot more significant control and FDTD tools are like an obligation.

Yet, with only employing PWE methods, nice designs are still achievable with some error tolerances. However, we also have made some significant assumptions in our designs. In real life it would be hard to fabricate alumina rods with perfectly 3.13

refractive indices and with exact dimensions. We also neglected the material dispersion effects. The dielectric constants would also be shifted while sweeping a frequency interval. One last supposition has been the consideration of the gas surrounding the sensor to be homogenous. A closed and isolated environment could only sustain such conditions.

Consequently, one must be precautious while applying the theoretical designs into the real world. The tolerable error margins have to be decided upon and the viability of the experiments should be discussed ahead.

In the following chapter we will be presenting the attainment of the experimental set-up at the microwave regime. Similar design configurations will be of our concern.

CHAPTER 5

PHOTONIC CRYSTALS AT THE MICROWAVE REGIME

Owing to the generality of our *master equation* (eq. 2.4), we have so far limited ourselves to no specific frequency regime or in other words to any dimensions. We have paid attention to write all the frequency components in terms of the lattice constants. So, all the frequency values are easily scalable to any frequency regime.

Inspired by the works of Ref. 58, we have been determined to experimentally demonstrate the basic notions that we have laid out theoretically in the previous chapters.

Building a Photonic Crystal block that closely satisfies our design parameters in chapter 4 has been our major objective. Now, we are going to begin by presenting our experimental set-up. First, the Photonic Crystal structure will be clarified, and then other microwave components will be described. Our fundamental theoretical expectations will be compared with the experimental outputs at the final stage.

5.1 Photonic Crystal

We have conducted our experiments in the microwave regime with a PC made up of a 7x7 (49) matrix of alumina rods. The simulations had been carried out for 2-D

structures and therefore the length of the constructed PC has been chosen to be long enough to sustain homogeneity in the third dimension. The main operating frequency has been selected as 10GHz, which corresponds to a wavelength of λ=3cm. At this stage, we predicted that a length of 5λ would be sufficient to minimize the scattering in the third dimension. A square lattice configuration has been achieved by arranging 15cm long alumina rods properly with a lattice constant of 1cm. Alumina is a reliable material with low tangent losses and a relatively high dielectric constant of 9.79.

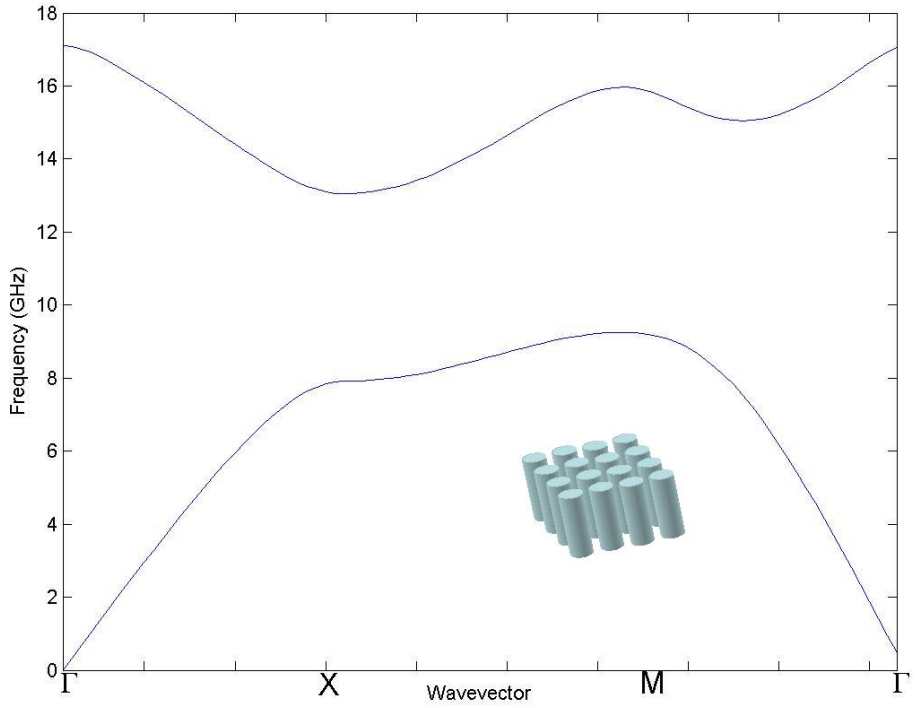

Fig. 5.1 Band diagram of our Photonic Crystal

The radius of the rods were assigned to be 0.2cm to split up a band gap approximately between 7.91-13.04 GHz in the Γ-X direction and 9.25-15.96 GHz in the X-M direction. The band diagram of our Photonic Crystal configuration has been portrayed in Fig. 5.1. Rod, by rod we carefully constructed our crystal structure by gluing to Plexiglas holders. The holders were placed to make sure that alumina rods were standing totally aligned and straight. Actually, we had planned to carry out the experiments with a greater matrix of 11x11, but the limitations in the market obliged

us to work with a 7x7 matrix. Still we were well aware of the difficulties that smaller matrices would bring [59]. Smaller dimensions would mean, bigger deviations from the theoretical results, which were performed assuming infinitely extending PCs in the x-y plane.

5.2 Experimental Set-Up

Our experimental set-up is composed of two antennas for transmitting and receiving purposes. Both of the horn antennas have been designed with the following parameters as shown in Fig. 5.2. The designed antenna's operating frequency has been chosen to be closer to the mid-bandgap.

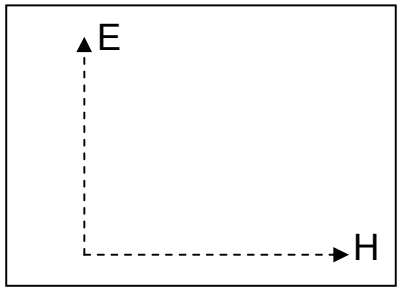

E=9mm
H=22mm

Fig. 5.2 Horn Antenna Dimensions for f = 10 Ghz

The antennas exhibited a flat transmission (flat S_{21}) and high radiation (low S_{11}) around the two lowest frequency bands of the PC, which have been vital for our experiments. Fig. 5.3 and Fig. 5.4 demonstrate S-parameters of the antennas with respect to the frequency. The S_{11} stays below -10dB which is a widely accepted threshold for a well designed antenna. Moreover, S_{21}, that determines the transmission characteristics were relatively flat around our operating frequencies that ensured minimal non-idealities contributed by our antennas. The antennas have been strictly aligned to face each other on the same horizontal line. The aperture and the beam size of the antennas were comparably smaller than the dimensions of our PC to allow most of the field to be coupled into the PC and thereby preventing the unwanted fields to be detected by the receiver horn due to the finite size of our PC.

Antennas were manufactured from brass and copper. Representative layouts were drawn for the antennas. The exact dimensions are given in Fig. 5.5.

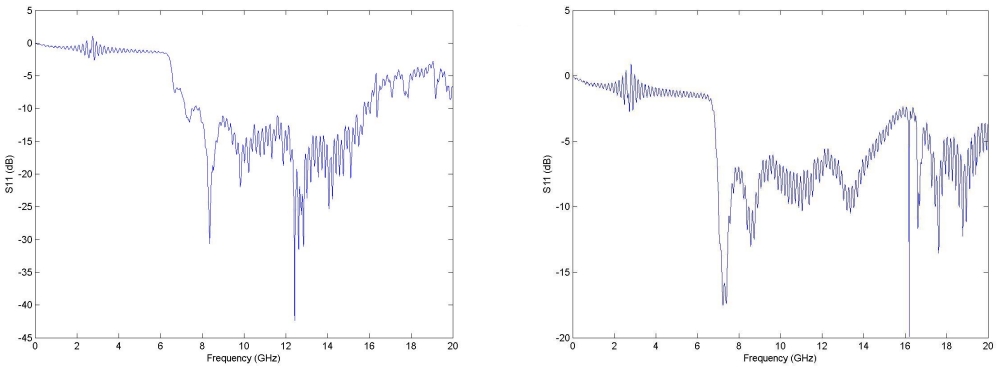

Fig. 5.3 S_{11} characteristics for (a) antenna1 and (b) antenna2

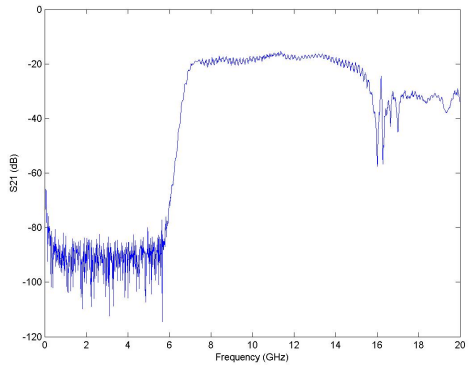

Fig. 5.4 S_{21}characteristics when distance between antennas, d = 25 cm

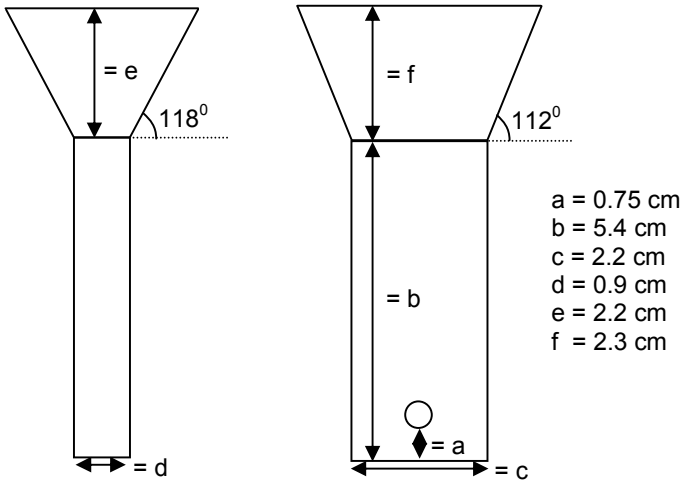

Fig. 5.5 Layout representation of the antennas

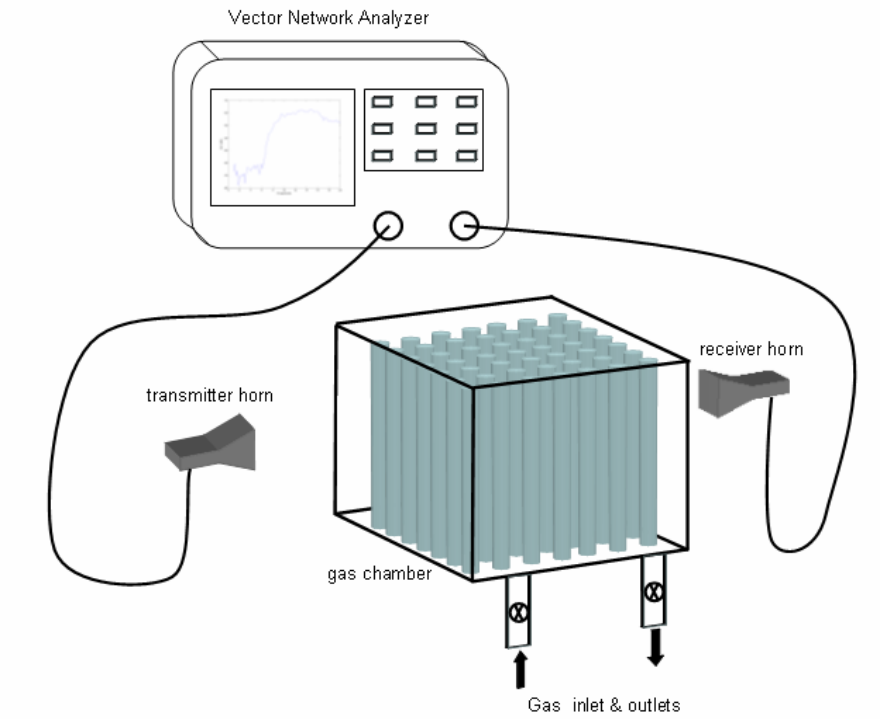

Fig. 5.6 Experimental Set-up

After having investigated antenna characteristics, Fig. 5.6 shows the experimental setup built in our microwave laboratories. The index modulation and thereby the sensing mechanism is based on the pressure dependence of the refractive index of the nitrogen gas. A Plexiglas gas chamber sustained isolation for the PC that is located inside. The inner pressure is adjusted with the help of a nitrogen tank. All the air is assured to be taken out to the chamber via the gas outlet while nitrogen is steadily pumped from the gas inlet. A pressure sensor, MPX2202DP had been attached to the gas chamber to keep track of the dielectric constant of the nitrogen gas. In order to realize our aim, an expression was already available. At higher radio frequencies, the refractive index of nitrogen gas is assumed to vary almost linearly with changing pressure (P) according to the following equation [60,61]

$$(n_{nitrogen} - 1) \times 10^6 = 294.1 \times P \tag{5.1}$$

Our chamber could stand up to 1.5 atm that would alter the refractive index of nitrogen by 10^{-4} at most. This value would be our top boundary for highest index modulations to achieve phase shifts on the traveling EM wave. For that prospect, S-parameter Vector Network Analyzer, Agilent 8720ES has been used to generate the EM waves propagating through the PC located inside the gas chamber. Data analysis of the received signals has also been carried out with the Network Analyzer

5.3 Experimental Results

First, in order to annul the Fabry Perot resonations from the consecutive walls of the Plexiglas gas chamber, the transmission characteristics of our PC has been studied in air. The free space transmission of the antennas (Fig. 5.4) had been saved initially, and then the transmission values through the PC structure have been processed. Fig. 5.7 illustrates the ratio of these gathered quantities.

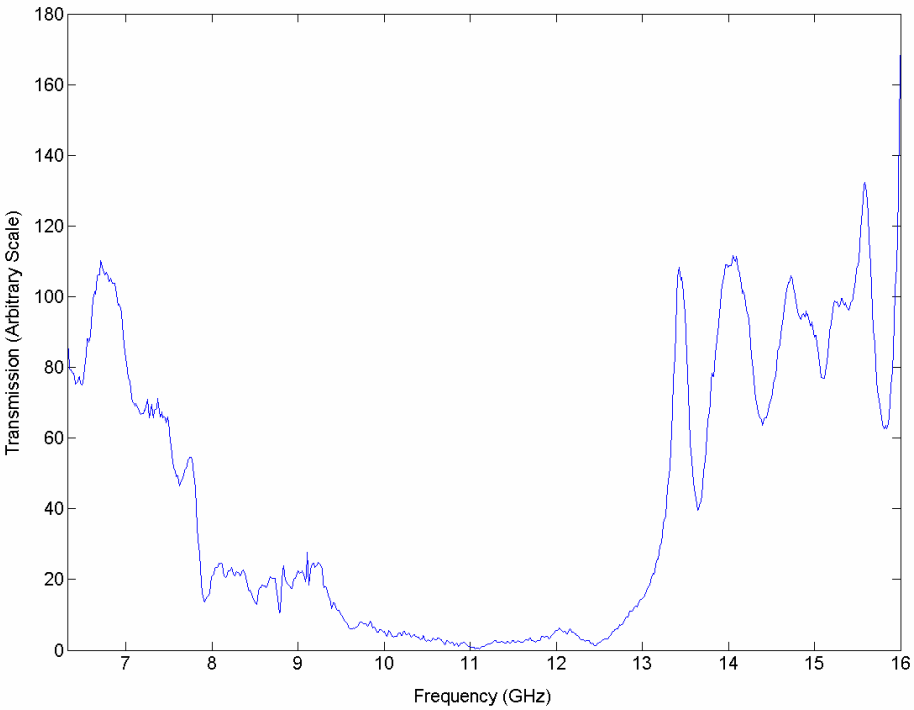

Fig. 5.7 Transmission characteristics in air. Notice that the transmission values on the y-axis are arbitrary units.

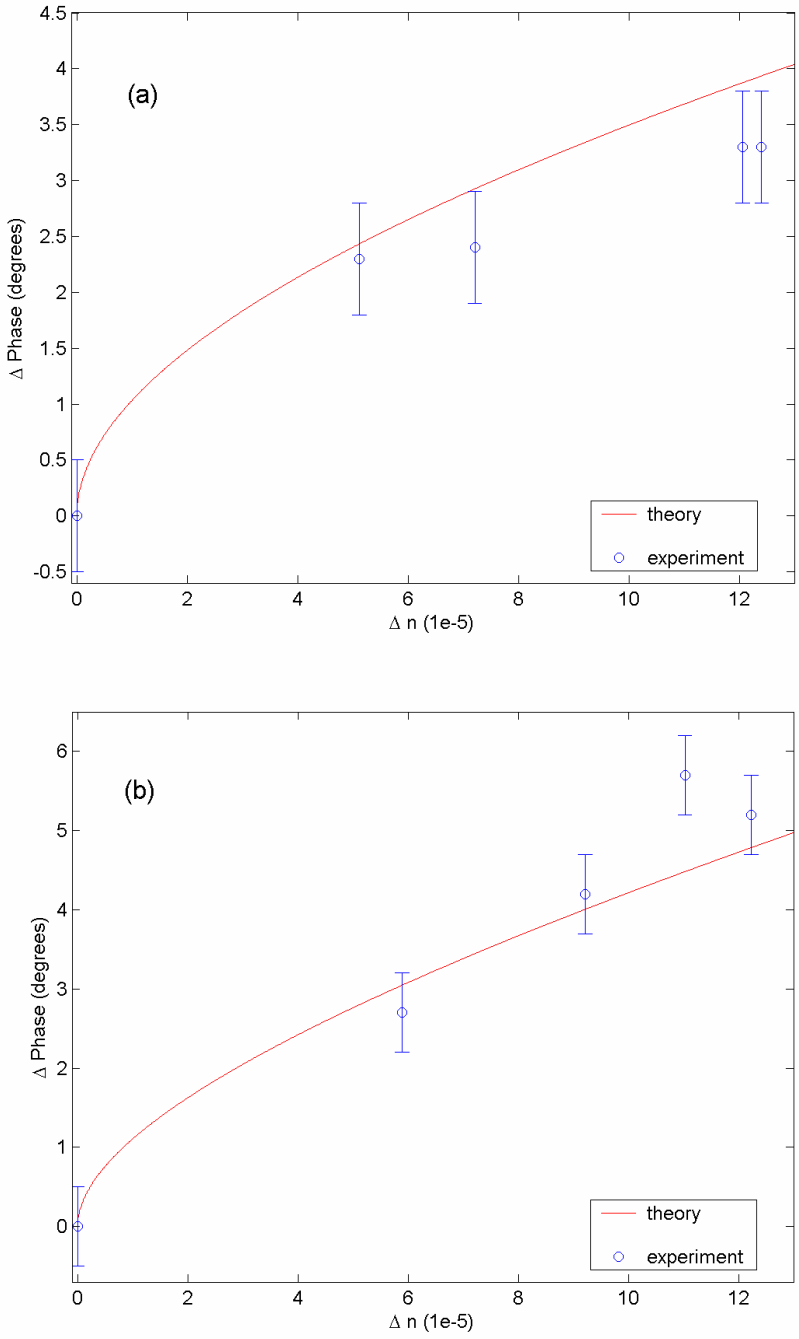

Fig. 5.8 Theoretically calculated and experimentally measured phase shift values at the band edges (a) Phase shifts at X band edge, f=8GHz (b) Phase shifts at M band edge, f=9.3GHz

As the network analyzer sweeps the frequency ranges, we would expect to see discontinuities in S_{21} parameters due to the photonic forbidden region. The transmission characteristics reveal the band edges of our configuration. In agreement with the theoretical expectations, the band edges turned out to lie roughly at 8GHz and 13GHz. Yet, there is still considerable amount of transmission up to 9.3GHz owing to the unstoppable coupling of the wave vectors in the X-M direction.

Nonetheless, we have determined our band edges. Later on, we would work specifically at these points. Experiments that are carried out at 8 and 9.3GHz show that our theoretical expectations are in very good agreement with the measured phase shifts as depicted in Fig. 5.8. While the inner pressure is modulated in between 1atm and 1.5atm, the phase shifts of the EM wave have been registered as an output of the network analyzer. The network analyzer's embedded inner circuits combine both of the transmitted and received signals with some kind of a mixer topology to calculate the relative phase differences. This is supposedly the electrical analogy of the optical interferometer configuration that has already been discussed.

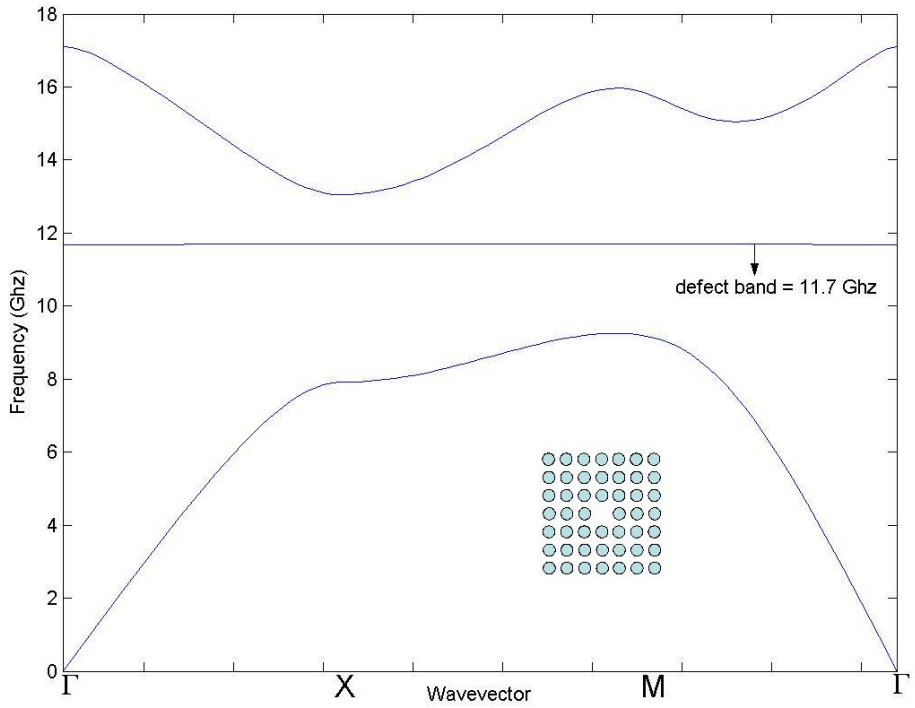

Fig. 5.9 Defect band diagram

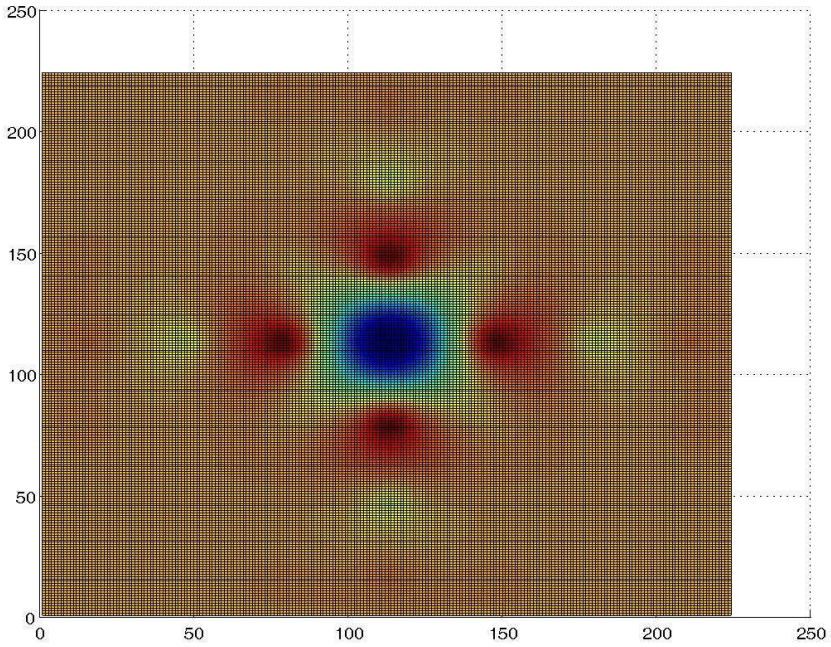

Fig. 5.10 Confined mode profile at the defect site

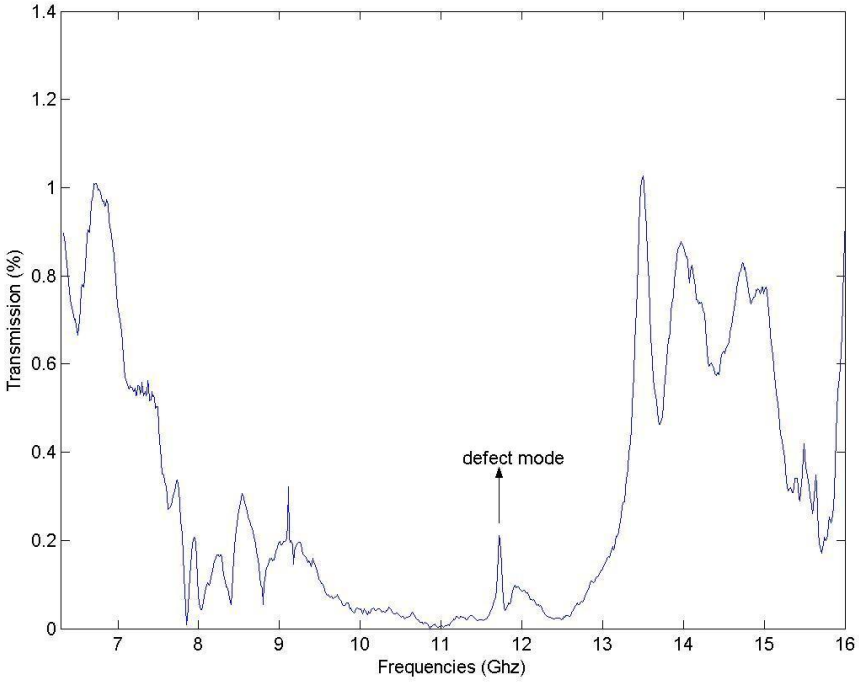

Fig. 5.11 Transmission characteristics of the defect configuration in air. Notice that the transmission values on the y-axis are arbitrary units.

We have also investigated the defect configuration by removing a single rod from the middle of the matrix. According to the theoretical results, the defect band would reside at 11.7GHz. The band structure has been exhibited in Fig. 5.9. Experimentally, we have examined the case by inspecting the transmission characteristics of the PC again in air. Experimental results support that there is a confined mode inside the cavity, whose mode profile is given in Fig. 5.10. The transmitted power out of the cavity has been detected by the network analyzer and is plotted in Fig. 5.11. There used to be no resonances in the band gap, but a sharp peak can now be noticed when the rod is removed from the middle of the matrix. However, we have not been able to follow the same procedure by particularly determining the phase shifts at defect bands. It has been left as a future study.

5.4 Discussion of the Experiment

We have also calculated possible phase differentiations if PC were not present in the chamber to convince ourselves that the primary changes were caused by the band edge modulations. As we modify the gas pressure, an L = 12cm long chamber would also yield a phase difference in proportional to the expression given in Eq. (5.2).

$$\Delta\Phi = \frac{2\pi}{\lambda}\Delta n_{nitrogen} L \tag{5.2}$$

However, even if a rather huge modulation were applied on the order of $\Delta n_{nitrogen} = 10^{-4}$, a phase change of only 0.14 degrees would be achieved, which obliges our resolution to be around 25 times worse than the scenario with PC. Without any doubt, modulation at the photonic band edges is dominantly responsible for phase shifts. Besides, a waveguide structure with the same length, experiencing the same amount of index modulations in its claddings would at most cause a phase shift of 0.1 degrees, which again signifies the importance of our configuration.

In our experiment, most of the errors are coming from the nonidealities of the antennas and PC structure. Better results are predicted with improved antenna designs. Moreover, as the number of layers in PCs has increased, deviations from

theoretical results are expected to decrease dramatically. The finite size of the PC is the major problem. Hence, larger superlattices could bring our simulation results closer to the experiment output values.

Nevertheless, we have accomplished several significant points. Theoretical calculations have been successfully carried out in the simulation environments, and the experimental results back up the theoretical expectations. The theoretically determined phase shift values can be directly correlated with our experimental results as shown in Fig. 5.8 at two separate band edges. We have completed our proof of principle experiments fruitfully. The method looks very promising and we have not come across with a particular problem that would prevent us from sensing even much smaller index modulations in a perfectly isolated space with higher resolution interferometer topologies for future attempts.

CHAPTER 6

CONCLUSIONS AND FUTURE WORK

We have proposed that the location of the band edges and the location of the defect bands of a photonic crystal structure is a strong function of the dielectric contrast; hence a propagating EM wave will acquire a phase shift if there is a change in the dielectric constants of the structure.

We have performed the proof of principle experiments in the microwave regime with a photonic crystal made of 7X7 alumina rods placed in a gas chamber. The refractive index changes were obtained by changing the gas pressure and the resultant phase shifts were recorded with a vector network analyzer. The experimental results were in good agreement with the theoretical calculations.

In our experiments we employed rather large index changes since the vector network analyzer is rather a crude instrument to determine very small phase shifts. However if the phase shifts can be recorded interferometrically, calculations show that we can sense index changes on the order of $10^{-13}/\sqrt{Hz}$ down to signal bandwidth of 1Hz by using a 100 lattices. Also, a further sensitivity increase of a factor of 10 is possible by recording the phase shift of a defect mode signal.

The theoretical investigations show that defect bands are even better candidates specifically for sensor applications. The realization of the experimental setup with the

defect band and the demonstration of the predicted theoretical phase shifts are major future works at the experimental side. Also, the volume of the gas chamber could be shrunk down. Further experiments can be carried out at higher frequency regimes such that the control and isolation over the gas pressure in the chamber could be handled much more efficiently with smaller dimensions. Then, the limits of our sensor could be tried with the construction of interferometers with very high sensitivities. The established multi functional sensor design could be used as a chemical detector in liquids where ultra precision is vital. It could be utilized as a pressure sensor and could find many other application fields in biomedical practices.

REFERENCES

[1] Robert W. Coutant and G. William Keigley, Analytical Chemistry **60**, 2538 (1988).

[2] Otto S. Wolfbeis, Analytical Chemistry **72**, 81R (2000).

[3] Sheng Hong Yu, Cheng Hau Chen, and Huihua Kenny Chiang, APBP 2004, IEEE, 165, (2004).

[4] J. B. Jensen, L. H. Pedersen, A. Carlsen, P. E. Hoiby, L. B. Nielsen, A. Bjarklev, and T. P. Hansen, OSA 2002, OSA, CTuP5, (2002).

[5] G. J. Veldhuis, L. E. W. van der Veen, and P. V. Lambeck, J. Lightwave Technol. **17**, 857 (1999).

[6] Romeo Bernini, Stefania Campopiano, Charles de Boer, Pasqualina M. Sarro, and Luigi Zeni, IEEE Sensors Journal **3**, 652 (2003).

[7] H. P. Ho, W. W. Lam, P. L. Wong, and F. Guo, Electron Devices Meeting, IEEE, 55, (2002).

[8] R. D. Harris, B. J. Luff, J. S. Wilkinson, R. Wilson, D. J. Schiffrin, J. Piehler, A. Brecht, R. A. Abuknesha, and C. Mouvet, Institution of Electrical Engineers, IEE, 1, (1995). Savoy Place, London, (1995).

[9] Eli Yablonovitch, Phys. Rev. Lett. **58**, 2059 (1987).

[10] Stanislav O. Konorov, Aleksei M. Zheltikov, and Michael Scalora, Opt. Express **13**, 3454 (2005).

[11] X. Wang, K. Kempa, Z. F. Ren, and B. Kimball, Appl. Phys. Lett. **84**, 1817 (2004).

[12] Jesper B. Jensen, Lars H. Pedersen, Poul E. Hoiby, Lars B. Nielsen, T. P. Hansen, J. R. Folkenberg, J. Riishede, Danny Noordegraaf, Kristian Nielsen, A. Carlsen, and A. Bjarklev, Opt. Lett. **29**, 1974 (2004).

[13] Marko Loncar, Axel Scherer, and Yueming Qiu, Appl. Phys. Lett. **82**, 4648 (2003).

[14] Alain Hache and Martin Bourgeois, Appl. Phys. Lett. **77**, 4089 (2000).

[15] Xiaoyong Hu, Yuanhao Liu, Jie Tian, Bingying Cheng, and Daozhong Zhang, Appl. Phys. Lett. **86**, 121102 (2005).

[16] Mehmet Bayindir, B. Temelkuran, and E. Ozbay, Appl. Phys. Lett. **77**, 3902 (2000).

[17] Mehmet Bayindir and Ekmel Ozbay, Opt. Express **10**, 1279 (2002).

[18] Solomon Assefa, Peter T. Rakich, Peter Bienstman, Steven G. Johnson, and Gale S. Petrich, Appl. Phys. Lett. **85**, 6110 (2004).

[19] Gregory P. Nordin, Seunghyun Kim, Jingbo Cai, and Jianhua Jiang, Opt. Express **10**, 1334 (2002).

[20] Steven G. Johnson, Christina Manolatou, Shanhui Fan, Pierre R. Villeneuve, J. D. Joannopoulos, and H. A. Haus, Opt. Lett. **23**, 1855 (1998).

[21] J. C. Knight, J. Broeng, T. A. Birks, and P. St. J. Russell, Science **282**, 1476 (1998).

[22] E. Yablonovitch, T. J. Gmitter, R. D. Meade, A. M. Rappe, K. D. Brommer, and J. D. Joannopoulos, Phys. Rev. Lett. **67**, 3380 (1991).

[23] O. Painter, R. K. Lee, A. Scherer, A. Yariv, J. D. O'Brien, P. D. Dapkus, and I. Kim, Science **284**, 1819 (1999).

[24] Wonjoo Suh and Shanhui Fan, Opt. Lett. **28**, 1763 (2003).

[25] Mehmet Fatih Yanik and Shanhui Fan, Phys. Rev. Lett. **92**, 083901-1 (2004).

[26] Mehmet Fatih Yanik and Shanhui Fan, Phys. Rev. Lett. **93**, 173903-1 (2004).

[27] B. Temelkuran, Mehmet Bayindir, E. Ozbay, R. Biswas, M. M. Sigalas, G. Tuttle, and K. M. Ho, J. of Appl. Phys. **87**, 603 (2000).

[28] B. Temelkuran, E. Ozbay, J. P. Kavanaugh, G. Tuttle, and K. M. Ho, Appl. Phys. Lett. **72**, 2376 (1998).

[29] Costas M. Soukoulis, *Photonic Band Gap Materials* (Kluwer Academic Publisher, AA Dordrecht, 1996)

[30] Steven G. Johnson and John D. Joannopoulos, *Photonic Crystals The Road from Theory to Practice* (Kluwer Academic Publisher, AH Dordrecht, 2002), Vol. **2**, p.25.

[31] K. Sakoda, *Optical Properties of Photonic Crystals* (Springer, Berlin, 2001)

[32] John D. Joannopoulos, *Photonic Crystals Molding the Flow of Light* (Princeton University Press, New Jersey, 1995)

[33] Charles Kittel, *Introduction to Solid State Physics*, **7**th edition (John Wiley, Canada, 1996)

[34] Richard L. Liboff, *Introductory Quantum Mechanics*, **3**rd edition (Addison Wesley Longman, 1997)

[35] Amnon Yariv, *Optical Electronics in Modern Communications*, **5**th edition (Oxford, New York, 1997)

[36] F. Villa, L. E. Regalado, F. Ramos-Mendieta, J. Gaspar-Armenta, and T. Lopez-Rios, Opt. Lett. **27**, 646 (2002).

[37] K. M. Ho, C. T. Chan, and C. M. Soukoulis, Phys. Rev. Lett. **65**, 3152 (1990).

[38] Robert D. Meade, Karl D. Brommer, Andrew M. Rappe, and J. D. Joannopoulos, Phys. Rev. B **44**, 13772 (1991).

[39] R. D. Meade, A. M. Rappe, K. D. Brommer, J. D. Joannopoulos, and O. L. Alerhand, Phys. Rev. B **48**, 8434 (1993).

[40] Kazuaki Sakoda, Noriko Kawai, Takunori Ito, Alongkarn Chutinan, Susumu Noda, Tsuneo Mitsuyu, and Kazuyuki Hirao, Phys. Rev. B **64**, 045116 (2001).

[41] Pierre R. Villeneuve and Michel Piche, Phys. Rev. B **46**, 4969 (1992).

[42] M. Plihal and A. A. Maradudin, Phys. Rev. B **44**, 8565 (1991).

[43] MIT Band Package Program (MPB), available at http://ab-initio.mit.edu/mpb/

[44] Solved with MPB

[45] Mehmet Fatih Yanik, Shanhui Fan, and Marin Soljacic, Appl. Phys. Lett. **83**, 2739 (2003).

[46] Mehmet Fatih Yanik and Shanhui Fan, Phys. Rev. A **71**, 013803-1 (2005).

[47] Susumu Noda, Alongkarn Chutinan, and Masahiro Imada, Nature **407**, 608 (2000).

[48] Mehmet Fatih Yanik, Wonjoo Suh, Zheng Wang, and Shanhui Fan, Phys. Rev. Lett. **93**, 233903-1 (2004).

[49] Toshihiko Baba, Ayumu Motegi, Takeshi Iwai, Naoyuki Fukaya, Yoshitaka Watanabe, and Atsushi Sakai, IEEE J. of Quantum Elect. **38**, 743 (2002).

[50] T. Ochiai and K. Sakoda, Phys. Rev. B **63**, 125107 (2001).

[51] T. Ochiai and K. Sakoda, Phys. Rev. B **64**, 045108 (2001).

[52] Steven G. Johnson, Shanhui Fan, Pierre R. Villeneuve, and J. D. Joannopoulos, Phys. Rev. B **60**, 5751 (1999).

[53] O. Painter, J. Vuckovic, and A. Scherer, J. Opt. Soc. Am. B **16**, 275 (1999).

[54] Tomoyuki Yoshie, Jelena Vuckovic, Alex Scherer, Hao Chen, and Dennis Deppe, Appl. Phys. Lett. **79**, 4289 (2001).

[55] E. Özbay, G. Tuttle, M. Sigalas, C. M. Soukoulis, and K. M. Ho, Phys. Rev. B **51**, 13961 (1995).

[56] H. S. Sözüer, J. W. Haus, and R. Inguva, Phys. Rev. B **45**, 13962 (1992).

[57] Linfang Shen and Sailing He, J. Opt. Soc. Am. A **19**, 1021 (2002).

[58] S. L. McCall, P. M. Platzman, R. Dalichaouch, David Smith, and S. Schultz, Phys. Rev. Lett. **67**, 2017 (1991).

[59] J. M. Hickmann, D. Solli, C. F. McCormick, R. Plambeck, and R. Y. Chiao, J. of Appl. Phys. **92**, 6918 (2002).

[60] L. Essen, Proc. Phys. Soc. B **66**, 189 (1953).

[61] K. D. Froome, Proc. Phys. Soc. B **68**, 833 (1955).